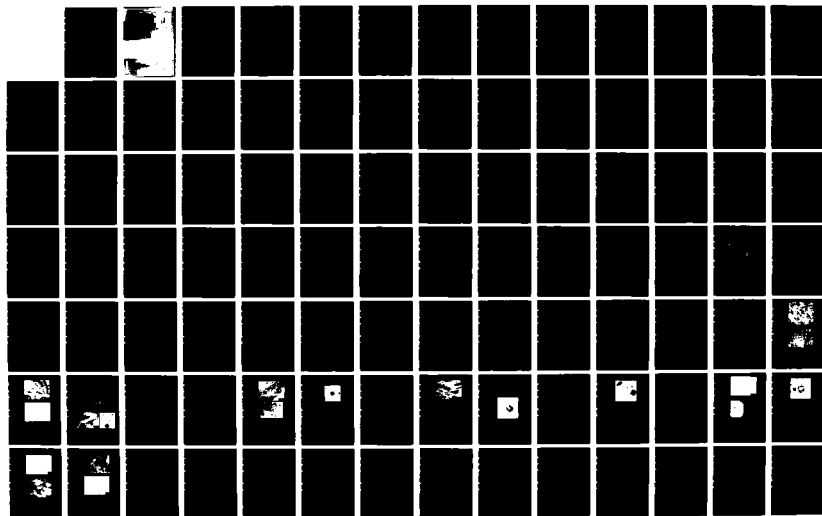AD-A148 610   EFFECT OF MICROSTRUCTURE AND TRAPPING ON THE HYDROGEN   1/2
                EMBRITTLEMENT SUSCE.. (U) CARNEGIE MELLON UNIV
                PITTSBURGH PA DEPT OF METALLURGICAL ENGI..
UNCLASSIFIED   M STEVENS ET AL. NOV 84 TR-19   F/G 11/6   NL
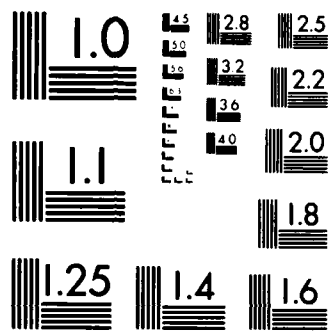
MICROCOPY RESOLUTION TEST CHART
NATIONAL BUREAU OF STANDARDS-1963-A

Technical Report No. 19

to

Office of Naval Research under
Contract N00014-75-C-0265, NR 036-099 (C-MU)

Effect of Microstructure and Trapping on the Hydrogen Embrittlement Susceptibility of a Ti-Bearing HSLA Steel

by

Michael Francis Stevens
Dept. of Metallurgical Engineering & Materials Science
Carnegie-Mellon University
Pittsburgh, PA 15213

Submitted in partial fulfillment of the requirements for the degree
of Doctor of Philosophy at Carnegie-Mellon University

Accession For

NTIS CRA&I	X
DTIC TAB	☐
Unannounced	☐
Justification	

A-1

November 1984

Abstract

The general hydrogen embrittlement susceptibility of a Ti-bearing HSLA steel has been characterized and correlated with detailed transmission electron and field ion microscopic studies of various microstructures. The hydrogen permeability and trapping in the same microstructures has also been studied through the use of electrochemical polarization and potentiostatic detection. The trapping character of the various microstructures has been determined by comparison with the TEM and FIM results. Hydrogen embrittlement susceptibility has been determined by the use of cathodically pre-charged cylindrical tensile specimens and hydrogen induced cracking of double cantilever beam type fracture mechanics specimens.

The hydrogen permeability studies showed that austenitized and quenched microstructures were composed of essentially low interaction energy reversible trap sites for hydrogen including but not restricted to grain boundaries, solute elements and dislocations. Aging at temperatures between 400°C and 500°C still resulted in a reversible trap population, although the character of trapping was inferred to have shifted to higher capture-to-release rates from examination of the form of the transient hydrogen exit flux. The introduction of cementite in these microstructures was assumed to be responsible. At aging temperatures of 600°C and higher, irreversible trapping of hydrogen was found to occur concurrently with the direct precipitation of the alloy carbide, TiC. As this precipitate coarsened beyond the estimated incoherent interface size range, irreversible trapping capability was lost and reversible trapping with high capture-to-release rate behavior was again found.

Pre-charged uniaxial tensile testing established that the formation of even 10-15 Å diameter "clusters" of TiC could bring about a 50% improvement in ductility compared to microstructures lacking this phase. More complete precipitation of Ti and C as carbide phase at 600° aging resulted in complete intergranular failure and loss of measurable ductility. This was found to be due to concurrent segregation of metalloids to high angle (prior γ) boundaries with the loss of titanium to the carbide phase.

Hydrogen induced cracking studies indicated that both bulk hydrogen diffusivity (as measured by permeation breakthrough times) and diffusable hydrogen content (as determined from permeation time-lag values) are important. In microstructures possessing a relatively high "breakthrough" diffusivity and little or no irreversible trapping (i.e. 400°C aging), low threshold stress intensities and high stage II crack velocities were observed. In a microstructure having a relatively low breakthrough diffusivity and a high density of fine, irreversible traps (i.e. 600°C aging) a higher threshold was found notwithstanding the lower inherent fracture toughness resulting from temper embrittlement.

i

Table of Contents

List of Figures

List of Tables

Chapter 1
Introduction

Hydrogen has been recognized as a generally deleterious solute in many metallic systems since the nineteenth century. Since then, a plethora of scientific and industrial literature has been generated concerning the quite general topic of hydrogen embrittlment.

The wide interest in hydrogen effects on materials stems in part from the va   of environments from which hydrogen may be taken up by a metal host and the suscep.   of many metals to hydrogen. Hydrogen may enter a metal from the gas phase through a surface dissociation reaction or it may be absorbed from the surface as the result of cathodic half-cell reactions accompanying corrosion. Additionally, hydrogen may embrittle a material by causing a fracture mode change (i.e. from ductile to intergranular) or it may more subtly affect the plasticity of the material without causing a fracture mode change[148,155]. At high temperature, hydrogen may react with other solutes in the metal matrix and produce gas bubbles, the so-called "hydrogen attack" phenomenon seen in medium carbon steels[168]. In certain metal systems i.e. Ti and Nb which favor direct chemical reaction with hydrogen, embrittlement may be linked directly to formation of brittle hydride phases[46].

The iron system poses perhaps the most challenging problem since no single mechanism appears adequate to explain the variety of ways in which hydrogen alters the mechanical integrity of iron based alloys, although several have been suggested[169,170,171].

Despite the unanswered question regarding embrittlement mechanisms, a great deal of information relevant to the kinetics of embrittlement in iron and steel has been estabilshed

and consistent trends concerning the affects have been observed. The iron system is first of all characterized by a low equilibrium solubility (0.01 atomic ppm at $25°C$)[120] and a reasonably high diffusivity ($\sim 10^{-6} cm^2/sec$)[120] at $25°C$) in the iron lattice. Measurements of these parameters have revealed that hydrogen interacts quite strongly with heterogenieties within the bulk, termed "traps"[25,26]. Detailed characterization of steel microstructures has shown that various traps, including grain boundaries, dislocations, inclusions and carbides, and solute atoms can be categorized as to the relative strength of their interaction with hydrogen. For the case of inclusions and grain boundaries, trapping at these sites is viewed as a precursor to failure. Additionally, dislocations have been suspected of being "mobile" traps for hydrogen, redistributing hydrogen atmospheres or core populations during plastic deformation[58].

The study and characterization of traps is important since as stated above, certain types of traps will be eventual failure initiation sites. More importantly, observations by many workers of decreased embrittlement susceptibility at sufficiently low temperatures or high strain rates are consistent with the requirement for redistribution of hydrogen under stress[45,175]. If the onset of embrittlement is generally associated with hydrogen redistribution, then this poses a microstructural parameter which may be manipulated to delay or possibly eliminate the embrittlement step in many grades of steel. Particularly promising sources of beneficial trapping in steel are Ti solute additions and Ti precipitates. A direct connection between Ti and decreased susceptibility was apparently first established by Bernstein[47,48,49]. He found that a Ti bearing steel was generally less susceptible to cracking than equivalent Ti-free grades, although the cause was not established. Later, Pressouyre and Bernstein[28,29] and Asaoka[34] proved that Ti and TiC particles were effective traps for hydrogen and could ameliorate embrittlement in some cases. In the related field of temper embrittlement, Ti additions have been found to be beneficial in suppressing this phenomenon also and some workers have claimed that trapping of metalloids by Ti precipitates is also responsible[40,42].

Titanium in solid solution in iron may also affect the plastic deformation properties

in the presence of internal hydrogen. Bernstein[49] found, through measurements of reduced "friction" stress in Petch type analyses, that Fe-0.15% Ti was softened by internal hydrogen. It was suggested at the time, that hydrogen may promote dislocation breakaway from carbon or nitrogen "pinning" points. Kimura[172] and co-workers also found hydrogen induced softening in high purity iron. These workers suggested that Bernstein's observations were caused by the "gettering" of interstitials by Ti and subsequent softening of the purified matrix by hydrogen. The same authors also conducted experiments on Fe -0.6 atomic %Ti and found that this material was hardened by cathodic hydrogen. Titanium-hydrogen complex barriers to dislocation movement were suggested as a possible cause. Titanium additions to experimental alloys have since been found to reduce susceptibility to hydrogen in dynamic testing situations[32,52,53,54].

Hence, a body of fundamental findings concerning the hydrogen compatibility of the Fe-Ti system exists from which some speculation about related composition steel behavior may be attempted. The most logical candidate steels are the variety of HSLA "microalloyed" steels based on titanium. These are reasonable choices since their processing is essentially designed to produce fine alloy carbide precipitates (i.e. Ti(C,N)) which refine the hot-rolled austenite grain size and hence, the transformed ferrite grain size. The later may be further modified by additions of Mn less than 1.5% which promote transformation to bainitic type microstructures rather than polygonal ferritic microstructures[137]. The fine carbides in the ferrite matrix can also give rise to precipitation hardening effects, raising the yield strength of these grades above 700 MPa while retaining high ductility and toughness due to refined grain structure and a high mobile dislocation density. Therefore, these alloys compositionally and microstructurally represent a small deviation from the experimental binary systems which have been studied and comprise realistic structural steel microstructures within which the trends of simple microstructure trapping and plasticity effects can be tested for hydrogen environment usage.

The studies conducted for this thesis utilized an HSLA acicular ferritic steel so that

TiC related trapping and their consequences on hydrogen embrittlement susceptibility could be examined at moderate strength levels (σ_y > 700 MPa). This material was thermally treated in order to produce precipitates with varying degrees of size, density and coherency. The trapping properties have been determined for these microstructures through analysis of transient hydrogen permeation data. The mechanical properties with internal hydrogen have also been determined using uniaxial fixed strain rate and quasi-static fracture mechanics type specimens. Through comparison of these various test results, a better overall understanding of the role of trapping in hydrogen embrittlement is hoped to be gained.

Chapter 2
Literature Review

In a complete review of the metallurgical literature relevant to this study, one must first examine the wealth of research which has been conducted on microalloyed HSLA steels in addition to the detailed studies on Fe-Ti-C model alloys which have served to isolate the effects of Ti on tempering reactions and mechanical properties.

Concurrently, the highly reactive nature of Ti as an alloying element in Fe has prompted numerous studies aimed at determining its role in well recognized, but ill-characterized phenomena, such as temper and hydrogen embrittlement. It is generally recognized that Ti plays a beneficial role here, but the mechanism(s) through which this occurs is(are) not well known in all cases.

Additionally it is necessary to selectively examine the published research which has attempted to relate detailed characterization of microstructure to hydrogen effects on tensile properties as well as sub-critical cracking in ferrous alloys.

2.1. Physical Metallurgy of Ti-HSLA Steels

The use of Ti as a microalloying additive is a relatively recent practice in comparison to the use of more common elements such as Nb and V. Initially its use was limited to that of strengthening and for sulfide shape control[1]. However, the modern applications of these alloying elements (ie. Ti, Nb, and V) in low carbon steels have given rise to "controlled-rolled" steels and "microalloyed" steels. In both cases, multiple benefits stemming from the presence of the carbide formers are realized.

In "controlled-rolled" steels, the precipitation of fine nitrides, carbonitrides or carbides during hot rolling produces an ultrafine ferrite grain size[1,2,3]. The presence of small precipitates (<1000Å) and the fine ferrite grain size produce significant increases in both strength and toughness. The precipitation of the fine precipitates is essential due to the fact that the preferred sites for nucleation are austenite grain boundaries. This effectively increases the recrystallization stop temperature allowing for refinement of the austenite structure by continued recrystallization as well as "pancaking" the austenite grain before transformation, producing a finer transformed structure. Additionally, as for the case of microalloyed steels, microalloy carbide precipitates are instrumental in delaying recrystallization of ferrite in quenched and tempered steels due to the inhibition of dislocation sub-structure movement[4]. This also arises from dislocations being preferred sites for carbide nucleation.

Elements like titanium are also instrumental in inducing a strong crystallographic texture in these steels, usually of the (112) [$1\bar{1}0$] type[5]. As this cube-on-corner texture becomes more intense, the impact transition temperature is lowered, as discussed by Pickering[6]. Meyer has proposed that this strong propensity for a recrystallization texture in interstitial free steels is due to retardation of recrystallization by precipitates[7], in analogy with the effect of AlN particles in aluminum killed sheet steels. The texture hardening in these steels may allow average plastic strain ratio ($\bar{R}$) values in the range of 1.8 to 2.2, offering excellent deep-drawability.

An additional and highly attractive role of titanium is that of sulfide shape control. In normal Al-killed C steels, sulfur is gettered by Mn. These sulfides tend to elongate at hot rolling temperatures due to a relatively low melting temperature. This produces a well known anisotropy of toughness properties as well as an increased tendency towards lamellar tearing. Due to its greater affinity for S, Ti changes the sulfide phase to the carbosulfide $Ti_4C_2S_2$ which has a much higher melting temperature and therefore tends to have a smaller aspect ratio than MnS[7].

As in the case of Si. Ti has a well known affinity for O, N, and C. The thermodynamic strength of this attraction is quantified in Fig. 2-1 taken from Chino and Wada[8]. This pronounced susceptibility for oxide formation in liquid iron requires that the steel be completely Al-killed before the addition of Ti. The somewhat lower, but still substantial attraction for N allows for the formation of the phase TiN in liquid iron. This phase is quite evident metallographically from its sharp-edged cuboidal morphology[7]. Additional findings by Chino and Wada have shown that the solubility of this phase in austenite at $1200^{0}C$ is so limited that it may be considered insoluble.
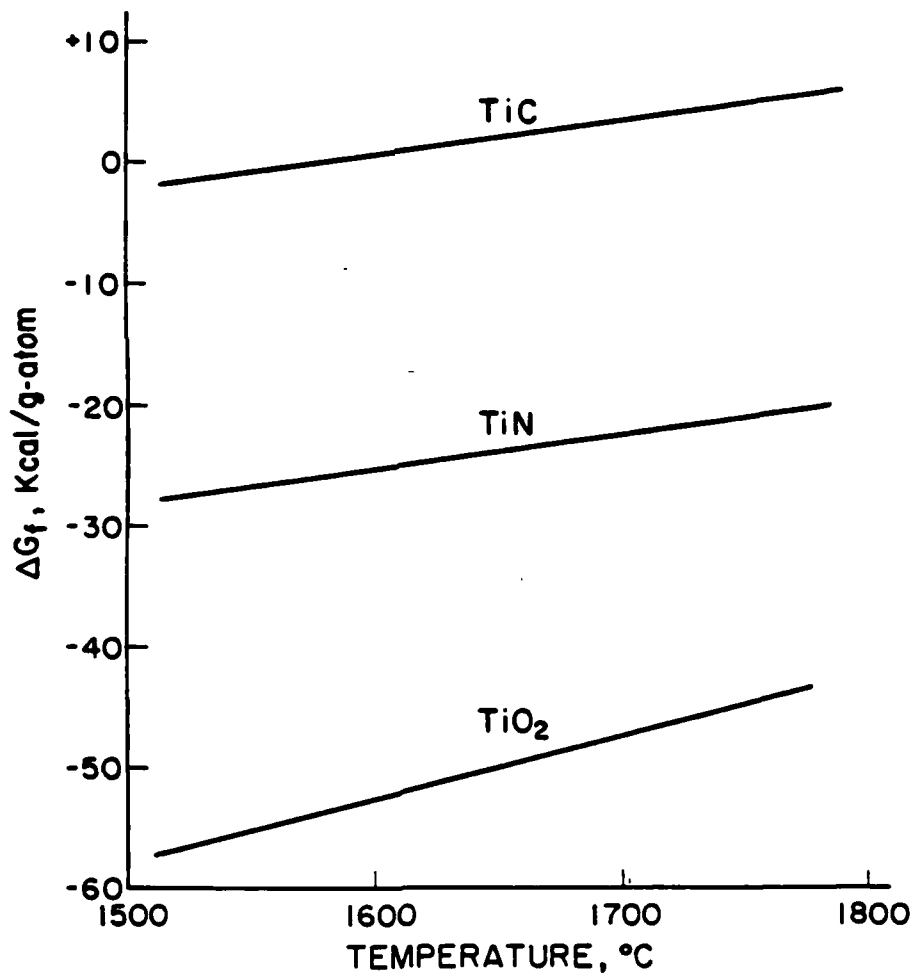
Figure 2-1: Free Energy of formation for TiO_2, TiN and TiC in Liquid Iron; from Chino and Wada[8]

Intermediate between the pure nitride and carbide phases is the formation of the carbosulfide phase. Meyer, Heisterkamp and Lauterborn[7] have characterized this sequence of precipitation schematically as

$$TiN \rightarrow Ti_4C_2S_2 \rightarrow TiC$$
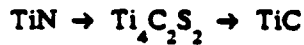
Ultimately any residual Ti left the solution after the reaction of O, S and N will be combined as the carbide phase or retained in solution.

Considerable attention has been given to the precipitation of TiC in steels both from an industrial and fundamental viewpoint. The limited, but substantial solubility of TiC in austenite has been empirically determined by Irvine et.al.[9] and may be described by the equation:

$$\log_{10}[Ti][C] = \frac{-7000}{T} + 2.75 \tag{2.1}$$

where the concentrations are in weight percent and T in °K. The solubility of this phase is shown graphically in Fig. 2-2 This predicts that at least 0.2 wt.% TiC may be dissolved in solution at 1250°C.

Two different precipitated morphologies of TiC in ferrite have been studied. In quenched and tempered low carbon martensitic or acicular ferritic matrices, TiC precipitates at dislocations and low angle boundaries[10,11]. If the austenite is transformed isothermally or by continuous cooling, a banded carbide dispersion may arise due to repeated nucleation of the carbide phase along the γ/α interfaces as they sweep through the austenite grains, as demonstrated by Freeman[12,13]. Campbell[14] showed, in an Fe-12Cr-0.2C alloy, that these interfaces advance by the movement of highly mobile incoherent ledges, as described by Aaronson[15]. The precipitates nucleate along the low energy "ledges" of these interfaces since the risers themselves are too mobile to allow sufficient time for precipitation. In the transformation range 600°C - 800° typical TiC particle diameters may range from 10 - 200 Å in size. Youle et al.[16] have studied the aging behavior of TiC and have found that the TiC phase has a Baker-Nutting type orientation with the surrounding ferrite i.e.
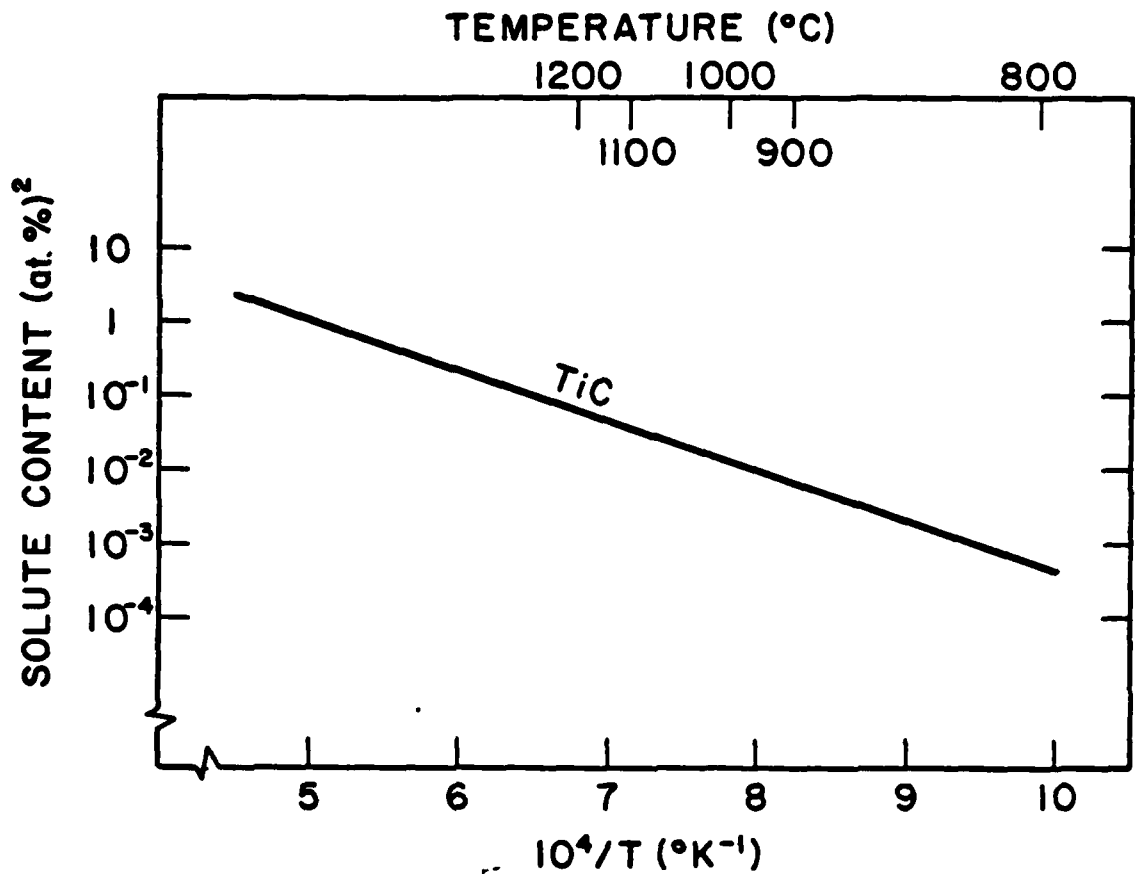
Figure 2-2: Temperature dependence of TiC solubility in austenite.

$$(001)_a \parallel (001)_{TiC} \tag{2.2}$$

$$[100]_a \parallel [1\bar{1}\,0]_{TiC} \tag{2.3}$$

Through ring matching of FIM images they also determined that the particles passed through a classical sequence of coherent ($<30\text{Å}$) to semi-coherent (~ 30-200Å) to incoherent ($\geq 200\text{Å}$). They also found that a spheroidal morphology dominated throughout the aging processes suggesting that surface energy considerations rather than strain energy were dominating the shape.

The effect of the TiC phase on mechanical properties of ferritic steel has been studied in depth by several authors[1,7,9,12,13,16, 17,18,19]. It should be kept in mind that strengthening of the final ferrite phase results from affects of TiC on austenite

recrystallization, texture hardening, sub-grain pinning in ferrite, solid solution strengthening as well as classical precipitation strengthening. Earlier work at U.S. Steel Research on Ti "gettered" iron has revealed that other solutes (both substitutional and interstitial) give rise to alterations of the mechanical response of iron. In a review of this work, Leslie[129] concluded, for example, that Ti(C,N) particles could raise the work hardening rate of iron at small strains. Other interactions with substitutional elements were also suspected, but applications to strengthening in low alloy steels were not discussed. Freeman and Honeycombe[13] characterized the strengthening due to the TiC phase in both quench and tempered and isothermally transformed steels containing 0.55, 0.25 ($\sim$ 0.43 v/o TiC) and 0.13% Ti and a stoichiometric amount of carbon. Maximum hardening occurred on transforming at 600°C although no lower temperature data was discussed. The average particle size in this microstructure was approximately 50Å, determined by FIM. In the quenched and tempered treatment the highest strength was found on aging at 650°C. Strength levels using quench and temper treatments were generally higher, due to the residual stresses, grain refinement and dislocation substructure resulting from the quench. Batte and Honeycombe[20] attempted to isolate the individual contributions to strengthening in the isothermally transformed microstructure and predicted a contribution of more than 550 MPa due to precipitation hardening at a transformation temperature of 600°, compared to only 124 MPa due to grain size refinement. These findings are consistant with similar studies by Herrnstein et al.[19] and Smith et al.[21] Fig. 2-3 shows a continuous cooling diagram developed by the later authors for a 0.06%C, 0.23%Ti steel showing that cooling following a finishing temperature of 650°C can produce strength levels in excess of 100 ksi (690 MPa). These authors attribute the enhanced strength after this thermal treatment to a combination of titanium carbonitride precipitation during transformation from austenite and ferrite grain size refinement. Steels for these applications usually contain anywhere from 0.5 to 2.0% Mn in order to avoid the higher temperature transformation to polygonal ferrite. In their studies of the strengthening of ferrite by titanium, Meyer and co-workers[7] and Gladman et al.[23] have determined that the most effective size range for strengthening by TiC is 20-100Å. This precipitation hardening

effect may be explained through Ashby's[23] treatment of the Orowan theory of dispersion strengthening which in final form is given by

$$\sigma = \frac{5.9f^{1/2}}{\bar{x}} \ln \left(\frac{\bar{x}}{2.5 \times 10^{-4}} \right)$$ (2.4)

where:

σ = uniaxial flow stress, MPa
f = particle volume fraction
$\bar{x}$ = mean planar intercept diameter of particles
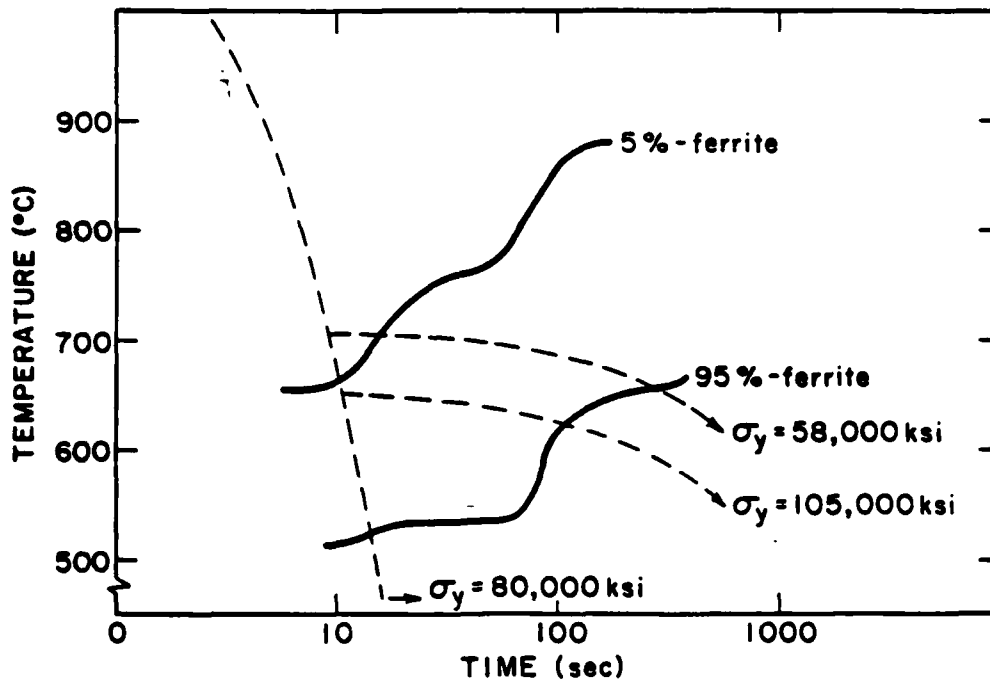
Figure 2-3: Continuous cooling curve for 0.06%C, 0.23%Ti steel showing final yield strength dependence on cooling rate.

Fig. 2-4 graphically compares the predicted strengthening from such a mechanism with estimated experimental values showing good agreement.

The toughness of low-alloy steels depend on many factors. In a review of factors affecting the toughness of alloy steels, Honeycombe[22] lists the following factors that contribute to good fracture toughness:

1. Fine austenitic and consequently fine ferritic grain size.

2. Clean steel with only fine inclusions.
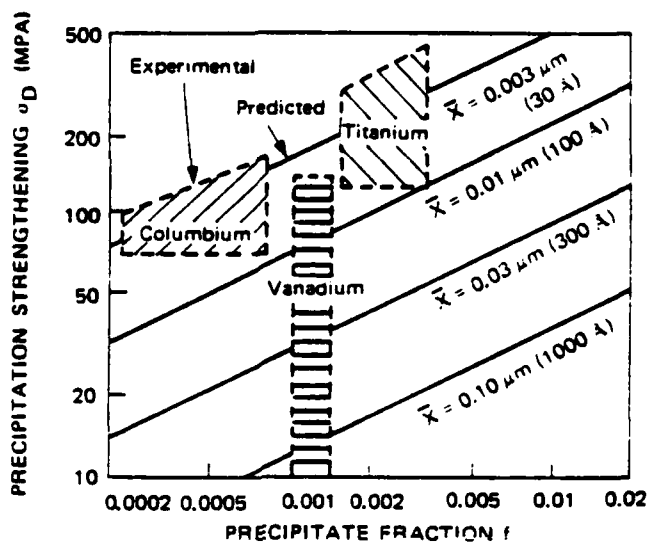
Figure 2-4: Comparison of experimental precipitation hardening in microalloyed steels to Ashby-Orowan model.

3. Absence of coarse carbide particles and grain boundary carbides

4. Small mean free dislocation path

5. Absence of pre-existing micro-cracks

Titanium in small amounts can certainly affect the first four of these factors and the low overall alloy content in HSLA steels provides some insurance against the last by lessening the likelihood of cracking during cooling or quenching.

Titanium, in general, has been shown to lower the notch-impact transition temperature of iron [129]. Freeman's [12] study of a 0.5Ti-0.19%C steel specifically compared the ductilities of isothermally transformed and quench and tempered microstructures. At equivalent yield strengths of approx. 800 MPa, the isothermally transformed specimen showed %RA values 17 times greater than the quench and temper microstructure (85% RA in the former compared to only 5% in the latter). If an equivalent austenite grain size prior to transformation is assumed, the difference must lie in the mode and homogeneity of precipitation as well as the resultant ferrite grain structure and dislocation density. The ferrite is usually polygonal after complete isothermal transformation and strength is primarily derived from the homogeneously dispersed uniform carbide density. In contrast,

In contrast, the strength of the quench and tempered steels is derived mainly from the refined acicular ferrite structure and the usually high ($\sim10^{10}$ cm^{-2}) quenched-in dislocation density. It is also possible that a different transformation texture or interlath orientation match-up may be responsible for these ductility differences. It is even possible that microscopic quench cracking may occur in these steels. These findings warrent more in-depth structure/property characterization for these microstructures.

The role of titanium as an austenite and ferrite grain refiner as well as a sulfide shape controller has been discussed earlier in this chapter. One may imagine that coarse carbide particles would not be a problem in steels containing elements which form very fine carbide dispersions such as Ti, Nb and V. This is true when these steels are transformed above 500°C, however, at lower temperatures the alloy carbide is preceded by the normal sequence of ϵ-carbide followed by cementite, since the rate controlling processes for these phases are the diffusion of carbon in. α-iron and self diffusion in iron, respectively[22,24]. The cementite phase coarsens quite rapidly in the temperature range 400-500°C. Gladman et al.[23] have shown that above a critical size for cementite of about 2-5 μm the impact transition temperature is raised considerably. In addition, a coarse carbide structure may also allow for longer mean free dislocation paths, producing pile-up stress concentrations leading to low-ductility (cleavage) failure. In this temperature regime, an additional effect of alloying elements may also be observed, namely that of retarding the coarsening of cementite[24]. The best known example of this is the action of Si, which segregates from growing cementite particles due to its low solubility in Fe$_3$C. The build-up of Si near these particles repels C due to a highly positive interaction coefficient between these two elements in ferrite. This action of silicon has led to its use in low alloy steels such as AISI 4340 to produce the common 300M grade, which allows tempering in temperature regimes where carbide associated embrittlement would otherwise be observed. The build-up of silicon in the matrix raises the local activity of carbon, slowing the growth of the carbide particle. Additionally carbide formers such as Cr, Mo and W are known to slow coarsening either by entering into the carbide phase or by competing for C with growing Fe$_3$C particles. The

consequences of this are to supress the tempering reactions to higher temperatures and longer times.

2.2. Hydrogen Trapping in Iron

It has been well accepted, since the early study of Darken and Smith[25], that the anomalous hydrogen diffusivity values measured in iron and steel at or near ambient-temperatures are due to microstructural trapping. The overlap of trapping and acute embrittlement susceptibility in many steels hints of a possible connection between the two.

Again, the published literature connected with this phenomenon is considerable, and detailed reviews of previous work have been conducted by several authors[26,27]. This present survey will focus only on relevant previous work to help characterize the trapping capability of Ti substitutional atoms and TiC precipitates in iron and steel.

A highly detailed study of trapping by Ti and TiC in iron has been conducted by Pressouyre[28] and analyses of his results have been published as well. His analysis of trapping was obtained through permeation transients using an electrochemical cell originally developed by Devanathan and Stachurski[33]. His results showed that titanium atoms are essentially reversible, low occupancy traps for hydrogen with an interaction energy of 0.27 eV and incoherent TiC particles were large occupancy, irreversible traps with an interaction energy of 0.98 eV with hydrogen in ferrite. Following these studies, direct evidence for trapping at TiC particles was obtained by Asaoka et al.[34] using high resolution tritium autoradiography. Recently, Brass[178] has studied the hydrogen permeation properties of 42 CD4 (AISI 4140) steel with and without modifying additions of Ti and V. It was found that the carbides in the modified alloy had an approximate composition of $(Ti,V)_2MoC$ and were present as a much finer (<200Å) dispersion when compared to the cementite (M_3C) in the standard alloy. Most significantly, the (Ti,V) modified precipitates were found to be very deep trapping sites for hydrogen, as judged from hydrogen permeability. More recently, Kimura et al.[35] have investigated the plastic flow properties of high purity Fe-0.6 atom% Ti alloys following cathodic pre-charging with

H. These workers found an increase in flow stress and hardening rate when H was present. Since purified Fe specimens displayed softening under similar conditions, it was concluded that the hardening was due to a strong interaction of H with Ti and glissile dislocations.

Iino and Yazima[36] have studied the hydrogen permeation properties of Ti-bearing experimental steels and found a distinct retarda...on in rise time for an increasing Ti concentration, as well as a distinct "intermediate" plateau which was predicted by their model for traps which exhibit diminished release of hydrogen. They concluded from comparison of their permeation transients and models for combined trapping effects that certain precipitates of titanium act as irreversible traps for hydrogen and that titanium substitutional atoms act as reversible trap centers, in confirmation with Pressouyre's earlier findings.

The explanation for a hydrogen interaction with microstructural heterogeneities may be traced to chemical or mechanical origins depending on the particular trap site and host crystal structure. A strong interaction of hydrogen with titanium in steel is immediately suggested by the highly enthalpic value of the first order interaction coefficient, e_{Ti}^{H}, in liquid iron at $1600°C$. Elliott et. al.[37] placed this value at -3.85 compared to values >-0.10 for most other alloying elements in liquid iron. Additionally, the strong attraction of titanium for hydrogen may be rationalized in terms of a large negative ΔG value for the reaction.

$$\underline{TiC}(s) + 2\underline{H} = TiH_2(s) + \underline{C} \tag{2.5}$$

Also, as suggested by Friedel[38], a possible electronic attraction exists since, upon dissolving in iron, hydrogen must ionize and in so doing gives up its electron to the conduction band. Titanium being to the left of hydrogen on the periodic table would be expected to have a somewhat stronger attraction for this "free" electron and the associated hydrogen atom.

The basis for an interaction between hydrogen and TiC particles in ferrite may be based on a free energy of formation value for the reaction

$$\underline{TiC} \ (s) \ + \ 2\underline{H} \ = \ TiH_2(s) \ + \ \underline{C} \qquad\qquad (2.6)$$

as shown by Pressouyre, but the calculated ΔG values are numerically smaller in magnitude than those for this titanium hydride formation. It is more likely that the interaction stems from the high interfacial energy of TiC in ferrite and possible strain fields associated with coherent particles (d < 30Å) and semi-coherent particles (d < 200Å). Asaoka[34] suggests that the interaction stems from a particle matrix interface factor and, in analogy with earlier studies of Lapasset[39] on maraging steels, puts the binding enthalpy near -14.5 kcal/mole. These observations are consistent with the FIM results of Youle et.al.[16] who suggested a high interfacial energy as implied from a persistence of spheroidal morphology for this phase.

The trapping potency of TiC has led to studies aimed at determining its possible use to ameliorate temper embrittlement susceptibility in alloy steels containing Sb and P. Meyers et. al.[40] analyzed trapping of Sb in a Fe-Ti-C alloy. These studies used a Fe-C binary which had been ion-implanted with Sb and Ti. Following annealing at 600°C, the Sb and Ti profiles, as determined by ion backscattering, showed coincidence. This shift in Sb to align with the Ti was taken as evidence of trapping by fine TiC particles, as the latter were readily found through TEM examination. Possible trapping at Ti substitution atoms was not accounted for, although the local Ti concentration far exceeded the stoichiometric quantity required for complete carbide formation.

Pillar and co-workers[41] conducted field-ion analyses of Fe-Ti-C and Fe-Ti-Sb-C alloys and found by direct observation of a particle/matrix interface and quantitative analysis that considerable segregation of Sb to TiC precipitates had occurred. The authors concluded that the segregation was caused by combined chemical and strain field effects.

In a similarly oriented study, Erhart et.al.[42] studied the possible reduction of grain boundary segregation of P in iron through Ti alloying additions. They found that Ti additions to pure iron caused a decrease in P concentration at prior γ boundaries. In

quatenary Fe-Ti-C-P alloys, however, precipitation of TiC caused an enhancement of grain boundary segregation of phosphorus, although at higher C concentrations P segregation was reduced by displacement from the boundaries by C. It was determined that at stoichiometrically matched Ti:C levels, the P concentration at boundaries was lower than for a carbon free Fe-P alloy with an equivalent amount of P. This difference was attributed to trapping of P at TiC interfaces[56].

Although these studies make apparent the fact that Ti and Ti-based precipitates in iron are effective trap sites, the obvious shortcoming of these studies for the most part is that no detailed correlation between precise microstructural parameters such as precipitate morphology and distribution, free Ti content, and trapping properties has been made. Therefore it should be kept in mind that most of the trapping properties of these various studies have been deduced but not proven.

2.3. Hydrogen Effects on Mechanical Properties of Fe-Ti Alloys

The literature reviewed in this section will deal most specifically with previous work on the role of microstructure on hydrogen embrittlement of low-alloy steels. Additionally, previous studies which attempted to isolate the role of Ti and TiC precipitates an hydrogen embrittlement susceptibility will also be covered.

The effects of H on iron and iron based alloys have been studied extensively and it is not our purpose here to exhaustively review this body of literature. Particularly useful reviews of the literature have been conducted by Hirth[27], Bernstein and Thompson[43,44], and Birnbaum[45,46].

Specifically, Bernstein[47,48,49,50] conducted the earliest studies which characterized the effect of Ti on mechanical properties of hydrogen charged iron. In his comparison of deformation of partially decarburized iron and Fe-0.15%Ti, he found that hydrogen increased the measured Petch slope in the former while having minimal effect in the latter case. This difference was accounted for by the scavenging effect of Ti on C and N, and

also the predicted attraction of H for Ti and Ti precipitates in Fe. It was also determined that the friction stress in both cases was lowered by dissolved hydrogen. Curiously, the aforementioned results of Kimura[35] indicated a pronounced hardening upon uptake of hydrogen. These descrepancies have not been accounted for to date.

In a study of cathodic charging induced cracking in iron, Bernstein[47] found that the gettering of interstitials by Ti promoted intergranular cracking compared to other partially purified iron grades. Bernstein and Rath[50] did determine that for a given grain size and charging current density, Ti gettered iron exhibited fewer cracks than Ferrovac iron. Also, from the kinetics of the frequency of damage, a plateau for the Fe-0.15Ti alloy, absent in the Ferrovac iron, was revealed. Pressouyre[32] examined these findings in greater detail and he found that increasing Ti concentrations could decrease the extent of cracking in iron by reversible trapping and in so doing could also delay the kinetics. In contrast, irreversible traps, in the form of TiC particles did not effect the extent of damage but could change the kinetics and prolong the low damage "plateau" during charging. Similar static charging results have been reported by Takahashi[51] for fishscale formation in an enameling steel. These researchers determined that a low density of surface fissures corresponded to a high density of fine "coherent" TiC precipitates and a low measured value of hydrogen diffusivity.

The ameliorating effects of Ti on embrittlement of iron have also been observed under dynamic loading conditions by Pressouyre and Bernstein[32], Kuslitski[52], Archakov[53], and Stevens et al.[54] In particular, Pressouyre and Bernstein modelled the interaction of internal hydrogen with mobile (dislocation) traps and fixed (Ti atoms, TiC particles, grain boundaries, etc.) traps. In this model, the authors considered that moving dislocations could "carry" hydrogen and deposit it at stronger irreversible trap sites, such as TiC. Ti atoms were considered as sources of hydrogen for the moving dislocations and as such may be deleterious to overall resistance. Their experimental results coincided with the model predictions; the best ductility was found for material containing a fine dispersion of TiC particles and a low concentration of free Ti. Large TiC precipitates present at grain

boundaries promoted an intergranular failure mode. The work of Stevens et al. generally demonstrated the same trend in properties. In this study, performed on the identical steel heat reported in this thesis, it was demonstrated that enhanced ductility following cathodic charging corresponded with direct precipitation of a fine (20-40Å) TiC precipitate population. In an unaged and charged condition, this material developed no measurable %RA whereas after aging at 600°C and an equivalent charging process, the same uniaxial tensile test produced almost 60 %RA at failure. It should be noted that these reported results represent a contradicting trend in properties by comparison with the present findings on nominally the same alloy. Although this will be discussed later in this document, it is felt that the discrepancy lies in the inhomogeneous distribution of tramp elements (P and S) and associated inclusions in this heat.

An additional microstructural consideration which has been observed[55] to be important in determining hydrogen embrittlement susceptibility is the presence of inclusions. It is well known that macroinclusions (> 1μm) participate in the early stages of ductile separation and thus greatly affect the fracture strain in the absence of hydrogen[56]. In the presence of internal hydrogen these inclusions are deleterious traps as they are preferred crack initiation sites. Under the influence of an external stress, large MnS inclusions as well as coarsened carbide particles produce a stress concentration in the microstructure which may induce a hydrogen flux to the region. Dislocation transport associated with plastic relaxation in these areas may enhance the hydrogen flux, in the manner suggested by Bastien and Azou[57], Tien et al.[58], and Louthan et al.[59]. Once accumulated near these particles, the hydrogen may recombine, possibly aided by the chemistry of the inclusion, to form a void or it may induce cracking, as shown by Iino[62,151]. Craig and Krauss[60] have observed flat fracture zones emanating from MnS type inclusions in a 4130 steel. A fracture mode change to one displaying tear ridges was observed in this study similar to those found by Takeda and McMahon in HY-130 steel[61].

2.4. Temper Embrittlement in Fe-Ti Alloys

Since the conclusive work of Steven and Balajiva[63] which proved that Sb, P and to a lesser extent, Sn and As were the primary cause of temper embrittlement, many studies have been conducted to understand the microstructural parameters necessary for the manifestation of this phenomenon. A vast majority of the work in this country has been conducted by McMahon and co-workers. An excellent review of grain boundary phenomena in iron and steel has been prepared by McMahon as well as by Briant and Banerji[65] and Seah[66].

As pointed out by Low[70], integranular fracture may be induced by at least two different causes: 1) grain boundary precipitates or 2) grain boundary impurity segregations. This survey will deal primarily with the latter and specifically the role of Ti in mitigating such behavior.

Although the low temperature fracture mode in iron is normally transgranular cleavage, it is possible to induce an intergranular failure mode through high temperature quenching. Early work of Rees and Hopkins[68] suggested that this was due to segregation of oxygen to these boundaries. Their findings were later substantiated by studies of McMahon[69], Low[70] and Kumar and Raman[71]. These workers all found that C could modify this behavior by scavenging O at boundaries if allowed to segregate during slow cooling. Rellick and McMahon[72] later elucidated the role of oxygen in this phenomenon by adding Al and Ti as getters for oxygen. Both of these additives were found to eliminate intergranular failure although Al was judged to be more effective in this role. Jolly and Goux[73] have found a similar effect of Al and Ti in iron although S was held responsible. Rack[74] later suggested that the reduced ability of Ti to suppress intergranular failure compared to Al was due to titanium scavenging of other elements such as C, weakening the deoxidizing effect. He additionally attributed better low temperature properties of Fe-Ti alloys to the elimination of coarse carbides which were present in Fe-C and Fe-Al alloys. Increasing titanium contents somewhat counterbalanced these observed

gains by increased solid-solution strengthening of the ferrite. It should be noted that these results are further supported by the aforementioned hydrogen induced cracking studies of Rath and Bernstein[48,50].

Titanium has also been analyzed for its effects in more conventional two-step temper embrittlement, a phenomon often observed in alloy steels tempered in the range of 600°C and either slow cooled through the temperature range 375°-560°C or subjected to service temperatures in this range. Generally, P and Sb are the usual segregating species in these cases.

Ohtani et al.[75] have found that Cr may enhance the segregation of these elements and Ni may cosegregate with the embrittling elements. Initial studied by these authors concluded that Sb (and P) doped 3.5%Ni-1.7%Cr alloys were highly embrittled due to a cooperative build-up of Ni and Sb at grain boundaries. This affect was rationalized in terms of an earlier model of Rellick and McMahon[77] which suggested that the segregation of Sb resulted from solute redistribution during carbide precipitation rather than equilibrium segregation. By gettering C, Ti prevented the low temperature formation of M_3C type carbides, thereby eliminating embrittlement. In a later study these same authors re-evaluated their findings to conclude instead that a benign Ni-Ti interaction occurred[78].

In contrast to this approach, several authors have attributed the beneficial effect of Ti as well as other carbide formers such as V and Mo to their direct interaction with Sb and P in solution. Graham and Yen[79] studied the segregation kinetics of P in a Ti bearing Ni-Cr steel and found a marked decrease in P segregation to free surfaces and concluded that the Ti addition lowered the concentration of P in solution. Indeed the work of Kaneko et al.[80] earlier demonstrated that Ti readily precipitated P as phosphides in a-iron. Guttman[81] has suggested that Ti may have a similar affect on Sb.

Relevant to these studies are the aforementioned studies of Meyers et al.[40] and Erhart et al.[42]. The study of Meyers' established a correspondence between Ti and Sb profiles in iron and suggested that this was due to trapping by TiC precipitates. These

authors, however, did not account for solute Ti interactions with Sb, which certainly were warrented in light of the high Ti:C ratios in their material. The study of Erhart et al. established that an addition of 0.18% Ti to iron could reduce grain boundary concentrations of P from above 30% to less than 5%. In systems containing C, this ability (to reduce segregation) was reduced at all but very high C concentrations. Spitzig[177] also found that the detrimental effects of phosphorous on the impact transition temperature of Ti gettered Fe was reduced in the presence of carbon. It was concluded that some trapping at TiC interfaces occurred since the P concentration at boundaries with stoichiometric Ti and C additions was lower than for higher Ti:C ratios. Recent studies by Pickering et al.[56] using FIM techniques demonstrated, however, that P was rejected from the vicinity of a TiC particle in iron and did not segregate to the boundary to any great extent. The results of these studies thus do not allow a conclusive decision regarding the nature of metalloid trapping (and hence amelioration of temper embrittlement) by Ti or TiC.

Additional support for the generally beneficial effects of alloying elements on temper embrittlement has recently been provided by Ustinovshchikov[83]. In this study, the author assessed the role of the carbide formers Mo, V, and Cr and the sequence of precipitation on transition temperature and fracture mode in a series of steels. In all cases, the results revealed that the precipitation of the equilibrium carbide phase (Mo_2C, VC or Cr_7C_3) was accompanied by an increase in impact transition temperature and an increased trend for intergranular fracture. It was concluded that carbide formers present in solid solution retain P due to a strong interaction energy, suppressing the diffusion of the latter to grain boundaries. When the carbide former is depleted from solid solution, P is free to segregate to grain boundaries inducing the intergranular fracture mode.

Finally the possibility of combined temper and hydrogen embrittlement has been studied by several authors[43,64]. Early evidence for this was provided by Cabral et al.[84] using a Ni-Cr steel. When temper embrittled at 500°C, the material displayed a lower threshold for cracking in an H_2SO_4 solution as well as a fracture mode change from

transgranular to intergranular. Similar results were found by Yoshino and McMahon[85] and Briant et al.[86] in an HY-130 steel.

Although these trends have been repeatedly demonstrated, no adequate mechanism of the hydrogen-impurity interaction has been developed. It is interesting to note that many of the known embrittling segregants (Sb, Sn and P) are "poisons" for the recombination reaction of hydrogen, as shown by Berkowitz and McCright[87]. It may then be imagined that the boundaries may be preferred sites for hydrogen ingress at the surface, as suggested by Latanision and Opperhauser[89] for nickel. For the case of internal hydrogen, it is not known if hydrogen and the impurities merely add their degrading effects on cohesive strength or whether a more complex synergism exists through which the interface is weakened.

2.5. Hydrogen Induced Crack Nucleation and Growth

The use of fixed strain rate experiments such as smooth tensile tests have proven useful in characterizing materials of high inherent ductility, but are not particularly useful for understanding the mechanisms of hydrogen induced failure nor do they reveal the kinetics of the process. An alternative and widely accepted technique is to measure the kinetics of crack growth due to a driving force such as the Mode I stress intensity factor, K_I. This technique has been used extensively for stress corrosion cracking and hydrogen embrittlement testing[90].

Wiederhorn[91] was the first to recognize the general response of crack velocity versus stress intensity in a "static fatigue" test and this relationship is graphically depicted in Fig. 2-5. Stages I and II are generally believed to arise from an environmental influence on the material and Stage III is an intrinsic, unstable crack extension region. The review here will focus on stages I and II; empirical findings will be covered first followed by previous attempts to model the results.

Studies of Stage I cracking may be considered essentially as attempts to define the

CRACK
GROWTH
RATE
(LOG SCALE)
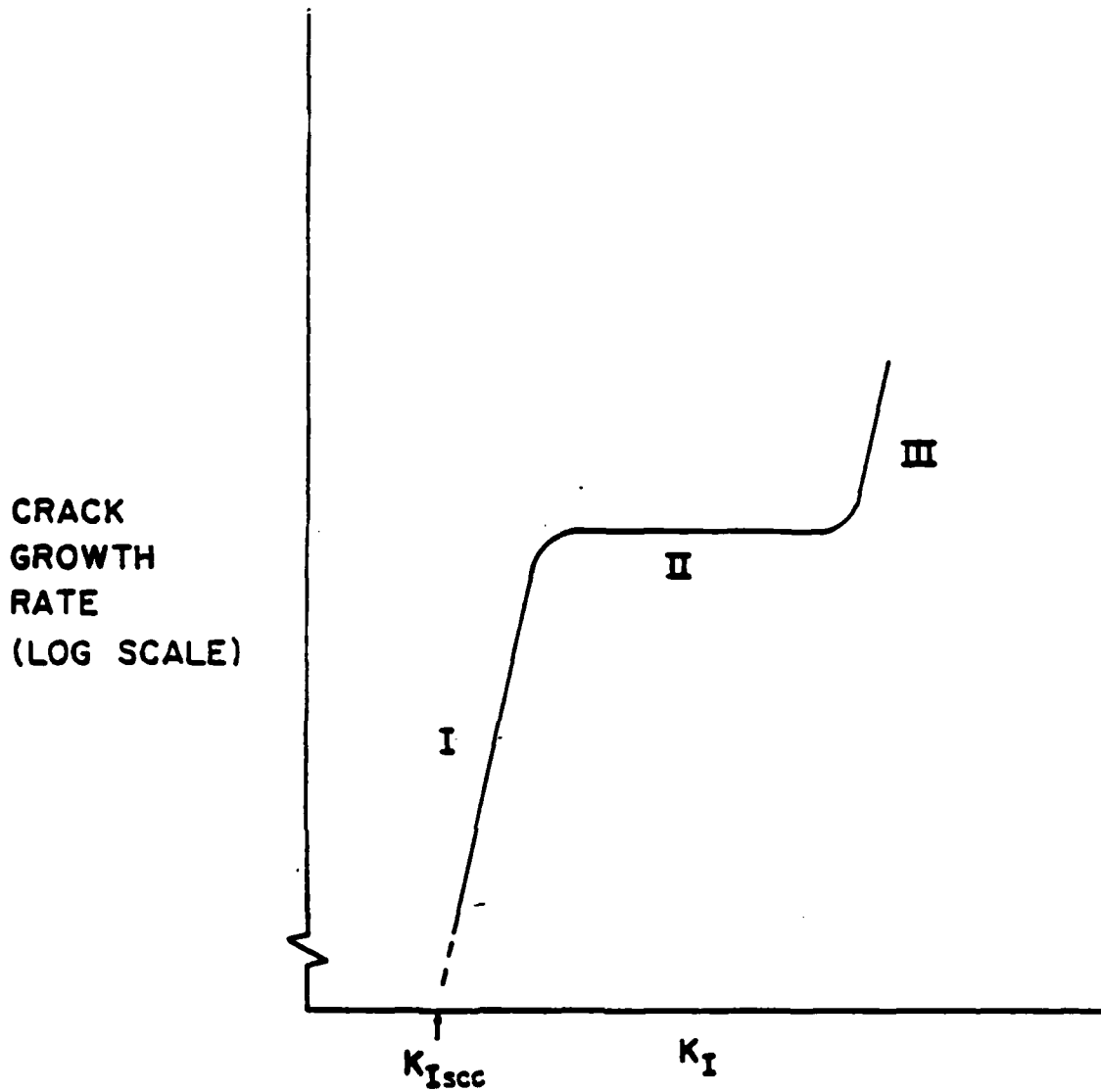
Figure 2-5: Schematic form of environmental cracking
kinetics showing three stage behavior.

threshold K for cracking in that environment. Williams and Nelson[92] have reviewed a

great body of data and found in general that the reported K_{th} values for steel increase

proportionally to T^n where n = 1.4 to 2.0 and decrease with log P, for studies conducted

in pressurized gaseous H_2. Additionally, the threshold values tend to increase with

decreasing strength level. Interestingly, there was no temperature dependence of K_{th} for

the same materials (4130) tested in distilled water. The explanation most likely lies in

the importance of temperature in determining the gaseous surface reaction kinetics as

opposed to a relatively insignificant role in the aqueous reactions in the temperature

regime studied. The relationship with pressure cannot be directly explained by a Sievert's law relationship since the observed relationship was

$$K_{th} \sim P^{-0.2} \qquad\qquad (2.7)$$

A possible explanation for this discrepancy is an effect of absorbed hydrogen on local plasticity and the crack tip radius, hence altering the K level. There has been no explanation for this effect to date. The effect of strength level is consistent qualitatively with an increased tendency for crack tip blunting and a lessening of the stress gradients ahead of the crack tip, as discussed by Rice[93]. This would require more hydrogen over larger volumes of material to operate the cracking mechanism. This is dependent, of course, on the microstructure which will determine the operative mechanism. In general, previous workers have found that refined grain sizes as well as precipitates (carbides and inclusions) and improved cleanliness (for improved grain boundary integrity) all contribute to increased threshold values[27].

Stage II cracking displays a lessened dependency on K and in some cases, may become virtually independent of K. For the latter case, Nelson and Williams[94,95] and Wei and co-workers[96,97,98] have attempted to quantify the combined process kinetics by examining the relationship of $\log v_{II}$ versus $1/T$. At low temperatures in gaseous H_2 ($0°C > T > -100°C$) the activation energies are consistent with hydrogen diffusivity in the material. At higher temperatures there is an abrupt change in properties and the observed stage II crack velocity begins to decrease with increasing temperature, probably reflecting a shift in surface reaction equilibria or kinetics. Gangloff and Wei[98] found that the pressure dependence on the transition temperature followed a Clausius-Clapyron type relationship yielding a "heat of transformation" of about 50 kJ/mol for two different maraging grades. The meaning of this value was not suggested at the time. Williams and Nelson[69] previously showed that the stage II velocity could be made to further increase with increasing temperature, by partially dissociating the hydrogen gas, further suggesting a shift in surface reaction behavior.

The dependence of v_{II} on H_2 pressure does vary with temperature as was demonstrated by Nelson and Williams[94]. At low temperatures, where thermally dependent growth does follow an Arrhenius type relationship, a Sievert's law dependence is observed. In aqueous conditions the stage II velocity for 4130 steel is highly sensitive to temperature, as was found in H-11[99] and 4340[100]. The absence of apparent Arrhenius type behavior in these studies suggests that the surface entry reactions dominate the kinetics of crack growth for this test configuration.

The complications arising from surface reactions either in gas phase or aqueous environments has prompted some work on pre-charged crack propagation specimens, particularly by Gerberich and co-workers[101,102]. In all of these studies, well defined thresholds and stage II behavior in general have been found, further supporting the general role of dissolved hydrogen in sub-critical cracking. The following section of this review will cover these studies of internal hydrogen induced cracking as well as associated predictive models.

Although the environmental cracking studies mentioned above have not conclusively identified the exact mechanism(s) of hydrogen embrittlement, some important features of the embrittlement process in general have become better understood through this technique. Most notable are the contributions of Troiano[103], in particular his proposal that the triaxial stress field at the tip of a stressed crack could produce activity gradients which would induce long range hydrogen migration. Li, Oriani and Darken[104] developed a relationship for the chemical potential of a species in a stressed matrix which can be related to an equilibrium concentration,

$$C = C_o \exp\left[\frac{V^*\sigma}{RT}\right] \tag{2.8}$$

where V^* is the partial molar volume and σ is the hydrostatic stress. Coupled with fracture mechanics estimates of the stress field distribution around mode I cracks, several workers have attempted to then model cracking kinetics. Oriani's[105] decohesion model predicts crack growth when the local normal stress to the crack plane reached the

maximum cohesive strength, which could be lowered by a sufficient quantity of dissolved hydrogen. This model is limited in that valid crack tip radius values are needed and in that it does not correctly predict crack growth dependency on H_2 pressure in Stage I. van Leeuwen[106] later attempted to explain Oriani's data by introducing a crack tip opening displacement factor δ_i, which was developed by Burdekin and Stone[107].

$$\delta_i = \frac{K^2}{2E\sigma_y}$$ (2.9)

and found a good fit between his predicted relationships of H_2 pressure vs K and Oriani's data.

Gerberich and co-workers[102] attempted to model internal and external hydrogen induced cracking using continuum elastic-plastic fracture mechanics. Their model is based primarily on the pressure tensor gradient as the driving force for hydrogen diffusion in the crack tip vicinity. For the case of internal hydrogen, stage I cracking is assumed to be controlled by a primarily elastic field induced gradient, giving an enrichment at threshold of:

$$C_{cr} = C_o \exp\left\{\frac{2(1+\nu)\bar{V}_H K_{Th}}{3(2\pi r)^{1/2}RT}\right\}$$ (2.10)

The value of r then becomes the crack jump interval. Gerberich compared empirical values of r from his own data and that of Oriani and Josephic[157], to Rice's[93] proposed position of maximum normal stress, $2\delta_i$ where:

$$\delta_i = \frac{K^2}{2E\sigma_y}$$ (2.11)

and found good agreement again. Assuming crack growth increments to be on the order of a grain size, d, these authors finally arrived at a value for crack velocity

$$\frac{da}{dt}\bigg)_I = \frac{2(1+\nu)C_o D_A \bar{V}_H K}{3d^{3/2}RT(C_{cr}-C_o)}$$ (2.12)

which predicts the expected linear dependency on K. The same authors assumed an

elastic plastic gradient for stage II growth and for a constant crack tip radius derived the following crack velocity relationship.

$$\left.\frac{da}{dt}\right)_{II} = \frac{9\,C_o\,D_A\,\overset{\star}{V}_H\sigma_{ys}}{2d\,RT\,(C_{Cr}-C_o)} \qquad (2.13)$$

It was determined later that the crack tip radius was not constant but rose linearly with stress intensity. The appended relationship was then

$$\left.\frac{da}{dt}\right)_{II} = \frac{3C_o\,D_A\,\overset{\star}{V}_H\sigma_{ys}}{dRT\,(C_{Cr}-C_o)}\ \ln\left[\,1 + \frac{d}{\rho\,(K_I/\sigma_{ys})}\,\right] \qquad (2.14)$$

which curiously predicts a decreasing velocity for increasing K level. Finally the authors consider Stage III cracking as a plastically controlled region and accordingly modify the stress field assumption to Hill's slip-line field equation in plane strain yielding:

$$\left.\frac{da}{dt}\right)_{III} = \frac{9\,C_o D_A\,\overset{\star}{V}_H K^2}{2Ed^2\,RT\,(C_{Cr}-C_o)} \qquad (2.15)$$

The predictive capabilities are limited since crack path and growth step distance must either be known or determined by experiment and the value of the term

$$\frac{D_A C_o}{C_{Cr}-C_o} \qquad (2.16)$$

strongly determines the rate of crack growth. Assuming $D_A = 2.2 \times 10^{-7}$ cm^2/sec, Gerberich estimated C_{cr} to be $2C_o$. It is obvious that the ambiguity surrounding the values of D_A, C_{cr}, and C_o make a critical assessment of Gerberich's model difficult at best. Plastic zone trapping and general microstructural effects on D_A have not and probably cannot be accounted for. Additionally, this model can only account for a single fracture path and it relies on a knowledge of the initial hydrogen distribution.

By the most analytical approach to hydrogen induced cracking is that of van Leeuwen[106,109,110].He effectively treats hydrogen induced cracking as a repetitive initiation

step by looking at the stress altered transient concentration gradient and assuming that crack growth will occur when the concentration reaches a critical value at some point in the plastic enclave. In the simplest form, the crack will grow a distance, l, after the passage of a time, t_c, to build up the critical concentration, C_c; hence:

$$v = \frac{l}{t_c} \tag{2.17}$$

To a first approximation, this distance may be taken as the plastic radius:

$$r_y = l + \rho/2 \tag{2.18}$$

and using the thin film solution to Fick's law gives:

$$l + \rho/2 = 2(Dt_c)^{1/2} \tag{2.19}$$

and

$$v = \frac{4Dl}{(l+\rho/2)^2} \cdot \tag{2.20}$$

Using the slip line field solution for the stress distribution in front of the crack, he showed that:

$$K = p_c \, \sigma_y \, (2\pi)^{1/2} \, (l+\rho/2)^{1.5} \, (l+\rho)^{-1} \tag{2.21}$$

Using appropriate values of p_c, the plastic constraint factor, and ρ, this simple analysis appears to work well for high strength steels. Inclusion of the stress dependent terms in Fick's Law involves a solution to the relation:

$$\frac{\partial C}{\partial t} = -\nabla J = D\nabla^2 C - \frac{DV_H}{RT}(\nabla C \cdot \nabla \sigma) - \frac{DV_H}{RT}C\nabla^2\sigma \tag{2.22}$$

where the hydrostatic stress state, σ, may be assumed to be elastic, viz.

$$\sigma = \frac{2}{3}(1 + \nu) \, \frac{K}{(2\pi r)^{1/2}} \, \cos\frac{\Theta}{2} \tag{2.23}$$

or plastic

$$\sigma = \sigma_y \left[\frac{1}{2} + \ln(1 + \frac{x}{\rho}) \right] \qquad (2.24)$$

It is obvious that both of these authors have made numerous assumptions about the exact mechanism of crack growth and each have admitted the limitation of their respective model. The uncertainty in ρ, the crack tip radius is certainly the most salient weakness. Gerberich[102] attempted direct observations of this during his tests but these measurements were made on the specimen surface. The role of dislocation density, sub-structure and slip mode has largely been ignored as well as possible contributions to hydrogen flux by moving dislocations. An additional question arises concerning the prediction and observations of a decreasing crack velocity with increasing stress intensity. Although the simple models of Gerberich and van Leeuwen predict this behavior, it is clear that an alternate cause may be the observation of crack branching and toruosity often observed at nearly constant crack growth rates. Brown[90] rationalized that in stage I, a side branch to the main crack would experience a lower K value and would be suppressed by the kinetic advantages of the strong K dependence of the main crack, which itself would continue to shoot forward. However, in Stage II, a side branch would not experience a crack rate penalty, due to the insensitivity to K, hence crack branching should be expected when the crack velocity becomes constant. Carter's[111] analysis concluded that both a constant velocity and critical value of K, K_{Ib} were necessary for crack branching. Earlier, Clark and Irwin[163] suggested that branching may be encouraged by the fact that the normal stress at a $60°$ incline to the crack plane was greater than that stress normal to the crack plane. An attempt to identify experimental parameters which may be manipulated in order to control (or eliminate) this phenomenon has been made by Interrante and Low[112] from a study on 2-1/4Cr-1Mo steel where it was found that crack branching was encouraged by high hardness and an L-T orientation to the original plate. It was also observed that branching could be inhibited by wax-coating all but the notch plane prior to immersion in the aqueous test medium. Alternate possibilities lie in the shape of the plastic zone. An analysis by Tuba[162] predicts a maximum shear stress (and extent of

plastic zone) at an acute angle of 69° from the crack plane. If hydrogen can affect a plastic instability, as suggested by Goldenberg et al.[148] and Lee et al.[155] cracking will tend to occur along characteristic slip lines. An addition contribution to this may be dislocation transport and enrichment along these trajectories[147].

The studies of hydrogen induced crack growth using external sources have, in retrospect, been hindered by the complexity surrounding hydrogen entry into the test material as well as an inability to sufficiently define the state and distibution of stress at the crack tip region. Studies of internal hydrogen induced cracking are a logical circumvention of the first of these problems; however, the latter will still exist. Hydrogen induced cracking using an internal hydrogen source should yield more information pertaining to the relative ability of the microstructure to deliver hydrogen to the highly stressed region. By controlling the trapping characteristics of the matrix, it should be possible to affect the cracking kinetics in a predetermined way. Certainly an effect on Stage II cracking may be expected if transport of a critical hydrogen flux to the crack tip is the controlling step. An influence on Stage I may even be observed if the concentration of diffusing hydrogen is altered by the introduction of irreversible traps. Therefore, combined study of trapping and hydrogen induced cracking is a likely candidate for expanding our general knowledge of environment induced cracking.

2.5.1. Assessment

The preceding review of the literature has certainly revealed the depth to which previous research has gone to establish the action of titanium in the physical metallurgy of iron and low alloy steels. It has been well characterized that small quantities of titanium may strongly influence the strength and ductility of microalloyed steels. This is principally achieved through the precipitation of Ti(C,N) at austenite grain boundaries during hot-rolling, thus inhibiting recrystallization and grain growth of this phase prior to transformation. The fine carbonitride produces a precipitation hardening effect while the refined grain structure leads to both enhanced strength and toughness. Two distinct

morphologies exist for TiC; one is produced through quench and aging where the carbide precipitates heterogeneously at dislocations and grain boundaries and the other results from repeated nucleation along glissile γ/α boundaries during isothermal or continuous transformation. Although the strength levels of alloys processed using the latter scheme are well described in terms of classical precipitation strengthening theory, there appear to be some curious strength/toughness combinations resulting from the isothermal transformation mode. This is a likely area for future structure/property investigations on microalloyed steels. It has also been observed that titanium imparts a favorable inclusion shape control effect by forming non-deformable sulfides. This above effect may be partly responsible for enhanced toughness and stress corrosion cracking resistance.

As regards the role of Ti on hydrogen embrittlement susceptibility, there appears to be a consensus opinion that this element is generally beneficial, although an exact reasoning is far from established. Pressouyre and Bernstein[29,30,32] as well as others[178] have well established the effect of solute Ti and TiC precipitates on the diffusivity and permeability of H through iron. These studies have shown that the diffusivity of H in iron is lowered by the presence of solute Ti through an apparently low energy reversible trapping effect. More significantly, several authors have concurred that a more potent, irreversible trapping effect of TiC precipitates takes place. Tritium autoradiography has apparently established this directly for larger sized carbides, but there is disagreement concerning the cause of this strong trapping and little or no information as to the role of interfacial structure (coherency). A better correlation between TiC size, coherency and trapping behavior is needed. Additionally, Bernstein[47] and Kimura et al.[35] have conducted studies on relatively pure, Ti "gettered" iron in order to observe the more fundamental effect of solute H on flow and friction stresses. Although both concluded that titanium or titanium precipitates affected the results, these studies arrived at different conclusions. Better controlled tests of this type must be undertaken in order to fully understand these effects. For example, charging induced damage in this type of experiment has already been identified as being responsible for so-called "softening" effects.

It has also been seen that titanium as well as other reactive elements, may enhance a steel's resistance to temper embrittlement apparently due once again to an attraction between the culprit metalloids (P,S,Sb) and titanium. Unfortunately, the beneficial action of titanium is even less well established here than in the hydrogen embrittlement studies. Although occlusion of P and Sb at TiC interfaces has been suggested, there is ample contradictory evidence which suggests that the most severe temper embrittlement *accompanies* precipitation of the carbide former (i.e. Ti). This discrepancy is not only important in its own right, but it holds serious consequences if TiC or similar strong hydrogen traps are to be used in commercial grade steels. If the precipitation of strong, effective hydrogen traps is accompanied by a temper embrittled microstructure, then alternate means must be introduced in order to independently control the temper embrittlement phenomenon, such as multiple alloying. This is done already in NiCrMoV steels where Mo is the principle carbide former and V is added to (presumably) stabilize the segregating species[165].

Finally, previous work aimed at understanding the kinetics of hydrogen embrittlement through the use of fracture mechanics type specimens has been reviewed. These experiments have met with limited success mainly with materials of sufficient strength where the complicating effects of crack tip plasticity could be minimized. It is generally accepted that hydrogen induced cracking in these tests is preceded by diffusion of solute hydrogen to the highly stressed region in front of the crack tip. Advances in the use of this technique seem limited mostly by a lack of knowledge of the shape and scale of local plasticity at the crack tip and how the stress field is affected by the plastic zone shape. This problem is compounded by the evidence collected by Goldenberg *et al.*[148] and Lee *et al.*[155] which indicates that slip and plasticity may in themselves be altered by the presence of hydrogen. In spite of these difficulties, there is ample need to examine the role of trapping in tests of hydrogen induced cracking kinetics. It is conceivable that, under fixed hydrogen source concentrations and strength levels, the presence of traps may influence both threshold K levels and Stage II cracking.

Chapter 3
Outline of Experimental Approach

The principal aims of this study have been to expand upon the findings of earlier researchers, notably Pressouyre and Bernstein[28,29,30,31,32], on Fe-Ti based alloys and their related hydrogen embrittlement and trapping behavior. These authors established a close tie between effects of Ti and Ti precipitates on hydrogen permeability and embrittlement susceptibility in model alloy systems. The extent of embrittlement in previous work has been determined through monitoring of static cathodic charging induced cracking (no applied stresses) and ductility losses in tensile tests. These techniques lend themselves well to studies of materials of low strength and high toughness which are not highly sensitive to typical hydrogen sources. The comparisons of suceptibility to microstructurally controlled diffusivity are nonetheless of importance, but may not be representative of the more complex albeit related, low-alloy steel response. This can be envisioned by consideration of a stressed structural component possessing a sub-critical crack-like flaw. The stress state in this situation is likely to comprise much higher tensile stresses and likely a triaxial configuration. In addition, these stresses may be quite localized in comparison to the effective component size and hydrogen source. Crack growth kinetics may be altered by hydrogen trapping in such a situation; however, this type of embrittlement is only likely to occur in alloys possessing sufficient strength so that plasticity and related crack tip blunting (or arrest) adopt only a secondary or minor role.

The material and experiments described herein were chosen with these considerations in mind. The principal alloy chosen, although not a classified grade is quite close in

composition, microstructure and mechanical properties to a number of commercial acicular ferrite, HSLA type steels which obtain their strength primarily from a refined ferrite grain size and microprecipitation hardening. In this case, the precipitates were TiC(N) and therefore the trapping of hydrogen at these particles, as demonstrated by Pressouyre[28] and others[34,178], may be examined in this steel. Differences in trapping behavior were effected by first solutionizing the alloy followed by aging at various temperatures, in order to vary the size, density, coherency and extent of precipitation. These parameters were characterized as closely as possible through transmission and field-ion microscopic techniques.

The uniaxial tensile test using cathodically precharged specimens was used extensively due mainly to its convenience and ease. These tests provide good baseline data but should be restricted to internal comparison, since the nature of stresses in this test are ill-defined and many of the test parameters are not fixed (i.e. strain rate). The higher strength level of this steel enabled the use of fracture mechanics type testing in order to simulate the more "realistic" configuration described earlier in this chapter. These experiments used "double cantilever beam" type specimens which were also cathodically precharged with hydrogen. This was done in order to establish a situation where large scale diffusion of hydrogen to the crack tip region would be necessary for cracking. Tests using external hydrogen sources (gaseous or aqueous) have shown that surface entry conditions may control (or limit) cracking and additionally, the diffusion distances from the crack tip to crack reinitiation sites within the specimen may be quite small, preventing unambiguous interpretation of cracking event frequency.

It is hoped, that careful comparison of each of these various tests will shed additional light on the role of microstructural traps on hydrogen induced cracking and embrittlement.

Chapter 4
Experimental Procedure

4.1. Material

Two separate experimental alloys were chosen for this study, although the bulk of the work was performed on one. This alloy, with heat designation V113, was prepared by U.S. Steel Research as a 45 kg ingot, (76 x 200 x 356 mm), reheated to 1260°C and rolled directly to a 25 mm thickness. The finishing temperature was approximately 1110°C and the plate was subsequently air cooled. The other material, designated 704K017 was prepared by Bethlehem Steel Research as a 136 kg vacuum-melted ingot, reheated to 1230°C and rolled directly to 38 mm plate. The composition of these alloys are listed in Table 4-1.

In the course of this work, V113 was reanalyzed in order to determine the homogeneity of the plate, motivated by observed property variations. A comparison of two separate samples from this heat is shown in Table 4-2.

4.1.1. Heat Treatment

The heat treatment schedule chosen for these alloys was aimed primarily at first dissolving a maximum quantity of Ti and C into solution and second to precipitate out the TiC phase in a controlled fashion, to produce a continuous spectrum of sizes, morphologies, and interfacial coherencies. Irvine, Pickering, and Gladman[9] in an investigation of fine-grained C-Mn steels have determined that the solubility product of the TiC phase in γ iron is given by:

$$\log_{10}[Ti][C] = \frac{-7000}{T} + 2.75 \quad (T \text{ in K}) \tag{4.1}$$

	C	Mn	P	S	Si	Al	V	Ti	N
Heat V113	0.053	1.40	0.004	0.006	0.239	0.003	<0.002	0.225	0.001
Heat 704K017	0.098	1.07	<0.002	0.005	<0.01.	0.010	<0.002	0.430	-

Table 4-1: Compositions of Alloys. Values are given in weight %.

	C	Mn	P	S	Si	Ti	Sb	N
#1	0.050	1.43	0.005	0.028	0.31	0.22	0.002	0.0005
#2	0.049	1.42	0.005	0.009	0.32	0.22	0.002	0.005

Table 4-2: Duplicate Chemistry Analyses of heat V113

This predicts that 0.2% Ti and 0.05%C may be dissolved at 1200°C. Accordingly, all specimens of heat V113 as well as 704K017 were solutionized/austenitized at 1200°C for 1 hr in a flowing argon atmosphere. The specimens were subsequently water quenched. Aging of the specimens was performed in either molten salt or lead with the former predominantly used for temperatures ≤600°C. The aging temperatures ranged from 400°C to 900°C and all specimens were subsequently water quenched from the aging medium. All tensile and fracture mechanics specimens were machined from the fully heat treated condition in order to ensure through thickness microstructural homogeneity as well as to facilitate machining.

4.2. Microstructural Characterization

In the course of this study, various characterization techniques were employed as necessary to sufficiently explain bulk alloy behavior, both with and without internal hydrogen. Light microscopy, scanning and transmission electron microscopy, field-ion microscopy with associated atom probe capabilities and high resolution scanning Auger electron spectroscopy were all used to varying extents in the analysis of the materials.

4.2.1. Microscopic Examination

Light microscopy was performed on an American Optical ULTRASTAR metallograph employing both conventional bright field as well as differential interference contrast imaging when etching relief effects were sought. Specimen preparation consisted of hot mounting the material in glass filled diallyl phthalate at 150°C for 6 minutes, followed by rough grinding to 600 grit ($\sim 20\,\mu$m) on emery paper followed by polishing with 1, 0.3 and $0.05\,\mu$m Al_2O_3. 2% Nital (HNO_3 plus ethanol) was used predominantly, although an etch consisting of 100 ml H_2O saturated with picric acid and an addition of three-five drops HCl and one ml "TEEPOL" (wetting agent) was used for improve delineation of the prior γ structure.

Transmission electron microscopy (TEM) of this alloy was performed on JEOL 100C and 120CX instruments using a 100kV electron source. Specimens were prepared by first

diamond wafering 0.13-0.18 mm sections from bulk specimens, which were then either mechanically thinned on 600 grit paper or chemically thinned in a 92% H_2O_2:8% HF solution to a thickness of 0.10-0.13 mm. At this point, 3 mm diameter discs were cut and these were further mechanically thinned to between 0.025-0.05 mm. Final preparation was carried out with a FISCHIONE Twin-Jet electropolisher until a perforation on the order of 100-400μm was made. The electrolyte employed was 70% methanol-30% nitric acid at a temperature of -60 to -50°C. The operating potential was 10V and the optimum specimen current was between 10-20 mA. Upon perforation, the specimen was thoroughly rinsed in methanol and stored in ethanol prior to examination, in order to minimize surface oxidation. Alternatively, an electrolyte[113] consisting of 1 part anhydrous sodium chromate to 5 parts glacial acetic acid at room temperature and 20-25V was employed, but it was found to give variable results due to the hygroscopic nature of the sodium chromate.

Fractography for this study was conducted on JSM-35 and CamScan Series IV scanning electron microscopes, both operating at 25kV. No special preparation of specimens was necessary except for examination of fracture mechanics specimen sections. Here the method of Park[114] was employed where the specimen is hot mounted in transparent lucite and sectioned normal to the fracture surface. The section making an obtuse angle between the fracture plane and the sectioned surface was then prepared metallographically as discussed earlier in this chapter. The lucite was then dissolved away using acetone in an ultrasonic vibrator. The corner of the specimen where the fracture surface meets the polished and etched surface is then viewed in a scanning electron microscope for a direct examination of how the fracture path scales and matches with the underlying microstructure.

In order to more precisely identify the point at which TiC precipitates first appear in the microstructure as a function of time and temperature, field-ion microscopic (FIM) techniques were employed using facilities at USS Basic Research, under the guidance of Dr. S. S. Brenner. Specimens aged at temperatures between 400°C and 600°C for

various times were prepared for FIM examination using the method of Brenner and Miller[115]. This entails the preparation of a specimen "needle" with a tip radius of 0.01 - 0.1 μm. The specimen blank is either a 0.5 mm diameter wire or a nearly square 0.5 x 0.5 mm cross-section specimen with a length of about 1 cm. A "neck" is formed in the specimen through electropolishing at room temperature in a thin layer of 25% perchloric acid in acetic acid floating on CCl_4. The operating voltage is 24VDC relative to an Au cathode. In the second stage, the necked region is slowly dissolved to produce the "needle" in a solution of 2% perchloric acid in 2-butoxyethanol. Voltages in the range of 15-20 VDC were used with Au as the cathode. The specimen is promptly mounted and inserted in a cryostage in the high vacuum chamber of the FIM and cooled to near 77K. The atomic structure of the tip is revealed by first field evaporating surface scale and oxide layers and then allowing for the field ionization of an imaging gas (Ne in this case) at the atom sites. Neon back pressures used for examination were in the 10^{-5} torr range. As the gas atoms ionize near atomic sites at the specimen surface, they are radially projected to the negatively charged imaging screen which in this case consisted of a channel plate image intensifier and a phosphor screen. The magnification of the image formed is proportional to the distance from the specimen tip to the channel plate divided by the radius of curvature of the specimen. This later parameter can be empirically deduced from the operating voltage (usually 5-20kV).

Analysis of specimens involves dynamic visual characterization as well as interpretation of time-of-flight mass spectrometer (TOF-MS) information. The magnification levels are typically one million times and more; microstructural features on the order of 10 Å are resolvable with an uncertainty of ± 2Å. Fine carbides, in this case TiC, were sized by the following procedure: During the field evaporation of the specimen, low index plane collapse can be identified; the most readily identified in Fe are {100} and {110} type planes. These planes collapse by the successive evaporation of edge atoms inward since these positions protrude most from the specimen surface. By counting the continual collapse of such planes, one has a means of determining the depth of

material analyzed. The TiC phase, which has been previously analyzed by Youle et al.[16], Pickering et al.[82], and Piller et al.[41], protrudes slightly from the surface owing to the different evaporation field for this phase and therefore images more brightly than the matrix. Using the above plane-counting technique one can thus determine the depth of material evaporated between the emergence and disappearance of a TiC particle. Positive identification of the particles was possible through the use of atom probe. Essentially, this employs a probe hole in the imaging system which can be positioned (by moving the specimen) over an area ~10 Å in diameter. A double channel plate single atom detector is positioned at the end of a flight tube and a high frequency (50 Hz) voltage pulse is superimposed on the static DC voltage of the specimen. As an atom evaporates (ionizes) from the surface, it passes through the probe hole and impinges on the detector. A vast quantity of this data is compiled using a high speed (5-10 ms) digital timer with an interfaced computer. The mass-to-charge ratio is easily computed thereby allowing chemical analysis of selected areas of the surface.

4.2.2. Scanning Auger Spectroscopy

Initial studies of this type were initially conducted at General Electric Corporate Research and Development with the assistance of Dr. C. Briant. Later studies were conducted on a PHI Multiprobe 600 Auger Electron Spectrometer at CMU. The experimental conditions for all experiments were essentially constant. Specimens for these tests were of the standard notched pin type geometry. The specific geometry used was determined by the particular instrument.

During the course of this study, it was found necessary to examine high angle (prior γ) grain boundaries for chemical composition revealed as intergranular facets. Fracture along these paths occurred at room temperature only in the presence of hydrogen so a technique was devised through which these facets could be produced in the high vacuum chamber of an Auger spectrometer.

Specimens were first degreased in acetone and chemically polished in 47% H_2O-47%

H_2O_2-6% HF at room temperature for 5-10 seconds. They were then cathodically charged (for anode material and solution, see section on charged tensile testing) at 50 mA/cm^2 current density for one hour, rinsed thoroughly in alcohol and immediately placed in the vacuum chamber. After a short time period ($\sim$ 15 min.) and attainment of a vacuum level of 1×10^{-9} torr, the specimen was fractured in the chamber at room temperature using a special fracture attachment. Analyses were conducted using 3 and 5kV electron beams from a LaB$_b$ source. Typical focused beam diameters of 1000Å were obtained.

Where concentration levels of species have been reported, a standard technique[164] was employed, where the atomic concentration of species x is given by:

$$C_x = \frac{I_x}{S_x d_x} \bigg/ \sum_\alpha \frac{I_a}{S_a d_a} \qquad (4.2)$$

where the I_α are the Auger peak heights for each element present, S_α is a sensitivity factor for the element α for the particular analysis conditions and d_α are scaling factors. For iron, the major element present, the peak at 703eV was chosen since it is least susceptible to distortion from magnetic effects.

4.3. Hydrogen Permeation Testing

The characterization of hydrogen trapping in these materials was performed by the use of an electrochemical permeation technique, first suggested by Devanathan and Stachurski[141]. The experimental set-up is shown in Figure 4-1. The experimental details have been extensively discussed by Pressouyre[28] and for further details, the reader is referred to that document. The anodic cell potential for all experiments was +200mV(SCE) and the cathodic current density was 1.0 mA/cm^2. In all other details, the experimental technique was identical to that of Pressouyre.

The specimen preparation was as follows. Material blanks approximately 6.5cm^2 were mechanically thinned to between 0.50-0.64mm and chemically thinned in 47% H_2O_2 - 47% H_2O - 6% HF to between 0.25-0.38mm. The specimen was then polished using 1μm Al$_2O_3$ and Pd plated on both sides using "Sel-Rex Palladex VI". Prior to plating,

C — Counter Electrode   W — Working Electrode
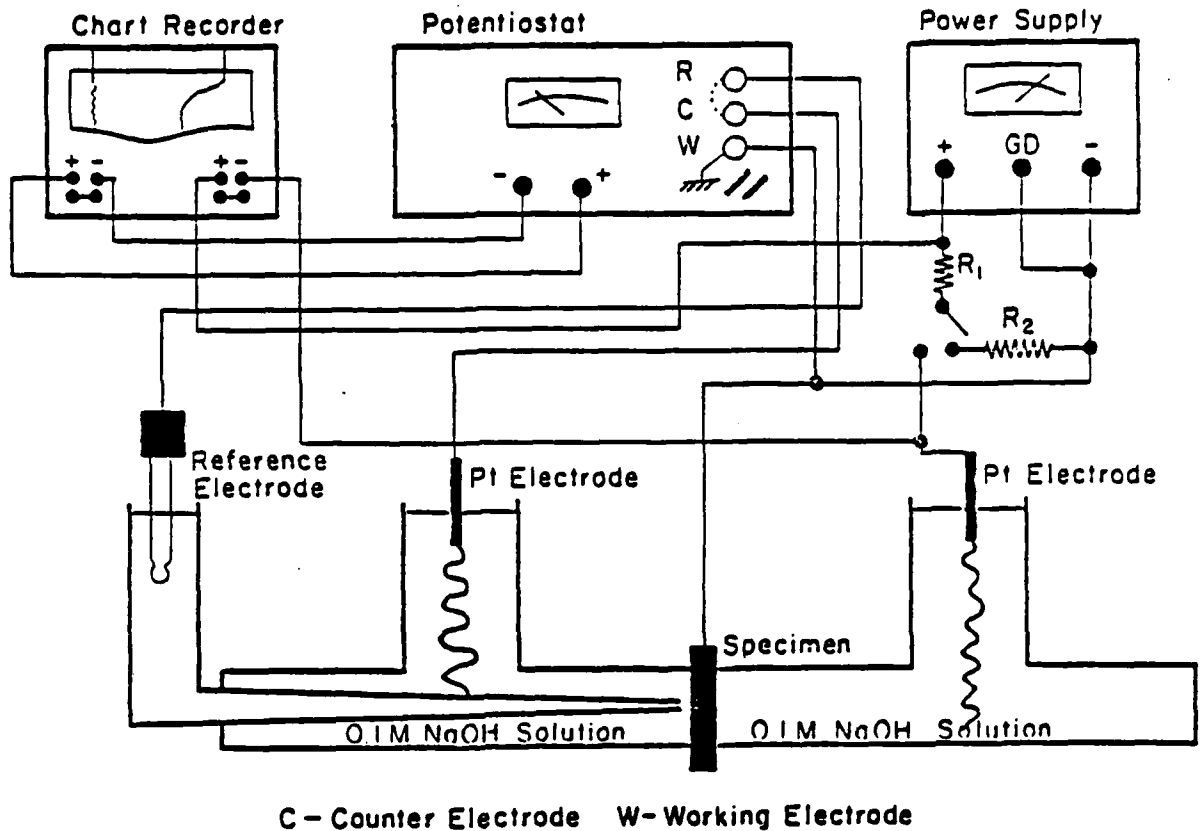
Figure 4-1:   Schematic apparatus arrangement for hydrogen
permeation   transient acquisition [28]

the specimen was momentarily dipped in 92% H_2O_2 - 8% HF for 2-3 sec and immediately

rinsed in methanol in order to remove the oxide film and to enhance the Pd plate

integrity.   The specimen was then immersed in the plating solution and a 500Å thick layer

was produced at a current density of 11 mA/cm^2.   The specimen was then rinsed in

distilled water.

As depicted in Figure 4-1, the specimen was then physically clamped between

virtually identical glass cells which comprised the anodic (left hand side) and cathodic

(right hand side) compartments for the permeation experiment.   In the cathodic cell, a

low density current is passed between the specimen and platinum anode through the use of

a constant current supply.   In a basic solution, as used here, this produces the reaction

$$2H_2O + 2e^- \rightarrow H_2 + 2OH^- \tag{4.3}$$

at the specimen surface, thus producing a hydrogen source. On the anodic side the specimen is attached as a working electrode to a potentiostat which maintains a constant potential (voltage) between the specimen and a reference electrode (saturated calomel) by inducing current as necessary through a counter (platinum) electrode and the specimen. The anodic cell potential, +200 mV(SCE), was chosen since the only reaction possible under the given conditions was the oxidation of hydrogen as it emerged through the opposite specimen face. This was made possible due to the palladium plating, which is noble in the alkaline NaOH solution chosen. The current through the counter and working electrodes may be accurately measured in the μA range, translating into a sensitivity to hydrogen flux on the order of 1 x 10^{-11} equiv. H/cm^2-sec.

The measured flux-time data may be readily analyzed in terms of normalized flux (J/J_{∞}) versus time and the geometry of this experimental configuration allows the use of single dimension solutions of Fick's second law using either a Laplace or Fourier transform. It should be noted that these solutions may yield the effective diffusivity of H through the microstructure, but contain no terms for the effect of trapping on hydrogen diffusion.

Alternatively, several analytical techniques may be employed which more directly yield the diffusivity through an analysis of the flux vs. time curve. The two most common techniques are the time-lag and breakthrough methods. The time-lag method uses the fact that the integrated quantity Q_t of diffusing species to pass through a membrane in time t is given by[118]

$$Q_t = \frac{DC_o}{L}\left[t - \frac{L^2}{6D}\right] \tag{4.4}$$

where C_o is the fixed input concentration, D is the apparent diffusivity and L is the specimen thickness. The intercept on the time axis of the Q_t vs t functionality is defined as

$$t_{lag} = \frac{L^2}{6D} \tag{4.5}$$

It can be shown that this t_{lag} corresponds to a value of J/J_{∞} equal to 0.63 and therefore the diffusivity is readily obtained if the specimen thickness is known.

Additionally, the breakthrough time may be used to calculate the apparent diffusivity. This time is defined as the first time at which measurable hydrogen is detected from the output side of the membrane and is defined by

$$t_b = \frac{L^2}{15.3D} \tag{4.6}$$

As mentioned by Pressouyre[28], this method is sensitive to slow surface reactions.

As stated above, these diffusivity values are obtained without any assumption related to the effect of trapping. McNabb and Foster have analytically attempted to model the effect of trapping on transient hydrogen flux by modifying Fick's second law to include a trapping "reaction". This model is described in detail later in this document, but it may be noted here that the solution to the McNabb and Foster "modified" equations include a number of parameters which specify the capture and release rate of hydrogen at traps, relative coverage and trap density. Due to the number of adaptable parameters, simple curve fitting of experimental data may not yield a unique set of values, as discussed by Pressouyre, so independent characterization of certain variables is necessary. Despite this difficulty, research by Pressouyre[28] and Iino[36] has revealed that a good deal of qualitative information pertaining to trap character may be obtained by alternate means. These are briefly introduced here and discussed in greater detail throughout this document.

First, Pressouyre deduced that successive polarization transients through a material may help to distinguish different trapping populations by the following reasoning. During the first or initial passage of hydrogen through an iron or steel membrane, the hydrogen flux will be influenced to some degree by all traps present and the associated flux data will reflect the influence of the entire trap population. However, Pressouyre noted that, while most traps were considered "reversible" in nature and comprised finite capture and release parameters for hydrogen, certain highly energetic traps might be classified as

"irreversible" in nature and would thus display a finite capture rate and a very small (or zero) release rate. Hence, if the hydrogen source were removed upon reaching steady state after an initial transient, the reversible traps would be expected to gradually give up their hydrogen during decay but the irreversible traps would not. If such an irreversible trap density were present, this would be manifested in subsequent transients as a more rapid breakthrough time and more rapid transient rise to steady state. This, in fact is observed for certain types of traps, most notably, titanium carbide. If only one reversible and one irreversible trap population are present in a microstructure, then the reversible trapping effects will be isolated in the second (and successive) transient(s) and the contribution of irreversible trapping may be inferred by difference between the first and second transients.

Iino has looked more closely at the possible implications on the observed form of hydrogen flux resulting from variation of the trapping parameters defined by the McNabb and Foster formalism. By substitution of various parameters in his solutions for the diffusion equations, he hypothesized that the flux-time curves may display higher capture than release rates and even irreversible traps for conditions of low coverage. Although this description is by no means complete, it serves to illustrate that additional information about the character of trapping may be obtainable even in microstructures too complex for isolated evaluation of trapping parameters.

4.4. Tensile Testing

Mechanical characterization of this material was conducted using standard uniaxial tensile testing technique. This practice is common for the hydrogen embrittlement susceptibility testing of alloy classes which display little or no sustained load or deflection degradation, as is the case with many low to medium strength steels[44].

The specimen geometry used is shown in Figure 4-2. All specimens were polished following machining to a 600 grit finish on a horizontal drill press. Testing was performed on an Instron Model 1125 Universal Testing Instrument using a 10,000 kgf load cell and a fixed cross-head speed of 0.5 mm/min.
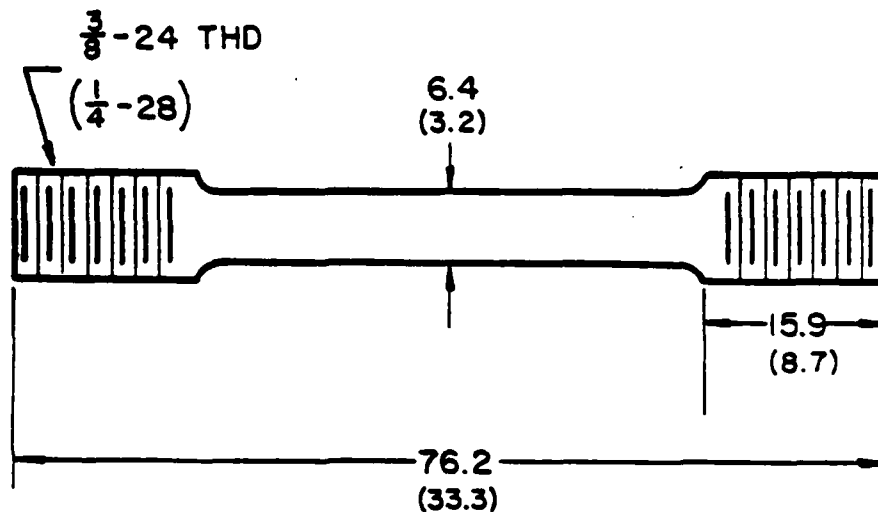
Figure 4-2: Dimensions of cylindrical tensile specimens. All dimensions are in millimeters except thread sizes. Values in brackets are for sub-sized transverse specimens.

For tests conducted to evaluate embrittlement susceptibility, the threaded ends of tensile specimens were first coated with a "stop-off" lacquer and then chemically polished for 10 seconds in a 47%H_2O - 47%H_2O_2 - 6%HF solution and immediately immersed in the cathodic charging solution. This latter solution consisted of 1 $\underline{N}$ H_2SO_4 (approx. 26 ml conc. H_2SO_4 per liter) with 10 drops each of CS_2 and a solution consisting of 10 mg As_2O_3 per cm^3 of water. This latter solution was prepared using the method of Pressouyre where 20 mg/cc of As_2O_3 are dissolved in 1 $\underline{N}$ N_2OH followed by H_2SO_4 neutralization. These compounds are added, in order to inhibit recombination of adsorbed hydrogen

$$H_{ads} + H_{ads} \rightarrow H_{2(g)} \qquad (4.7)$$
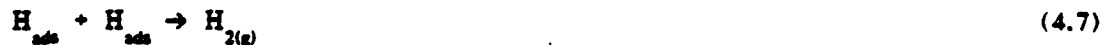
A platinum wire anode was employed and a current density of 20 $\mu A/cm^2$ at room temperature was used throughout. The current density was chosen with the intent of producing reversible, microstructurally dependent embrittlement in the system. Reversibility was ensured by charging and plating (discussed below) a specimen in the normal fashion. The Cd plating was then removed by mechanical polishing and the specimen baked 3 hrs

at 150°C. Following this, the specimen was tested in tension and the results compared to uncharged specimens. In all cases, for a charging current density of 20 $\mu A/cm^2$ the original (hydrogen-free) ϵ_f (failure strain)and %RA were obtained from the charged and out-gassed specimen.

Charging times were determined through the use of a

$$x \sim 2 \ (Dt)^{1/2} \tag{4.8}$$

diffusion distance dependency. Using an estimated diffusivity of H in Fe at room temperature of 5×10^{-6} cm^2/sec, this requires a time of 5 hrs. for charging of a 6.4 mm diameter tensile specimen. Cathodic charging times for other size specimens in this study were similarly determined to ensure geometric scaling.

Following cathodic charging, the specimens were rinsed in distilled water and immediately Cd plated in order to impede hydrogen egress from the specimen. This barrier property is due to the low diffusivity, $\leq 10^{-10}/cm^2/sec$[121], of hydrogen in Cd[121]. The plating procedure was the same as used by Pressouyre[28] and consisted of a solution containing 32g/l CdO, 112 g/l NaCN, 12 g/l NaOH and 4.5 g/l of a brightening agent ("Postum", a coffee beverage substitute) dissolved in distilled water. Maintenance of the brightener was important since, as shown by Berman[122], "bright" coatings are better barriers to hydrogen than "dull" ones and less hydrogen uptake during plating occurs in the presence of a "brightening" agent. The anode in this case was a Cd strip and the plating was performed at room temperature for 30 min at a current density of 2.15 x 10^{-2} A/cm^2; measured plate thicknesses varied from 20-40 μm.

Embrittlement · in these tests was determined through %RA changes between the charged and uncharged conditions. The %RA was measured with an optical measuring microscope with a resolution of 0.01 mm. Four traces were measured across the specimen surface, each taken 45° from the previous one. These final diameters were compared to the original diameter d_o and the %RA given by:

$$\%RA = \frac{d_o^{\,2} - d_f^{\,2}}{d_o^{\,2}} \qquad (4.9)$$

All 25 mm gage length specimens in this study were taken from the 25 mm thick plate in the longitudinal direction. Additionally, undersized tensile specimens, as shown in Fig. 4-2, were taken in the transverse direction. The cross-head speed for these tests was also 0.5 mm/min. In these experiments, the charging current density was still $20\,\mu A/cm^2$, but for only a 75 min period. Cd plating was conducted as described above.

4.5. Hydrogen Induced Cracking (HIC) tests

Since a major goal was to determine the effect of microstructure on hydrogen assisted crack growth in these materials, a fracture mechanics type specimen was chosen so that a quantitative relationship could be established between the driving force for crack growth (K_I) and the crack growth rate (da/dt). This is in contrast to smooth specimen type tests where combined initiation and propagation information are desired[ref(1111)]. Although the initiation site is predisposed in a fracture mechanics type test (i.e a fatigue induced pre-crack), a wealth of information about the interaction of the environment (aqueous, H_2 or internal H) and a growing crack is available from this type of test. It was decided to test and analyze only cathodically pre-charged specimens in a manner similar to the tensile specimens since for this procedure interpretation of the kinetics would not be confused by rate controlling surface reactions.

The specimen type chosen for these experiments was a crackline-loaded, single-edge-cracked specimen (also known as a double cantilever beam) as shown in Fig. 4-3. All specimens were taken from the plate in a T-L orientation. This specimen type was chosen since it was material conservative; it can be used in either an increasing or decreasing K situation and it can be tested repeatedly for threshold determinations.

The overall specimen configuration was chosen for convenience except for the following factors. In K_{Ic} testing it is known[123] that the specimen thickness does affect the measured K value through an effect on the state of stress ahead of the crack tip.
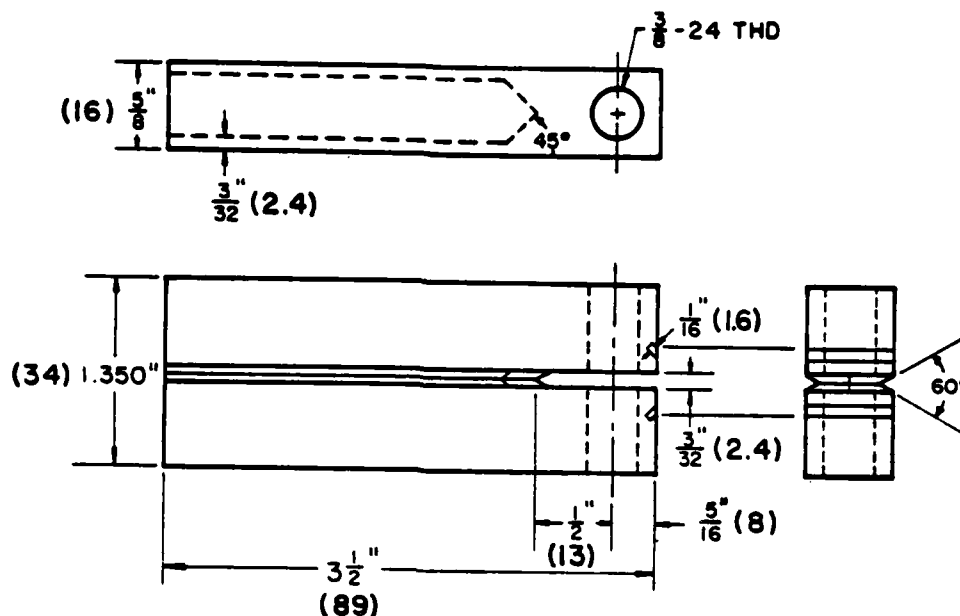
Figure 4-3: Dimension of DCB specimens used in this study. Values in brackets are in millimeters.

The recommended thickness for these tests according to the ASTM E399 plane strain fracture toughness test standard is

$$B \geq 2.5 \left(\frac{K_{IC}}{\sigma_{ys}} \right)^2 \qquad (4.10)$$

where σ_{ys} is the uniaxial yield stress and $K_{.Ic}$ is the valid toughness value. However, for "sub-critical" testing such as of the stress corrosion or hydrogen type, no standards have either been made or proposed. Brown[90] has noted in SCC tests of AISI 4340 in 3.5% NaCl that for specimens with a thickness value

$$B \geq 2.5 \left(\frac{K_{ISCC}}{\sigma_{ys}} \right)^2 \qquad (4.11)$$

a higher threshold value was observed. A possible interpretation of this may be that crack growth data at K levels obeying the inequality

$$K > \frac{\sigma_{ys} B^{1/2}}{1.58} \qquad (4.12)$$

should be interpreted in a cautious manner. In the present work, the thickness chosen probably allowed testing to stress intensities between 50-70 MPa(m)$^{1/2}$ before the data are subject to thickness effect uncertainties by this criterion.

In an attempt to restrict cracking to a single plane normal to the load application direction, side grooves were also machined in the specimens. It has been found that the presence of these grooves does suppress shear lip formation and crack front bowing and may guide the crack along a single plane. Steel specimens are more susceptable to ths phenomenon than wrought Al alloys due to a strong texture dependent susceptibility for the latter.[90] It is found that materials which exhibit a region of crack growth which is independent of stress intensity may branch in this region since a side branch would not experience a crack growth rate penalty as would a side branch in the Stage I regime. Freed and Krafft[125] have analyzed the effect of a side-grooved geometry on the Mode I stress intensity and showed that it is modified as:

$$K_{Ia} = \left(\frac{B}{B_n}\right)^{\Phi} K_{Iu} \qquad (4.13)$$

where K_{Iu} is the stress intensity factor for the unotched geometry and B_n is the reduced thickness at the notch. For a variety of materials $1/2 < \Phi < 1$; a value of $\Phi = 1/2$ corresponds to a high value of toughness in the groove blank direction relative to the forward crack direction and as Φ approaches unity, this relative value diminishes. For the given specimen geometry, Φ was chosen as 1/2 based an the empirical observation that crack extension initiated in the forward crack direction for these tests. This condition was further promoted through the use of a chevron notch which provides a straightened fatigue pre-crack. The stress intensity for this configuration as well as any Mode I crack[161], is given by for the case of plane strain by:

$$K_I^2 = \frac{P^2 E}{2B(1-\nu^2)} \frac{dC}{da} \qquad (4.14)$$

where P is the applied load, E is Young's modulus, B is thickness, C is the

compliance, a is the crack length measured from the load application line and v is Poisson's ratio. The compliance is defined as the reciprocal of the load line deflection, δ, to the applied load. In effect then, the stress intensity of any specimen is known if the relationship dC/da can be determined. This can be done empirically or can be derived from theoretical considerations. As is often found for specimens of this type[22], the compliance obeys a logarithmic dependence on crack length of the form:

$$C = \delta/P = Aa^n \qquad (4.15)$$

where A and n are determined empirically. This relationship was established experimentally for this material and specimen geometry as shown in Fig.4-4. Incorporating all these factors, the final expression for the plain-strain stress intensity is then

$$K_I = \left[\frac{n \ AE \ P^2}{2 \ B_n(1-v^2)} \left(\frac{\delta}{AP} \right)^{(n-1)/n} \right]^{1/2} \qquad (4.16)$$

Using the following material constants

n = 2.07

A = 5.69 x 10^{-4} kg^{-1}-$m^{-1.07}$

E = 211.4 GPa

v = 0.293

a simplified expression for the stress intensity is given by:

$$K_I = 0.441 \ \delta^{0.2584} \ P^{0.742} \quad \text{in} \quad MPa(m)^{1/2} \qquad (4.17)$$

Therefore, the instantaneous stress intensity can be calculated if the load line deflection, δ, and P are known. Since these two parameters can be recorded continuously with time, as will be discussed below, these experiments can be automated over long time periods.

Prior to the cathodic introduction of hydrogen, all test specimens were fatigue pre-cracked through the entire chevron notch and into the constant thickness portion of the
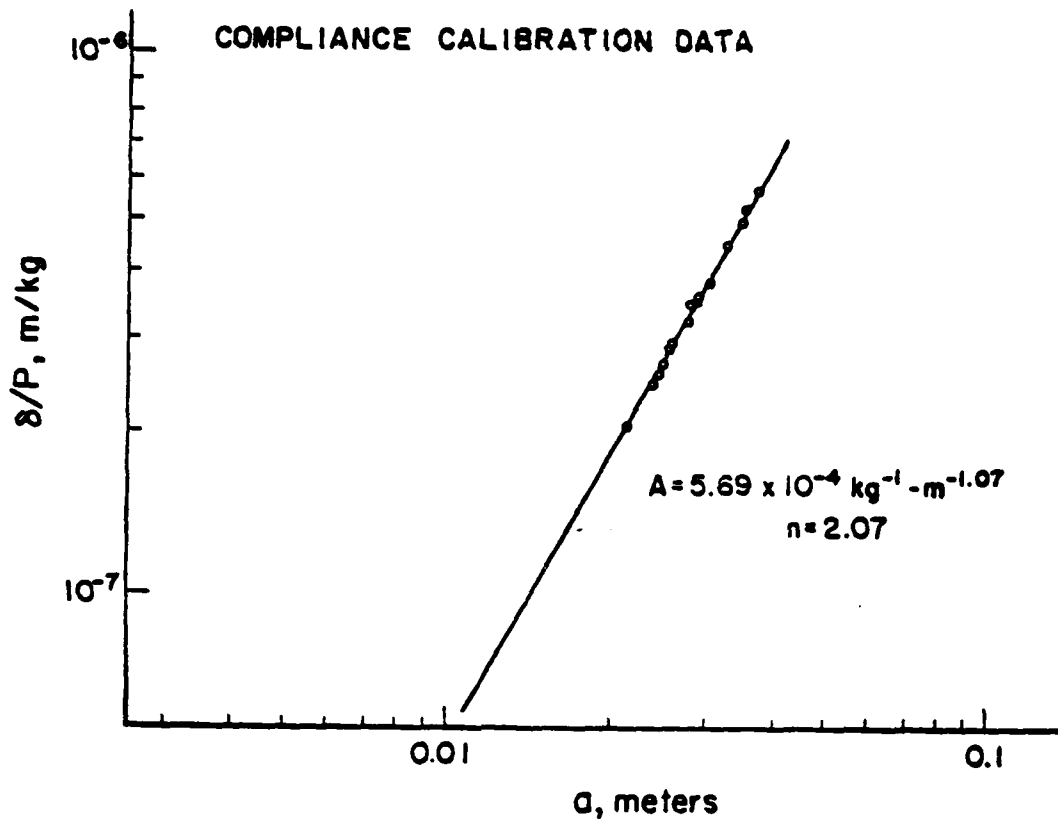
Figure 4-4: Experimentally measured compliance values for DCB specimen and power law constants

specimen a distance of not less than 2 mm. In most cases, a fatigue pre-crack could be produced at alternating stress intensities of $\Delta K = 14$-20 MPa(m)$^{1/2}$ at R values of 0.2 and frequencies of 20 Hz. Under certain circumstances, where the crack propagation rate was particularly slow, the use of a $0.1\underline{N}$ H_2SO_4 solution applied by eyedropper to the notch root was helpful in reducing the time for crack extension. Following fatigue pre-cracking, specimens were ground to a 600 grit finish over the entire surface, chemically polished for 10 sec. in 47% H_2O_2 - 47% H_2O - 69% HF and pre-charged over the entire surface in a manner identical to that chosen for the tensile specimen except for time. The charging time was chosen in order to give a depth of penetration similar to that of the tensile condition from the equality:

$$\left[\frac{x_1}{x_2}\right]^2 = \frac{t_1}{t_2} \tag{4.18}$$

Using the condition for the tensile test (x_1 = 6.4 mm and t_1 = 18,000 sec) and the reduced thickness as 11 mm gives a charging period of 15 hrs. An extended time of 24 hrs was chosen in order to ensure complete saturation.

Following charging, specimens were "baked" at $150°C$ in order to homogenize the hydrogen, after the technique of Gerberich and Chen[127]. The baking time was chosen with the assumption that hydrogen must be redistributed from near surface regions to the center. Using available diffusion data for hydrogen in α-Fe[120], D was estimated at 5 x 10^{-5} cm^2/sec and the necessary diffusion distance was chosen as 5 mm. Using an x~ $(Dt)^{1/2}$ relation, this then requires a 1-1/2 hr baking time.

Specimens were tested immediately following the baking procedure after they had been allowed to cool to room temperature. Testing was performed on an MTS servohydraulic feedback controlled testing machine with a 100kN capacity. This machine has the capability of being operated in either a transducer (clip-gage) displacement or load control mode. Clip gage and load cell signals were recorded continuously from their respective D.C. conditioners on a dual pen strip chart recorder in order to trace crack growth over time. The clip gage used could measure 1.0 mm of crack mouth opening with an error of 0.01%. Similarly, the load cell system was capable of a 4500 kg range with only a 0.5 kg error.

Initially, tests were run in a clip-gage (displacement)controlled mode in order to effect a decreasing K type test. The stress intensity was ramped to 50 MPa(m)½ and held 24 hrs. If no crack growth was detected during this period, the load was increased in 200 N steps until crack growth was detected in a 10 hr period. Threshold determinations were repeated at least one additional time in order to ensure repeatability. At the completion of the last threshold test, the specimen was unloaded and machine control transferred to the load cell signal. This produced a constant load (increasing K) type test which culminated in specimen failure.

Crack growth rates were determined from these data traces through the following

procedure. Crack length can be determined implicitly in terms of the measured parameters by rearranging the compliance expression:

$$a = \delta^{1/n} \, P^{-1/n} \, A^{-1/n} \tag{4.19}$$

Since either δ or P is constant with time for the testing configurations used, this expression may be differentiated with respect to time to give:

$$\left.\frac{da}{dt}\right)_{\delta} = -\frac{1}{n}\delta^{1/n}P^{-(n+1)/n}A^{-1/n} \left.\frac{dP}{dt}\right)_{\delta} \tag{4.20}$$

This equation gives crack growth for a fixed displacement condition. The corresponding expression for fixed load is

$$\left.\frac{da}{dt}\right)_{P} = \frac{1}{n} \, \delta^{1-n/n} \, P^{-1/n} \, A^{-1/n} \left.\frac{d\delta}{dt}\right)_{P} \tag{4.21}$$

Although the exact time differentials of δ and P in the above expression could not be evaluated from the chart traces, graphically evaluated slopes were measured over time periods which allowed a linear approximation.

Following fast fracture, specimens were prepared for SEM examination by rinsing in acetone followed by sectioning the specimens normal to the crack plane in order to accommodate them on the specimen stage of the microscope.

Chapter 5
Results

5.1. Microstructures and Properties

5.1.1. Heat Treatment

The heat treatments employed in this study were aimed at producing a controllable variation in TiC precipitate density which would ultimately effect a change in total hydrogen trapping capability. An additional requirement was that the trapping population should not strongly alter the strength level or adversely affect the toughness so that the hydrogen trapping capability in this case could be isolated and analyzed independently. In summary, the resultant microstructures following heat treatment were as follows:

1. Quenching from $1200\,^{\circ}C$ into water produced a highly deformed acicular ferrite microstructure with isolated islands of martensite.

2. Although precipitation of fine TiC phase was suppressed during the quench, some auto-tempering did occur resulting in some fine precipitation of cementite (Fe_3C).

3. Coarse Ti rich inclusions were found but did not influence tensile ductility greatly in the absence of hydrogen.

4. Aging at $400\,^{\circ}C$ resulted in grain boundary cementite. No evidence for TiC formation was found for short (<3hr) aging times.

5. Concurrent precipitation of Fe_3C and clustering of TiC occurred at $500\,^{\circ}C$. Notable secondary hardening occurred at longer aging times (~ 10hr) indicating significant TiC formation.

6. At aging temperatures greater than $500\,^{\circ}C$, the formation of cementite was effectively by-passed by the direct precipitation of TiC. Some TiN precipitation was also found.

These findings are consistent with the general tempering properties of microalloyed martensite reviewed by Honeycombe[22] and Speich and Leslie[130].

The general features of the quenched microstructure are shown in Fig. 5-1 . The average ferrite lath width was approximtely $0.5 \mu m$. It is believed that this microstructure is produced by either a bainitic or massive transformation of austenite to ferrite. Here, as in commercial grades, the ferrite grains are highly irregular in shape and possess a high dislocation density, about 10^{10} cm^{-2}. Manganese aids in obtaining this structure by retarding higher temperature transformation to polygonal ferrite[3]. The rather high austenitization temperature ($1200^\circ C$) used in this case probably also aided in this way by coarsening the final austenite grain size, which ranged from 50 to 150 μm, as shown in Fig. 5-2.

An additional microstructural feature which was virtually constant throughout the heat was the presence of inclusions. When resolved by TEM, as shown in Fig. 5-3, these particles were normally found in the size range of from 0.3-0.5 μm in diameter. However, and perhaps more importantly, a high density of larger particles in the 10-20 μm size range were also detected on an optical scale. As expected in Ti bearing steels, the particles are quite regular in shape, reflecting the effect of Ti on inclusion chemistry and morphology[3,7]. Infrequently, more sharp edged particles were also detected, suggesting that these were TiN precipitates[7]. A selected area dark field (SADF) image of a fine TiN particle is shown in Fig. 5-4. Note the finer background precipitation in this image. This arises from the fact that TiC and TiN are isomorphous with respect to each other and share similar d spacings, thus crystallographically representing the same phase. STEM microanalysis of inclusions in this alloy revealed a varied chemistry, but Ti and S were the most common constituents, as shown in the energy dispersive X-ray spectrum in Fig. 5-5a. These particles may represent either τ-Ti_2S or "Y" $Ti_4C_2S_2$ phase, although both of these phases are hexagonal and a wide range of stoichiometries are possible. Lattice spacing information from selected area electron diffraction (Fig. 5-5 b and c) analysis supports these possible structures, as summarized in Table 5-1. More will be said with regard to analysis and composition of these particles in the discussion on cathodically charged tensile properties.
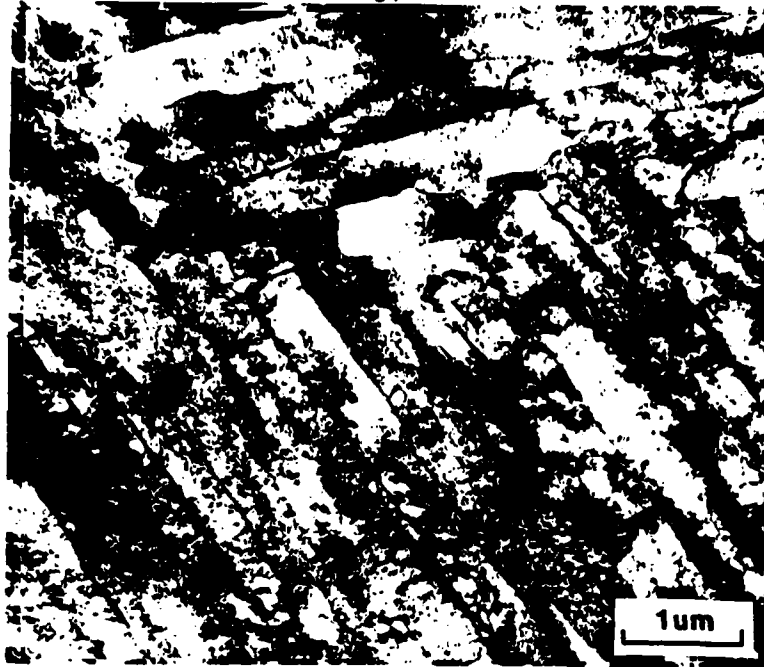
Figure 5-1: Transmission electron micrograph bright field image of as-quenched microstructure showing irregular grain shape and high dislocation density

Figure 5-2: Light micrograph of as-quenched structure showing outline of prior austenite grains

Figure 5-3: Transmission electron micrograph bright field image showing regular shaped inclusions
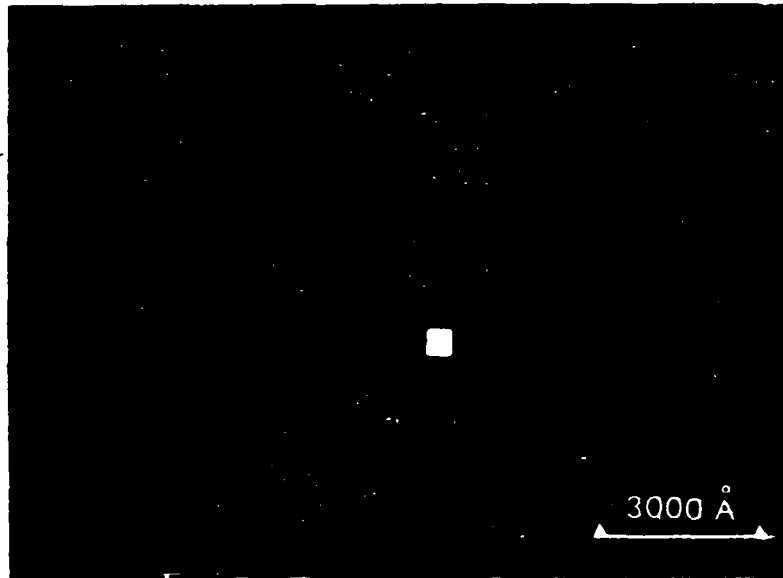
Figure 5-4: Centered dark field electron micrograph of cuboidal TiN particle.

a

b

.5μ

c)
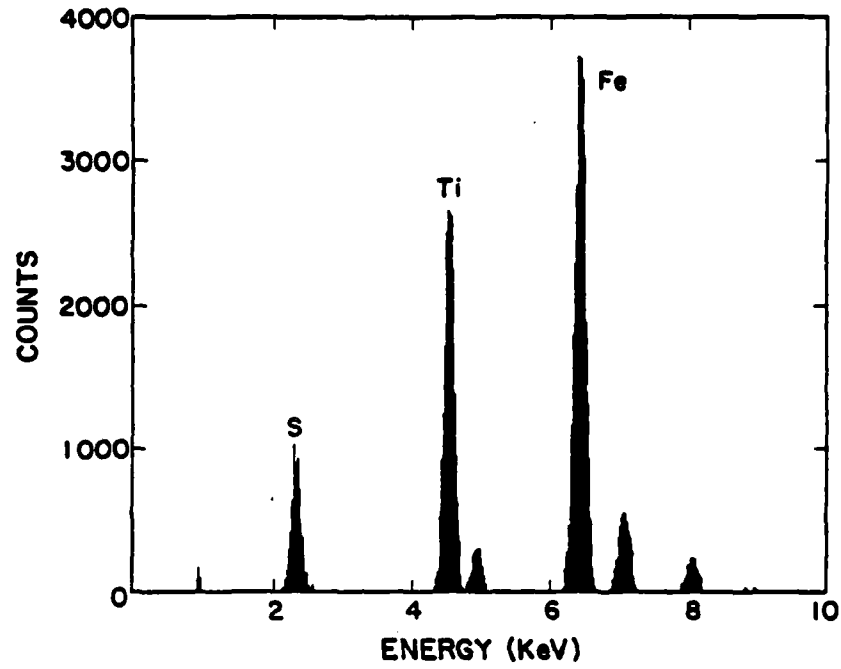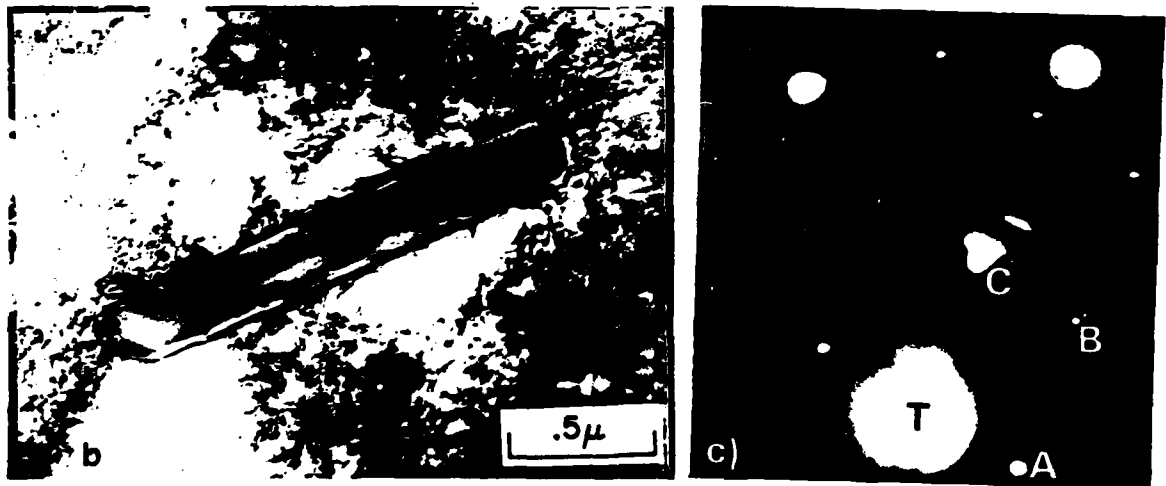
Figure 5-5: a) energy dispersive X-ray spectrum and b) associated inclusion particle showing bulk chemistry and c) selected area electron diffraction pattern[176].

Spot	Calculated "d" Spacing	Ti_2S "d" Spacing	$Ti_4C_2S_2$ "d" Spacing
A	2.79 Å	2.77 Å {100}	2.78 Å {004},{100}
B	1.77	1.74 {105}	1.74 {015}
C	2.02	1.96 {104}	1.98 {104}

Table 5-1: Comparison of calculated "d" spacings from Fig. 5-5c with powder diffraction "d" spacings for Ti_2S and $Ti_4C_2C_2$ phases

At the lowest aging temperature used in this study, 400°C, widespread precipitation of Fe_3C occurred along lath boundaries, as shown in Fig. 5-6a and b. It should be noted that the structure of these particles resembles a pearlitic type product. The appearance of this phase is a common feature of Stage 3 tempering during which cementite first appears in the microstructure[22]. This morphology is common to quenched and tempered plain carbon steels.

The cementite phase in this material was found to be consistent with the Bagaryatski orientation relationship with the ferrite, viz.

$$(100)_{Cementite} \parallel (0\bar{1}1)_{\alpha-Fe}$$
$$(010)_{Cementite} \parallel (1\bar{1}\bar{1})_{\alpha-Fe}$$
$$(001)_{Cementite} \parallel (211)_{\alpha-Fe}$$

This orientation relationship is supported by actual (Fig. 5-7a) and indexed (Fig. 5-7b) diffracton patterns. The diffracton pattern in Fig. 5-7 shows a $[\bar{1}01]$ α-Fe zone with a superimposed [100] orthorhombic Fe_3C pattern. Alignment of the $[001]$-Fe_3C directon with the $[\bar{1}21]$ α-Fe can also be seen from ths pattern.

Most importantly, it should be pointed out that the cementite phase was the only second phase detected in this microstructure. Detailed examination using both TEM and FIM techniques did not reveal any TiC clustering in microstructures aged for up to 1 hr. at 400°. This is reasonable since, if the activation energy for diffusion of Ti in α-Fe is assumed to be about 250 kJ/mol[138], the diffusivity at 400° will be on the order of 10^{-20} cm^2/sec. Using a $x^2 \sim Dt$ relationship, this allows for migration of Ti in one hour of $\sim$ 1Å. Since the nucleation of cementite will be limited by the diffusivity of C, which is much faster, it is understandable that that cementite formation is first observed.

At 500°C, which is prescribed by Honeycombe[22] as a transition temperature for direct precipitation of the alloy carbide, the carbide distribution and morphology is markedly different. At the TEM level, some limited cementite precipitation was found, as indicated in Fig. 5-8, but comparison with the cementite phase in Fig. 5-6 shows that

Figure 5-6: Bright field electron micrographs showing lath boundary precipitation of Fe_3C resulting from $400\,^{\circ}C/1\,hr$ aging
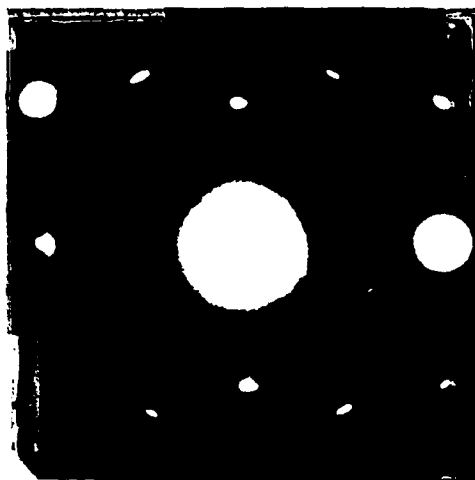
a
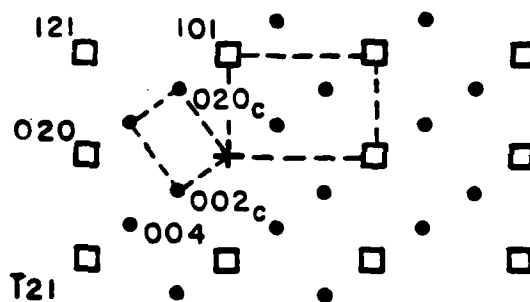
b

Figure 5-7: Cementite diffraction $(B=\{\bar{1}\,01\}_a)$ revealing Bagaryatski orientation relationship in a.) actual and b.) indexed SAD patterns

the morphology and size at 500°C is quite different. At the higher temperature, the carbide now exists as narrow platelets along the ferrite lath boundaries and which are generally isolated, in contrast to the larger clusters of cementite at 400°C which appear to nucleate at the boundary and grow into the ferrite matrix. Although the change in carbide morphology is slight, it probably indicates the beginnings of the influence of competing carbide phase (TiC) precipitation. This contention is supported by the isothermal aging response displayed in this temperature regime, as shown in Fig. 5-9.

5.1.2. Isothermal Aging Kinetics

Consider first the 400°C hardness trend for this material, shown in Figure 5-9. The pronounced softening is a general characteristic which is associated with the precipitaton of Fe_3C. Some small degree of secondary hardening is observed at longer times (> 10,000 sec) perhaps due to TiC clustering. Comparison of these trends to these of the 500°C curve reveals two noteworthy distinctions. First, the softening associated with the cementite precipitation is slightly delayed to longer · times · and secondly, a more dramatic secondary hardening appears at times > 10,000 sec. The most reasonable explanation for these observatons would be that competition for C between Fe_3C and TiC occurs which delays the softening associated with the cementite and diminishes the cluster sizes of this phase. At longer times, the fine TiC precipitates prevail producing significant hardening.

FIM analysis of the 1 hour/500°C microstructure revealed that extremely fine clusters of Ti and C (or N) were indeed present in the matrix, as seen in Fig. 5-10. The size distribution of these clusters in one of the specimens is summarized graphically in Figure 5-11, where it is seen that the average mean particle diameter ($\sim$10Å) was well below that discernible by conventional TEM analysis (realistically limited to $\sim$30Å). Significantly, these findings are in accord with predictions of Cuddy et al.[18], who observed a persistent "hot-hardness" increase in similar Fe-Ti-C alloys at 500°C, which was not attributed to conventional precipitation strengthening, since an overaging effect was not observed. Instead, the authors suggested that this dynamic strengthening was due to a
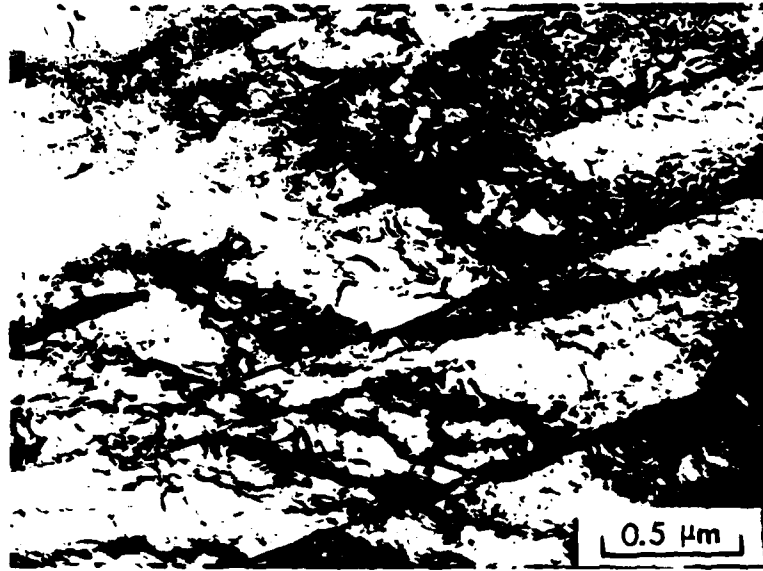
Figure 5-8: BF transmission electron micrograph showing thin interlath Fe_3C platelets resulting from $500°C/1hr$ aging. Compare with Figure 5-6
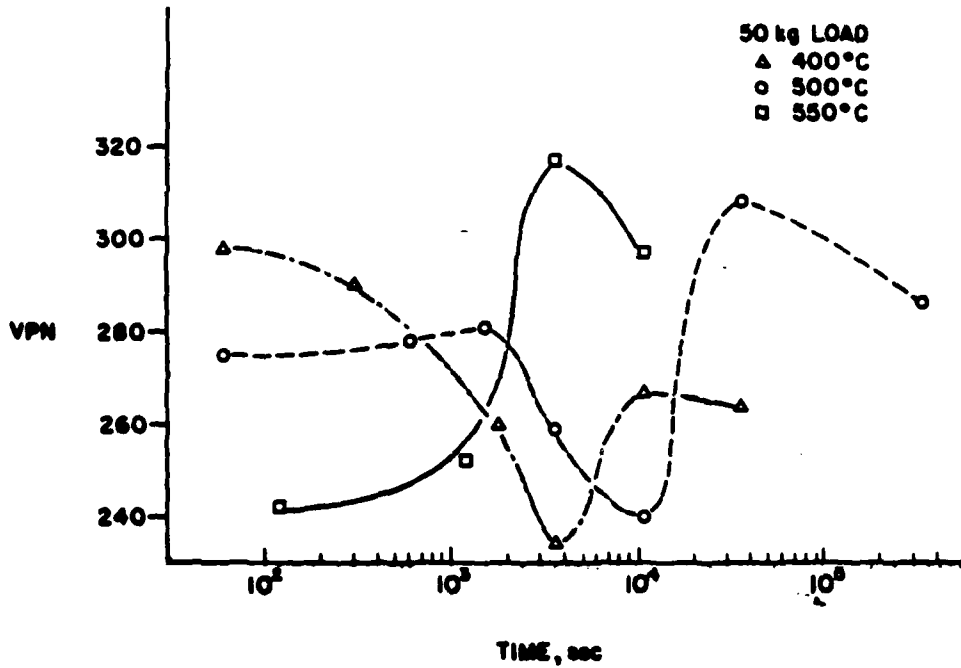
Figure 5-9: Isothermal aging response of Heat V113 at intermediate aging temperatures. All measurements made at room temperature

reorientation of some type of stable cluster of solute atoms under the stress field of a moving dislocation. This interaction was described as being analogous to Snoek ordering or reorientation of Zener dipoles. It is also likely that these "clusters" are the nuclei for the formation of the final TiC precipitate. This possibility is supported by the strong secondary hardening displayed at longer times at this temperature. The TiC precipitation for the $500\,^\circ$C/10hr treatment is shown in Figure 5-12 which is a field ion image. The particle size distribution from a field evaporation of this microstructure is shown in Fig. 5-13, suggesting a high rate of nucleation and more sluggish growth.
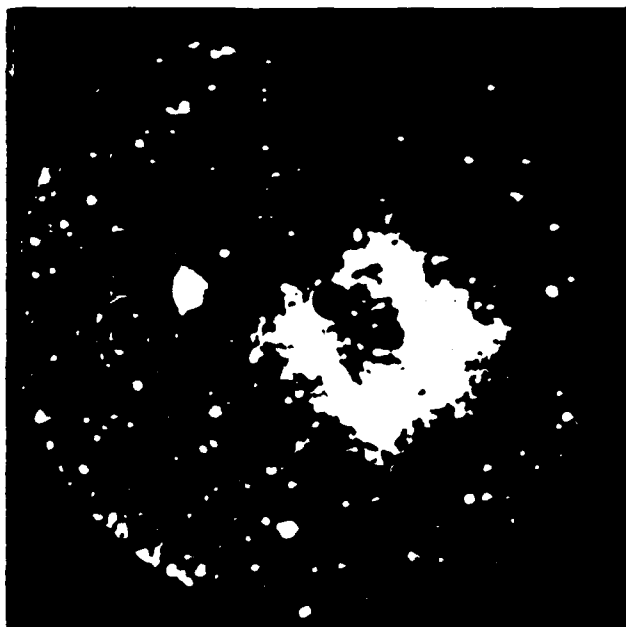
Figure 5-10: Field ion micrograph of small TiC clusters formed during aging at $500\,^\circ$C. Magnification is $\sim 10^6$ times

It may be concluded from these low temperature aging studies that little if any TiC clustering occurs at $400\,^\circ$ over the time periods studied and that precipitation is virtually limited to Fe_3C. At $500\,^\circ$, however, TiC clustering apparently affects the precipitation of Fe_3C throughout the aging process, as suggested by the delayed isothermal softening and strong secondary hardening observed at this temperature.

At aging temperatures of $550\,^\circ$C and above, direct precipitation of TiC occurs.
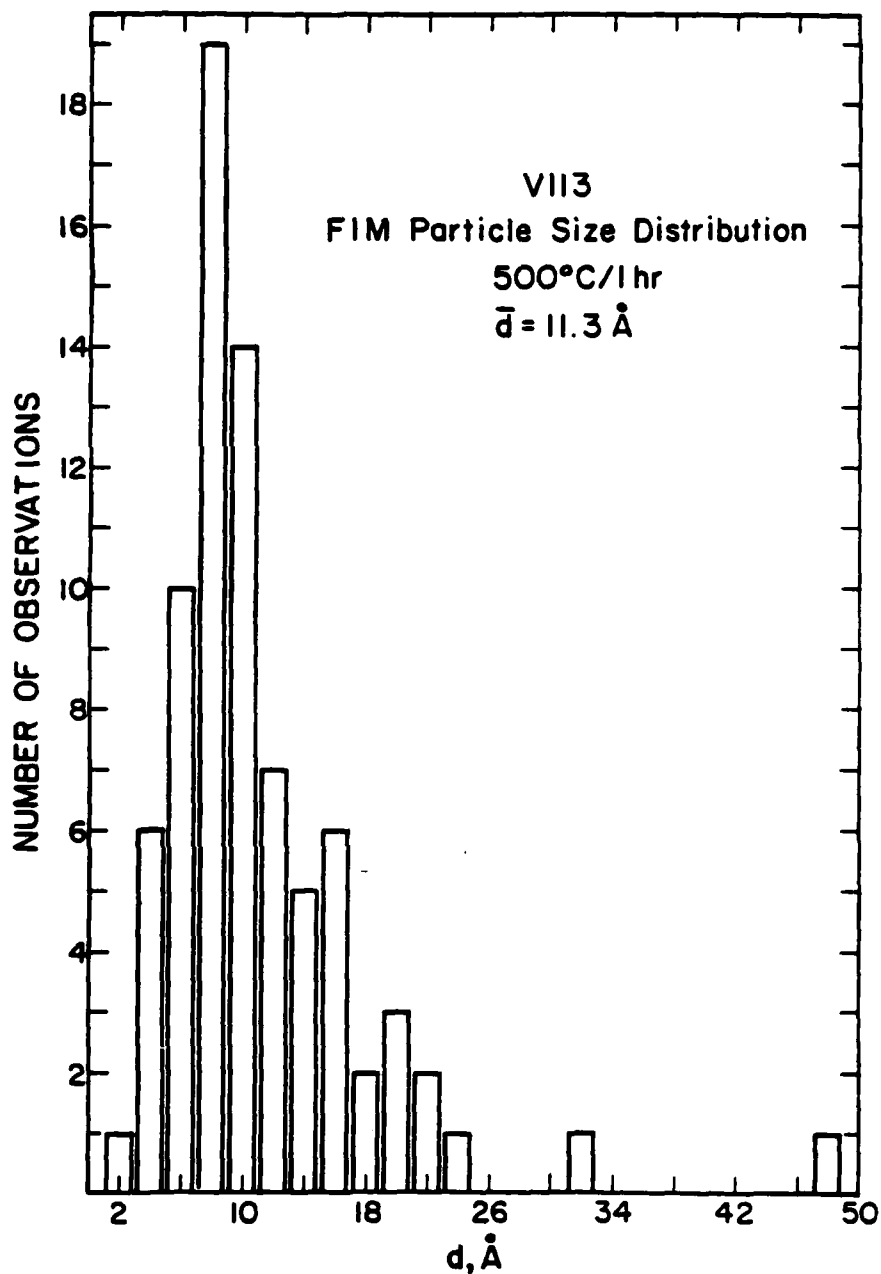
Figure 5-11: Sample size distribution of TiC precipitates in 500°C/1hr aged microstructure

This sequence change is supported first by the rapid secondary hardening displayed at 550°C in Fig. 5-9 and second by TEM imaging which shows dense precipitation of this phase at 600°C (Fig. 5-14) for one hour aging times. Additionally, no evidence for cementite formation was found through either TEM or FIM analysis. The micrographs in
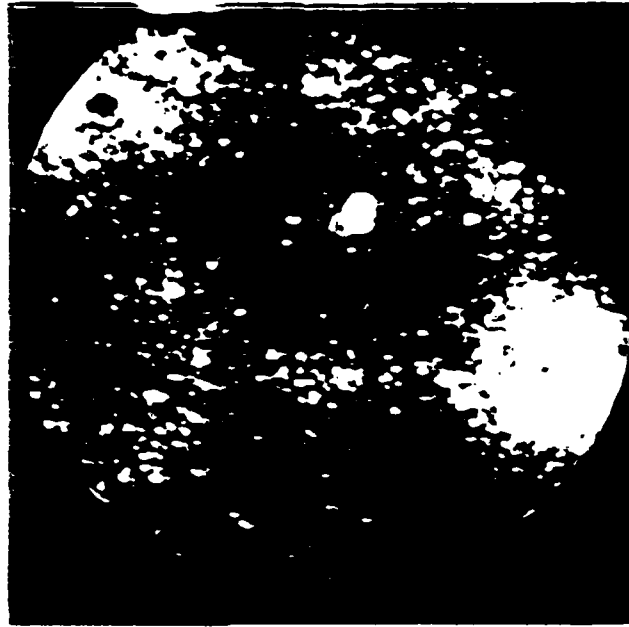
Figure 5-12: Field ion micrograph of TiC particle formed during aging at 500°C/10hr. Magnification is ~ 10^6 times

Fig. 5-14 show that heterogeneous precipitation of the TiC phase occurs primarily at lath and grain boundaries and also at dislocations. The identity of these precipitates as TiC phase is supported by comparison of the SAD pattern found for these microstructures (Fig. 5-14b) and the indexed version (Fig. 5-14c). Field ion analysis of these microstructures (Fig. 5-15) revealed a high density of very fine particles (d ~ 20Å) which were only barely discernible by TEM. Earlier studies of Piller et al.[41] have shown that Fe-Ti-C alloys doped with Sb displayed a markedly higher nucleation rate of TiC at 560°C than equivalent Sb free alloys. It is not known if the impurities present in this alloy (P and S) had the same effect, but the high nucleation and slow growth rates suggest such a possibility. It should additionally be noted that the 500°C and 550°C aging curves in Fig. 5-9 also indicate that the peak strengthening due to TiC precipitation is susceptible to rapid overaging. Although the particle size range does not significantly change over these time periods, the interfacial coherency with the matrix may be changing significantly, as suggested by Youle[16], suggesting that much of the strengthening may be due to transient dislocation-coherency strain interactions.
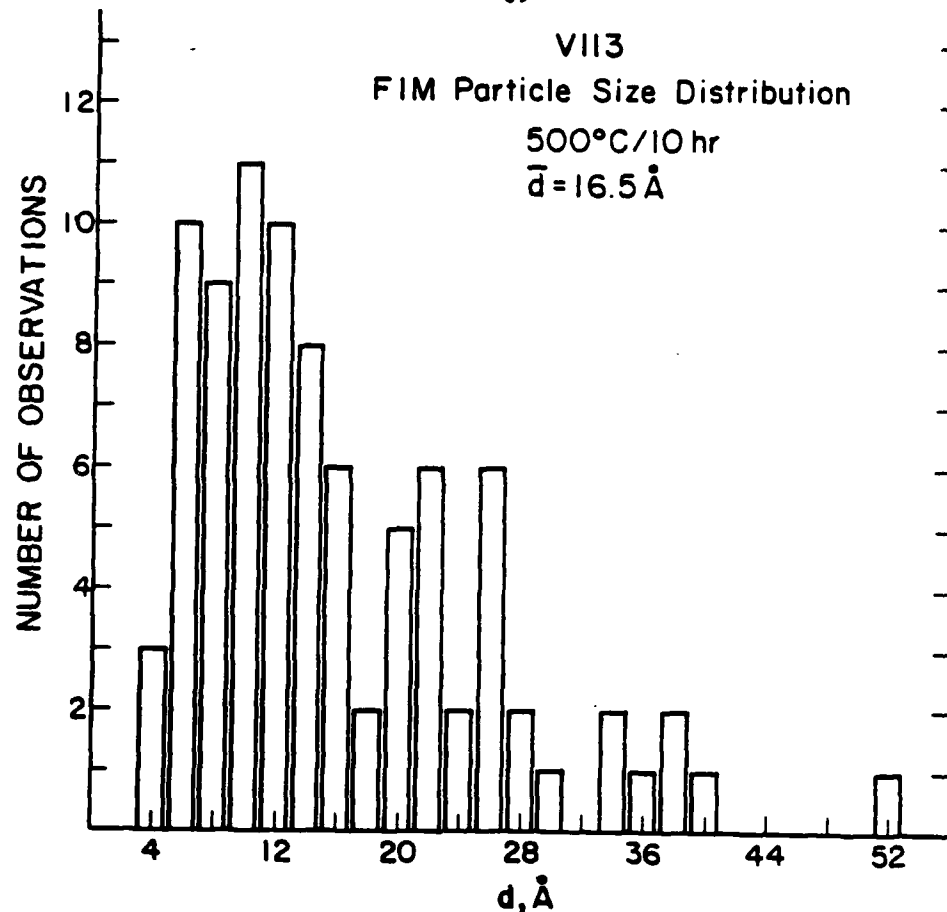
Figure 5-13: Sample size distribution of TiC precipitates after aging at $500\,^{\circ}C/10$hr. Note shift in average size and broadening of distribution from Fig. 5-11

The microstructure resulting from the $700\,^{\circ}C/1$hr treatment revealed a coarsened TiC precipitate population as well as a partially recrystallized microstructure, as illustrated in Fig 5-16a and 5-16b . This microstructure was accompanied by a significant loss in strength, as was also observed by Freeman[139] and Kuo[140]. At higher aging temperatures, both the coarsening of the TiC phase and recrystallization of the grain structure accelerated until for the $900\,^{\circ}C/1$hr condition the grain structure was completely recrystallized. Somewhat unexpectedly, there remained a fairly dense distribution of fine TiC particles, averaging about 100Å in size, which suggesting that growth continues to be sluggish. Fig 5-17a and 5-17b which are matching BF and DF pairs from the $900\,^{\circ}C/1$hr structure show the dense distribution of TiC precipitates which are now readily identified on the BF image. Note the somewhat larger particles along the lath boundary, suggesting earlier nucleation or more rapid growth at these sites.
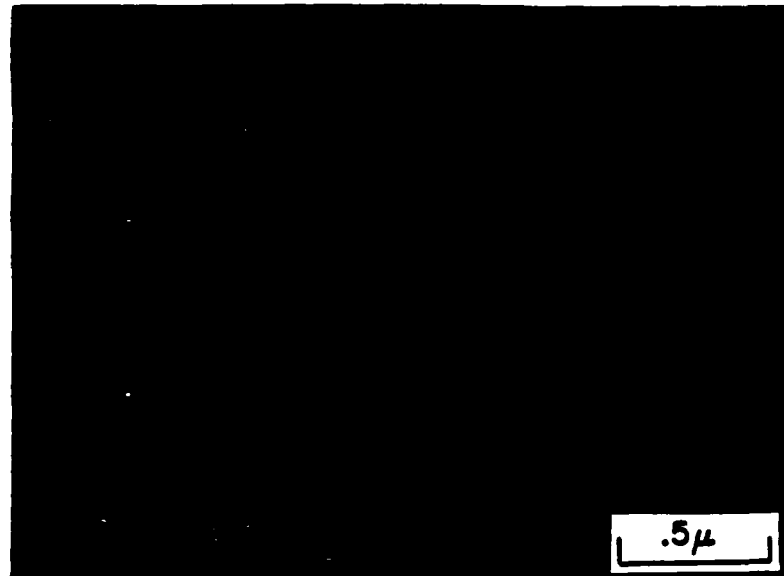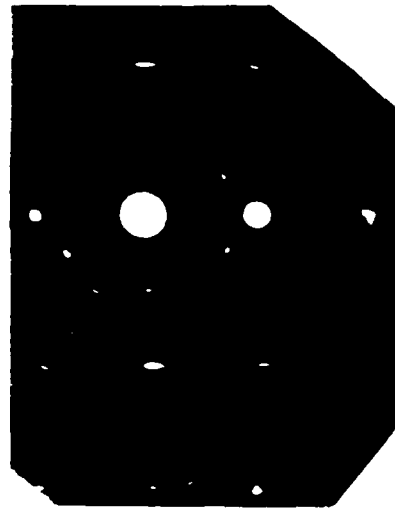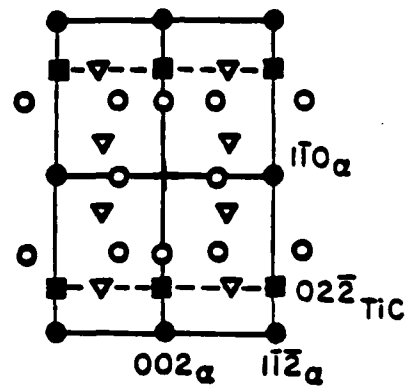
Figure 5-14: a.) CDF electron micrograph revealing TiC precipitation along dislocations in 600°C/1 hr aged microstructure. b.) actual and c.) indexed diffraction patterns[176]
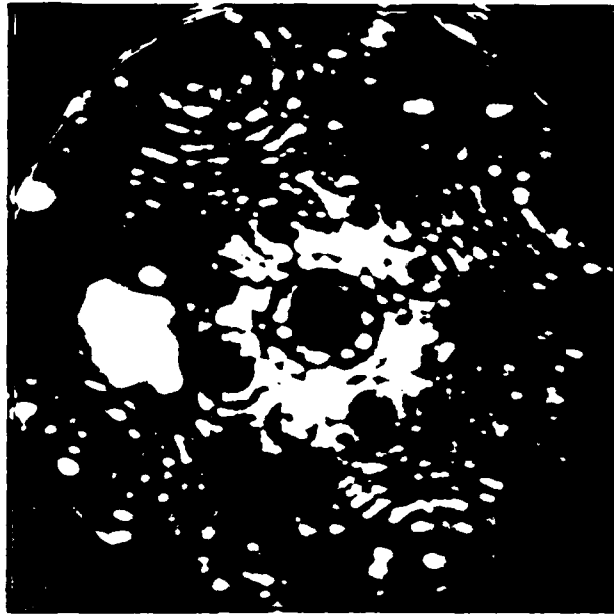
Figure 5-15: Field ion micrograph of well defined TiC precipitates in 600°C/1hr aged microstructure. Four-fold symmetry of underlying matrix image indicates {100} plane normal

5.1.3. Mechanical Properties

An understanding of the effect of internal hydrogen on the mechanical properties of this or any alloy system must start with a sufficiently detailed knowledge of the base material properties such as strength, work hardening capability, toughness, etc. These factors are directly correlatable from the microstructural characteristics outlined in the previous section.

The principle mechanisms of strengthening in microalloyed grades are grain refinement and particle dispersion strenghtening[17,137]. The roles of these factors are manifested in Fig. 5-18 which summarizes the yield and ultimate tensile strength levels of this material. The normal range of strength levels achieved in HSLA steels varies from 300 to 600 MPa[3]. Acicular ferrite steels usually possess yield strengths around 500 MPa in the as-quenched condition but this can be increased by ~ 100 MPa by straining and age hardening near 600°C. The higher strength levels observed in this alloy probably
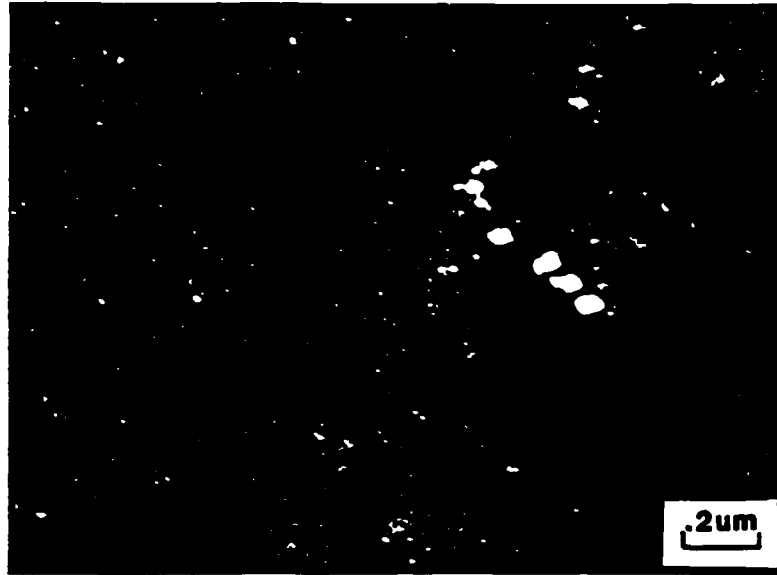
a

b

Figure 5-16: Microstructure resulting from 700°/1hr aging. Coarsening of Ti(C,N) particles is shown in a.) and partial· recrystallization of the microstructures is shown in b.). Compare with Figure 5-2 and Figure 5-14

a

.5μ
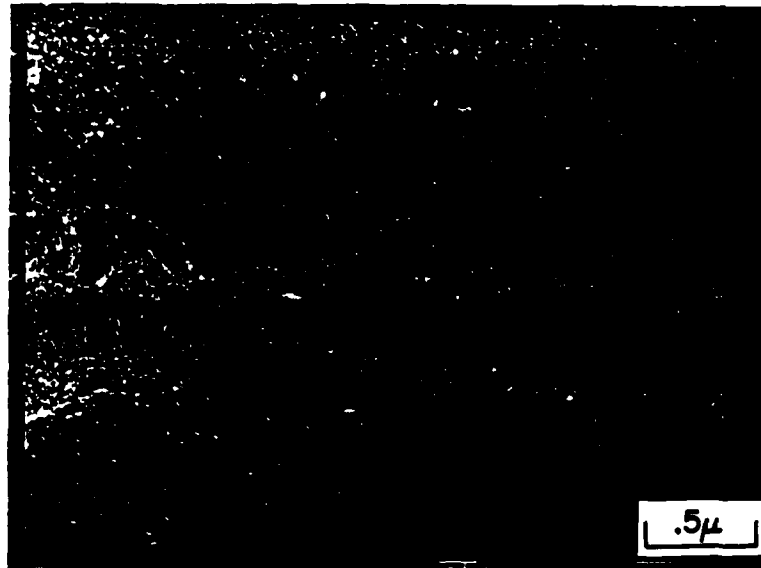
b

Figure 5-17: Matching a.) bright field and b.) dark field illustrating dense TiC precipitation resulting from 900°C/1hr aging

stem from solid solution strengthening due to Mn and Si as well as the effect of Mn on hardenability. It has been shown that Mn delays high temperature transformation to polygonal ferrite hence favoring transformation to acicular ferrite which possesses greater strength and ductility owing to the finer grain structure and high mobile dislocation density.

Thermal Treatment	Fe$_3$C	TiC	Estimated TiC Density	Theoretical TiC Density	Comments
AQ/1HR	None	None (FIM)	-	-	Isolated Fe$_3$C Found but not prevalent
400/1HR	Coarse Lath Boundary Agglomerates 0.25μm x 400Å THK 0.6μm x 800Å THK	None (FIM)	-	-	
500/1HR	Thin Lath Boundary Platelets 0.8μm x 600Å THK 0.5μm x 400Å THK	d ~ 11Å (FIM)	5 x 10^{16} cc^{-1} (FIM)	6.0 x 10^{18} cc^{-1}	TiC density estimated during field evaporation of specimen
500/10HR	Lath Platelets 0.65μm x 500Å 0.6μm x 1000Å	d ~ 16.5Å (FIM) d ~ 30Å (TEM)	1 x 10^{17} cc^{-1} (TEM)	1.93 x 10^{18} cc^{-1}	TiC Density Estimated from TEM DF image and 500-1000Å thick specimen
600/1HR	None	d ~ 21Å (FIM) d ~ 60Å (TEM) 30-120Å observed	3.8 x 10^{16} cc^{-1} (TEM)	9.37 x 10^{17} cc^{-1}	
700/1HR	None	d ~ 75Å 60-6000Å observed	1.37 x 10^{16} cc^{-1}	2.05 x 10^{16} cc^{-1}	
900/1HR	None	d = 150Å 50-2000Å OBJ	2.7 x 10^{16} cc^{-1}	1 x 10^{16} cc^{-1}	

Table 5-2: Summary of aging microstructures formed in Heat V113

The engineering stress-strain curves for longitudinally oriented specimens for four heat treated conditions are shown in Fig 5-19; these were chosen for comparison since their yield strength levels were nearly constant. The 700°C/1hr treatment gave a substantially lower yield strength due to partial recrystallization and it will not be considered here. It can be seen from these curves that although the yield strength levels are virtually constant, the work hardening capability for the various microstructures differs. Although the differences are small, the as-quenched and 600°C/1hr conditions do appear to work harden over a wider range as compared to the 400°C and 500°C aged microstructures. As stated previously, the role of residual stresses associated with martensite islands in the as-quenched microstructure may be to activate more dislocation sources in a uniform way during plastic deformation. This mechanism is also held to be partly responsible for the smooth continuous yielding displayed by this alloy, seen as well in other acicular ferrite steels. After aging at 400°C and 500°C, these stresses are removed, diminishing the uniformity of plastic deformation and reducing the work hardening capability. After the 600°C aging, however, the microstructure possesses a dense precipitate population. Although some coherency with the matrix is likely, it is improbable that these particles are sheared by moving dislocations owing to their high hardness (3000 HV, 0.02kg as compared to 800 for martensite)[3]. This may give rise to enhanced dislocation multiplication, through a double cross-slip type mechanism, as dislocations by-pass these particles.

From the tensile test traces in Fig. 5-19, it is evident that precipitation strengthening is not a principal strengthening agent in the longitudinal direction. Conversely, the transverse direction strength data, as summarized in Fig. 5-18 show a more distinct upward trend with aging temperature. There are several possible causes for this apparent anisotropy of properties. One possible cause is a crystallographic texture, as discussed in the literature review. This possibility was discounted since an X-ray diffractometer examination found no evidence for a significant preferred orientation. Light metallography provided no evidence for anisotropic grain shape. Additionally, the use of identical cross head speeds on the different sized specimens made for these tests resulted
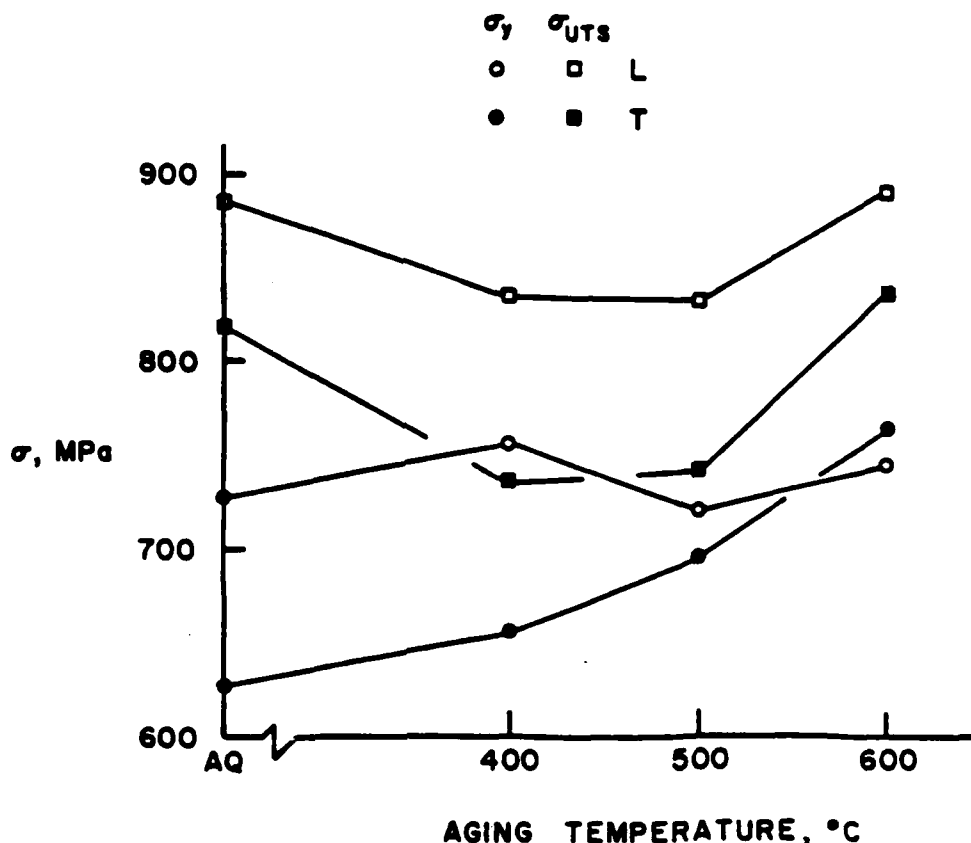
Figure 5-18: Tensile response of Heat V113 for orientations and aging treatments shown.

in slightly higher (3 times) strain rate for the shorter, transverse specimens. Faster strain rates usually result in decreased elongation and ductility in BCC metals. It is likely that the interlath orientations of the ferrite on a sub-packet scale may be of importance for a better characterization of this discrepancy.

The general conclusions which can be drawn from these studies are:

1. The heavily dislocated acicular ferrite microstructure and residual stresses in the matrix give rise to moderately high strengths levels, continously smooth yielding and significant work hardening capacity.

2. This work hardening capacity is diminished by low temperature aging but may return following high temperature aging (600°C) presumably through particle induced cross-slip.
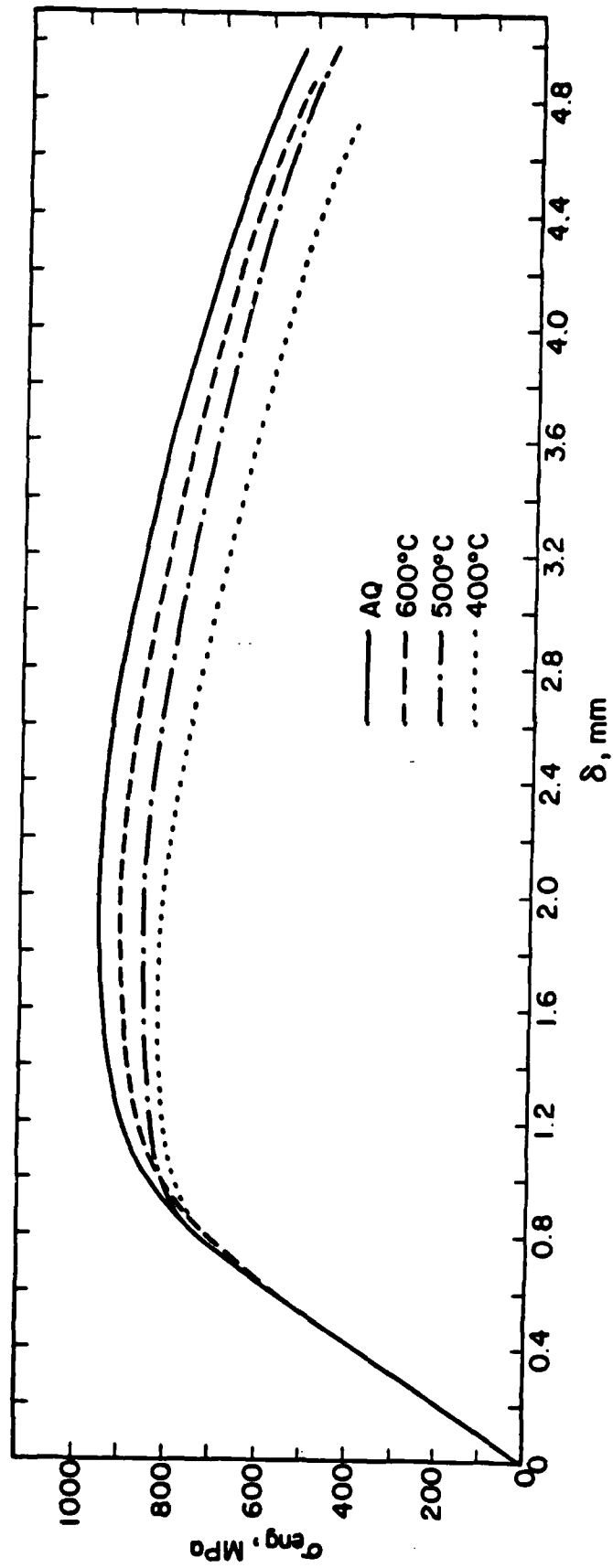
Figure 5-19: Tensile test traces for various agings of Heat V113. $\delta = 1-l_o$.

5.2. Hydrogen Trapping Studies

The quantitative determination of trapping in this alloy, as discussed in Chapter 4, was obtained through the use of an electrochemical permeation technqiue, first developed by Devanathan and Stachursky[33,141] and later adapted for use on ferritic materials by Pressouyre[28]. These experiments yield hydrogen flux vs time curves which can be interpreted through the use of several mathematical models, most of which use the original concept of McNabb and Foster[142].

As stated earlier, the details of the use of electrochemical permeation on α-Fe have been discussed in detail by Pressouyre, but the more important points are reiterated here for clarity. In general, the exact procedure of Pressouyre was employed here, except where alternative operating conditions were stated in the experimental procesure.

Reliable analysis of flux-time curves in these experiments can be severly limited by either a dominating input or surface concentration effect. The hydrogen uptake from the cathodic cell in such an experiment can be a complicated function of surface chemistry, surface roughness and the presence of surface films. It is important to be able to ensure that these effects do not dominate the form of the flux-time curve. Pressouyre[28] found that the presence of Ti in solution produced a significant surface effect likely due to trapping of hydrogen by titanium just under the surface. The use of an electrochemically deposited palladium layer on the surface ($\sim 1000 \text{Å}$) was found to ensure similar entry conditions for all alloy chemistries under consideration. This stems in part from the very low overvoltage now necessary for adsorbed hydrogen to recombine to form molecular hydrogen. This will limit the quantity of hydrogen which will pass through the Pd layer and thus prevent saturation at the interface (causing blisters) or just under the surface of the Fe membrane (causing surface cracks or blisters) Also, the solubility of H in Pd is quite high ranging from 1×10^5 to 6×10^5 ppm at $20\,^\circ C$ and 0.005 atm H_2[141]. This, together with the high diffusivity in Pd, of around 3.2×10^{-7} cm^2/sec ensures that a continuously supplied, constant, low concentration of hydrogen covered the plated iron membrane. At the same time, the Pd layer provides a corrosion resistant barrier to the $0.1\underline{N}$ NaOH solution.

Important electrochemical parameters include the input current density and the integrity of the Fe-Pd interface. Pressouyre found that the steady state flux of hydrogen, J_∞, increased proportionally to the square root of the charging current, $i^{1/2}$, for low current density values. At sufficiently high densities, a "hump" in the flux-time curve was observed which was related to either surface trapping, crack or blister formation, or impermeable layer formation. Pressouyre showed through the use of his electrical analog[30] model that surface trapping could explain the occurrence of such a "hump" in the permeation transient, but his experimental evidence indicated that it was observed only for Fe membranes not coated with Pd. It is more likely that one or both of the later two possibilities are responsible. Specifically, the occurrence of surface blisters can be diminished by lowering the charging current density but this will depend on the integrity of the interface. If an oxide or corrosion product scale is present prior to Pd plating, a lower charging current density will be tolerated since hydrogen will build up at this interface and cause blistering. Experimentally, this presents a repeatability problem since all specimens must (or should) be tested at a constant input coverage and hence input current density. The most important conclusion to this discussion is that great care must be exercised when the final preparation of a permeation specimen is attempted. In the course of this study, it was determined that close adherence to the preparation technique described in Chapter 2 was necessary in order to avoid breakdown of the specimen surface by blistering. This was especially important for comparison of separate results from different experiments.

An additionally important technique parameter was the agitation level of the cathodic charging cell. In practice, it was found that the hydrogen flux rate increased dramatically with progressively lower stirring speeds. This suggests that convective movement in the solution somehow aids the surface diffusion of H_{ads} and thus recombination. As a result, constant, reproducible stirring speeds were essential for relative comparison of flux data. This was accomplished by ensuring that the specimen-mechanical stirrer distance and stirring speed was constant throughout all tests.

After accounting for these "artifact" effects on the observed flux-time data, o. may then interpret the form of the data using a suitable model. The model m. . adaptable to most boundary conditions and coordinate systems is the McNabb and Foster[·2] formalism which assumes that Fick's second law may be modified to:

$$\frac{\partial C}{\partial t} + N \frac{\partial n}{\partial t} = \nabla D \nabla C$$

where $C = C(x,t)$ is the concentration of diffusing hydrogen, N is the single trap type density, n is the fractional trap occupancy, D is the general diffusivity and t is time. The accompanying equation which characterizes the nature of the traps is

$$\frac{\partial n}{\partial t} = kC(1-n) - pn$$

where k is the capture rate and p is the release rate from a particular trap type. In order to facilitate manipulation of these terms the equations are usually presented in dimensionless form

$$\frac{\partial u}{\partial \tau} + \frac{\partial v}{\partial \tau} = \frac{\partial^2 u}{\partial \xi^2} \tag{5.1}$$

and

$$\frac{\partial v}{\partial \tau} = \lambda u - \mu v \tag{5.2}$$

where:

$u = C/C_o$ with C_o being the input concentration

$v = nN/C_o$

$\tau = Dt/a^2$ where a is characteristic length

$\lambda = Nka^2/D$

$\mu = pa^2/D$

$\xi = x/a$ where x is distance from input surface

General solutions to these equations have been obtained by Caskey and Pillinger[131] using finite difference techniques. Representative solutions are shown in Fig. 5-20 which illustrate the effect of trapping parameters (a and b) and input concentrations levels (c) on the form of the flux time curve.
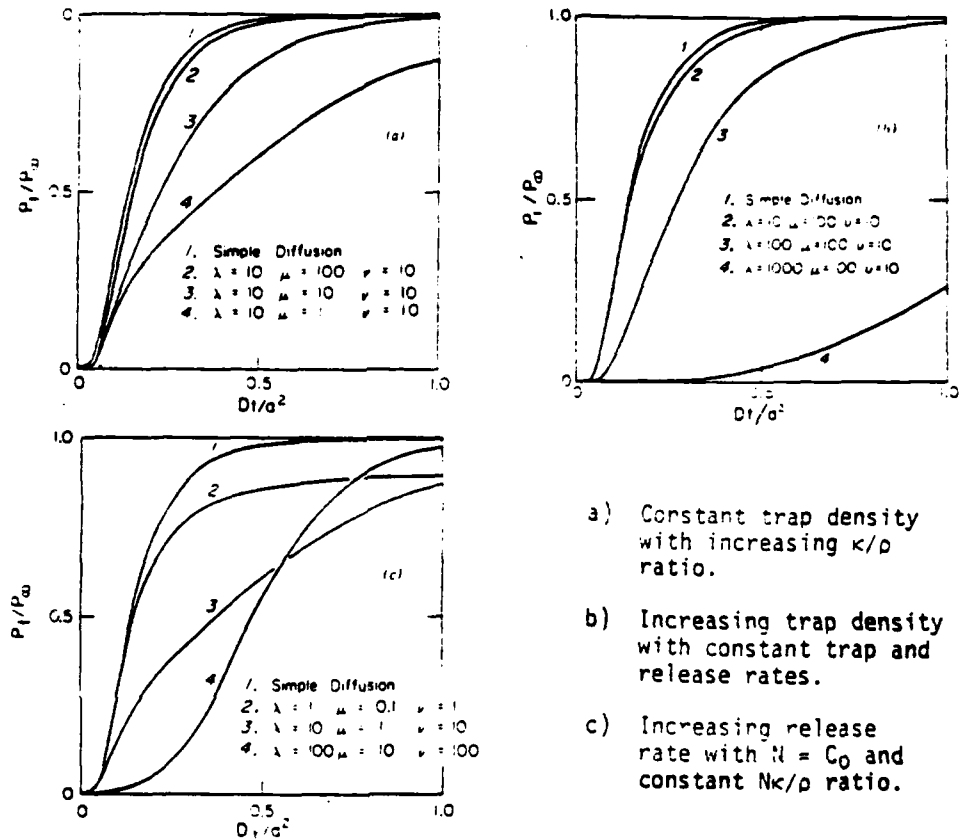
Figure 5-20: Predicted form of normalized flux versus dimensionless time for varying trapping parameters, as given. Caskey and Pillinger[131]

Although qualitative observation of flux curves may point to some general trapping trends, a more exact quantitative description is necessary. McNabb and Foster determined the modified lag time using their formalism for a one-dimensional solution to the governing differential equations. For simple diffusion theory (no trapping) the time lag is simply defined by integrating the quantity of hydrogen which has permeated a membrane versus time. At longer times, this relation is linear and an extrapolation of the slope to the time curve defines t_L where:

$$t_L = \frac{a^2}{6D}$$

For the case of a single population of reversible traps, this becomes:

$$t_T = t_L \left[1 + \frac{3a}{\beta} + \frac{6a}{\beta} - \frac{6a}{\beta^3} (1+\beta) \ln (1+\beta) \right] \quad (5.3)$$

where:

$$a = N\frac{k}{p}$$

$$\beta = C_o \frac{k}{p} = \frac{n}{1-n} \quad (5.4)$$

Limiting cases of this equation are useful for analyzing trapping. For dilute occupancy of traps (β, n << 1), the situation examined by Pressouyre, this reduces to:

$$\frac{t_T}{t_L} = 1 + a \quad (5.5)$$

or

$$\frac{D_o}{D} = 1 + a \text{ where } D_o \text{ is the lattice}$$

diffusivity and D is the measured or apparent diffusivity. For the case of trap saturation,

$$\frac{t_T}{t_L} = 1 + \frac{3N_T}{C_o} \quad (5.6)$$

Pressouyre[28] confirmed that his studies were indeed performed for a low coverage situation by observing a linear dependence of D versus N_T (Ti concentration), while simultaneously varying the input charging current density (i.e. C_o) to show that this did not affect the measured D values. Since virtually the same charging conditions as his were used in the present study (1.0 mA/cm^2 versus 0.8 mA/cm^2), although on a more complicated microstucture, the same assumption of low coverage will be assumed.

Recently, Iino[143,144] has expanded on this analysis by solving a similar set of dimensionless differential equations for combined reversible and irreversible trapping. The diffusion equations are then expressed by;

$$\frac{\partial u}{\partial \tau} + \frac{\partial v}{\partial \tau} + \frac{\partial w}{\partial \tau} = \frac{\partial^2 u}{\partial \xi^2} \tag{5.7}$$

with

$$\frac{\partial v}{\partial \tau} = \lambda u - \mu v \tag{5.8}$$

and

$$\frac{\partial w}{\partial \tau} = \kappa u \tag{5.9}$$

where now $w = N_i n_i / C_o$ and $\kappa = N_i k_i a^2 / D$ with the "i" subscript denoting irreversible trapping. These equations are not exact since they have already been modified for the case of low hydrogen concentration, C_o, and coverage, n. Using suitable boundary conditions and the Lapace transform method of solving differential equations, a solution for the flux is obtained. In this case, the inflection in the predicted flux curves is enhanced in the presence of increasing irreversible trapping. According to this model, the presence of an inflection indicates that strong traps exist in the microstructure.

Pressouyre[28,29] has also analytically accounted for the presence of reversible and irreversible traps. This approach relies on acquiring successive permeation transients through a membrane. The shape of the first transient is assumed to be affected by all traps of consequence in the material. After attaining steady state, the hydrogen source is removed and the flux decays to zero. If the identical source is then reapplied, the second polarization of the membrane will produce a flux-time curve which will reflect, at the temperature of interest only the presence of significant reversible, weak traps since it is assumed that the irreversible traps retain their hydrogen during the decay process. If the second polarization transient is shifted significantly to shorter times, this then indicates the presence of irreversible trapping.

The successive permeation transients obtained from the various microstructures in this study indicate that both of these models may be suitable for a qualitative understanding of trapping in this material. As an example, consider the first and second polarization transients through the as-quenched microstructure. As shown in Fig. 5-21, it is evident from the shape as well as the close time correlation of these curves that this microstructure primarily exhibits reversible trapping. Fig. 5-22 presents apparent diffusivity values calculated from time-lag values from all of the heat treatments studied. Using an estimate of 6×10^{-6} cm^2/s^{29} for the lattice diffusivity of trap-free iron and an effective diffusivity of 1×10^{-7} cm^2/sec, as measured from the as-quenched microstructure, one may estimate

$$\frac{k}{p} N_T \sim 60 \qquad (5.10)$$

$\frac{k}{p}$ in this case must be the average for all reversible traps in the microstructure, including grain boundaries, inclusions, dislocations and Ti substitutional atoms. Additionally, this factor also incorporates any multiple occupancy coordination factors such as were discussed by Pressouyre. In his study, Pressouyre was able to assume that reversible traps other than Ti atoms were insignificant in his material since the matrix was essentially well-annealed iron. His values of $(k/p)N_T$ ranged from approximately 1 to 10. Due to the more complex nature of the microstructure (and hence trapping) in the present study, an independent evaluation of k/p or N_T is quite difficult.

However, if the value of N_T is estimated between $10^{20} - 10^{21}$, this then gives estimates of k/p ranging from $6 \times 10^{-19} - 6 \times 10^{-20}$ cm^3/atom. Considering the accuracy with which the D_{app} can be detected and the assumption of N_T, this represents a reasonable agreement with Pressouyre's findings. Therefore, the character of reversible trapping in the as-quenched microstructure is assumed to be reasonably equivalent to that found by Pressouyre in his study.

The permeation transients for 400°C and 500°C age microstructures, shown in Figures 5-23 and 5-24 display a transient "plateau" as was predicted and observed by
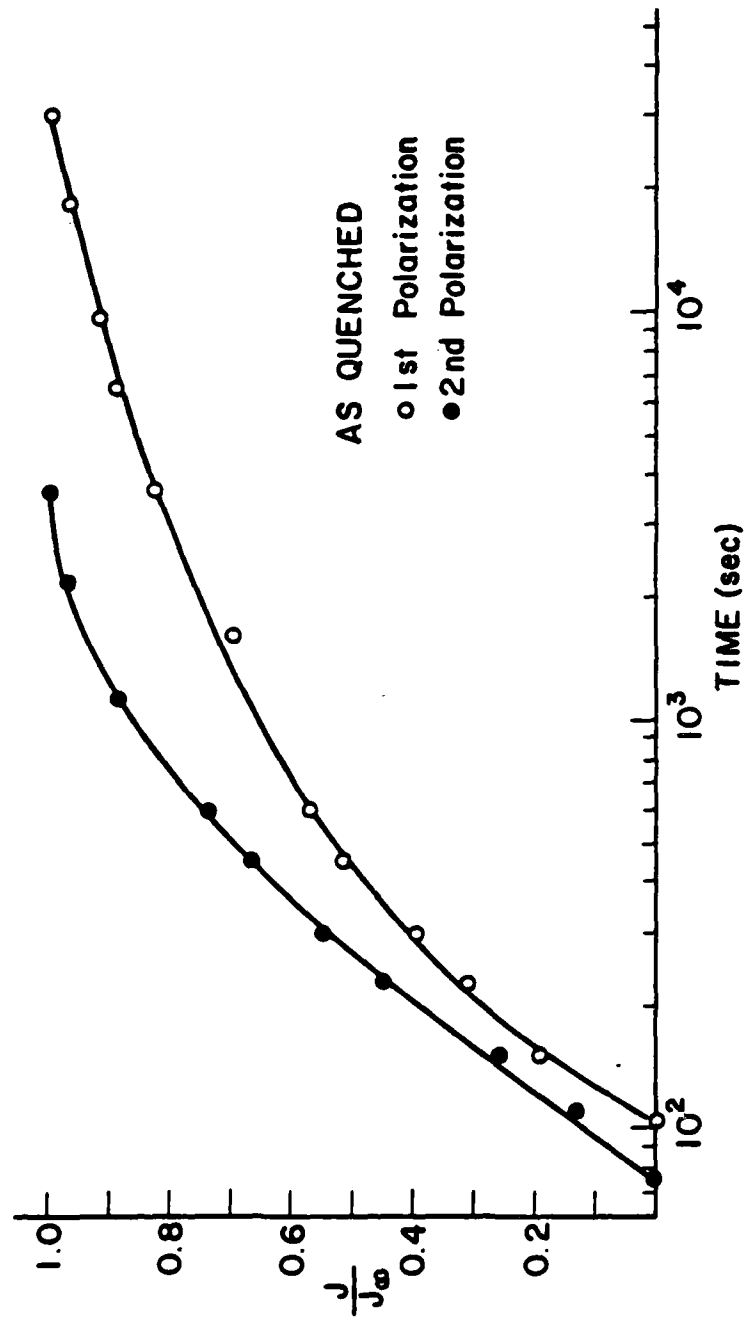
Figure 5-21: Normalized hydrogen permeation flux transients through microstructure as-quenched from 1200°C

END

FILMED

DTIC
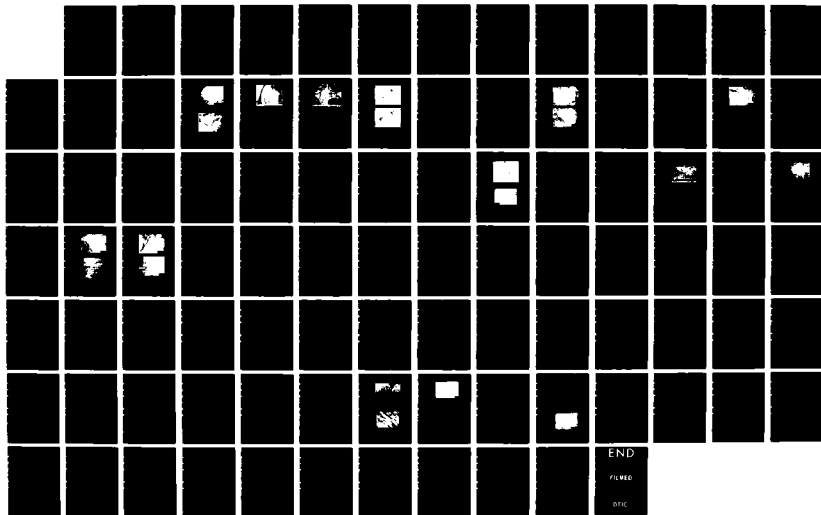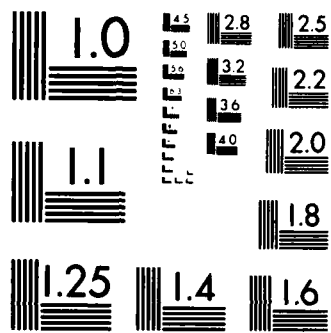
MICROCOPY RESOLUTION TEST CHART

NATIONAL BUREAU OF STANDARDS-1963-A
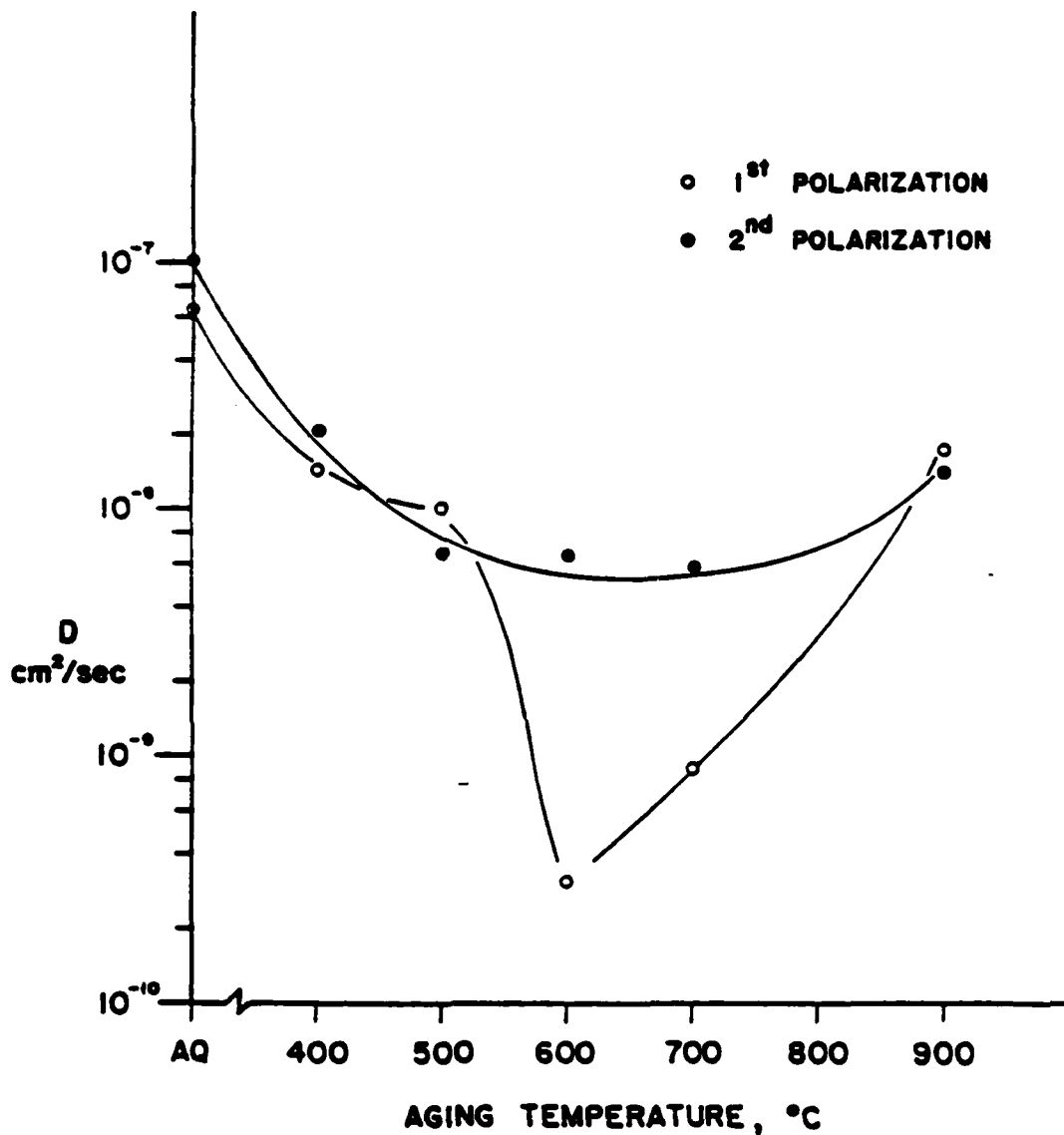
Figure 5-22: Summary of apparent D values calculated from permeation transients using time-lag methods

Iino[36] for reversible trapping. Iino analytically predicted that an intermediate plateau may be observed for the case of reversible trapping if the dimensionless release rate, μ, is sufficiently small. This condition holds only for low hydrogen concentration and low trap coverage, n << 1. His predicted curves are shown in Figure 5-25 where in this case, a

plateau is observed for λ/μ values greater than 10. This plateau thus seems to indicate that the nature of trapping in these microstructures is fundamentally different from the population present in the quench and unaged microstructure, but that over long time periods, the traps are still reversible. Since the only visible change in microstrucure at the 400 and 500°C aged conditions was the appearence of carbide phases, it is logical to assume that these phases may be responsible for the change in reversible trapping character.

A difficulty in pinpointing this discrepancy is possibly related to the wide range of values assigned to the binding enthalpy, E_B, between hydrogen and the ferrite-cementite interface. Robertson and Thompson[134] have determined the average binding enthalpy of hydrogen to traps in three different microstructures of 1045 steel through the use of the time-lag approach. In a spheroidized microstructure, the average binding enthalpy estimated was 36.4 kJ/mole; in pearlite this value fell to 18.4 kJ/mole and in tempered martensite, the value was 29.7 kJ/mole. In contrast, Lacombe et al.[133] have estimated the binding enthalpy at $\geq$ 84 kJ/mol for cementite. Recent studies by Hong and Lee[135] estimate this energy at 10.85 kJ/mol. In addition to this, an equally wide discrepancy in binding energies for H to dislocations in iron have been reported; ranging from as high as 60 kJ/mol[132] to as low as 27 kJ/mol[145].

◆

The hydrogen flux transients shown in Figure 5-26 for the 600°C aged microstructure now represent a case of deep, irreversible trapping, by comparison with both the models of Iino and Pressouyre. Considering first the analysis of Iino, the form of the first polarization flux from Figure 5-26 definitely corresponds closely to the transient predicted by this author for increasingly stronger trapping. That this trapping is predominantly irreversible is evident from the form of the second polarization flux which is shifted to significantly shorter times for all values of J/J_∞. As predicted by the model of Pressouyre, the irreversible (at room temperature) trapping in this microstructure now shifts the subsequent curve to shorter times, greatly altering the apparent diffusivity in this microstructure; the ultimate result being that the diffusivity is one and a half orders of magnitude fast__ during the second transient.
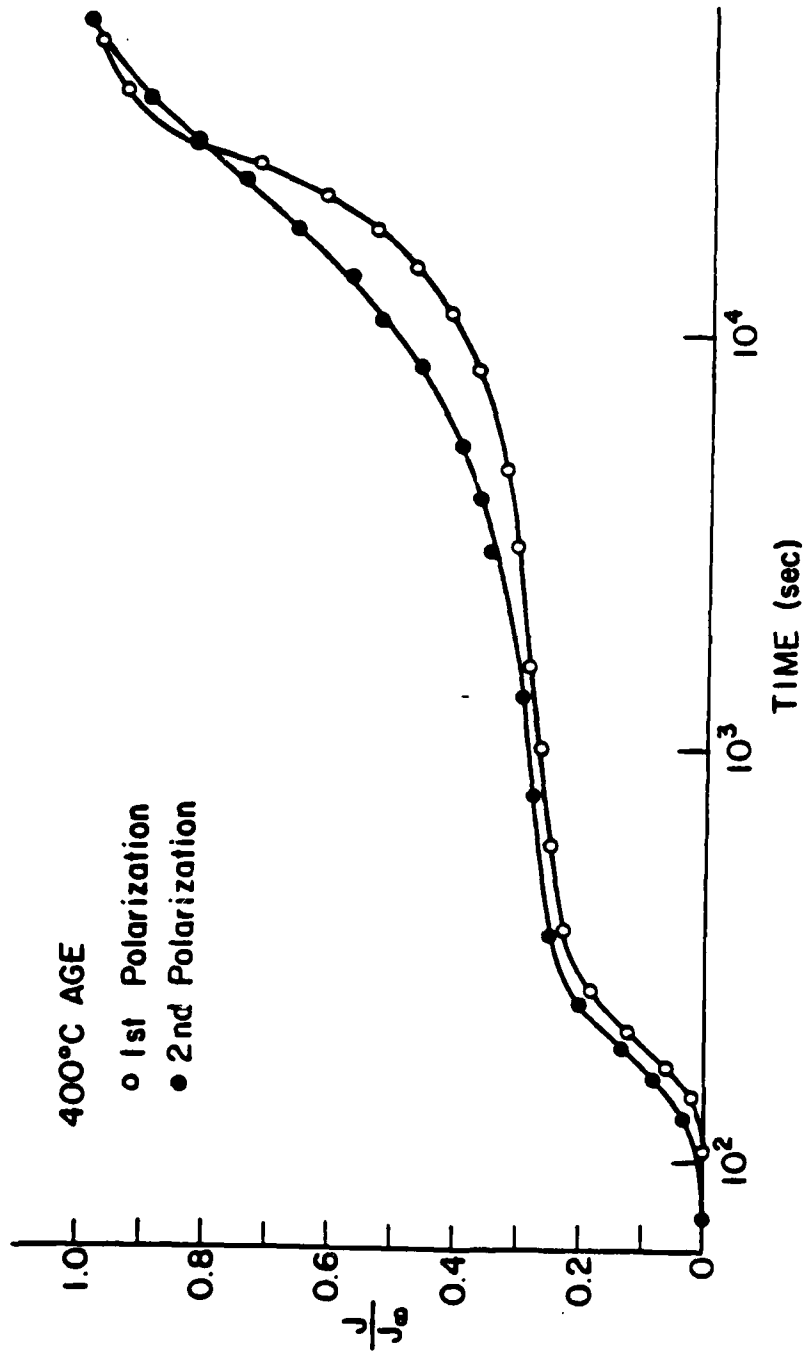
Figure 5-23: Normalized hydrogen permeation flux transients through microstructure aged 1hr at 400°C
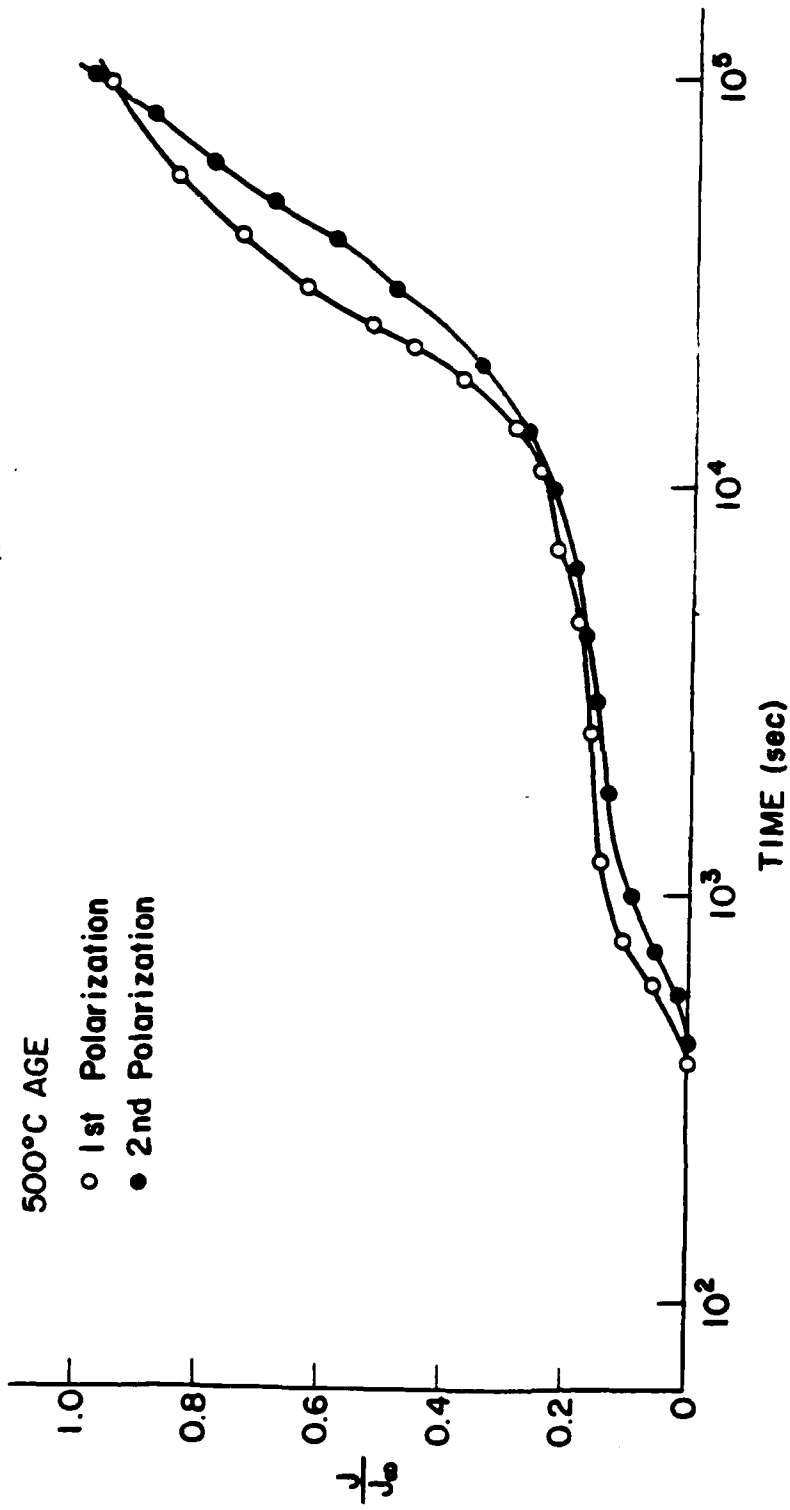
Figure 5-24: Normalized hydrogen permeation flux transients through microstructure aged 1 hr at 500°C
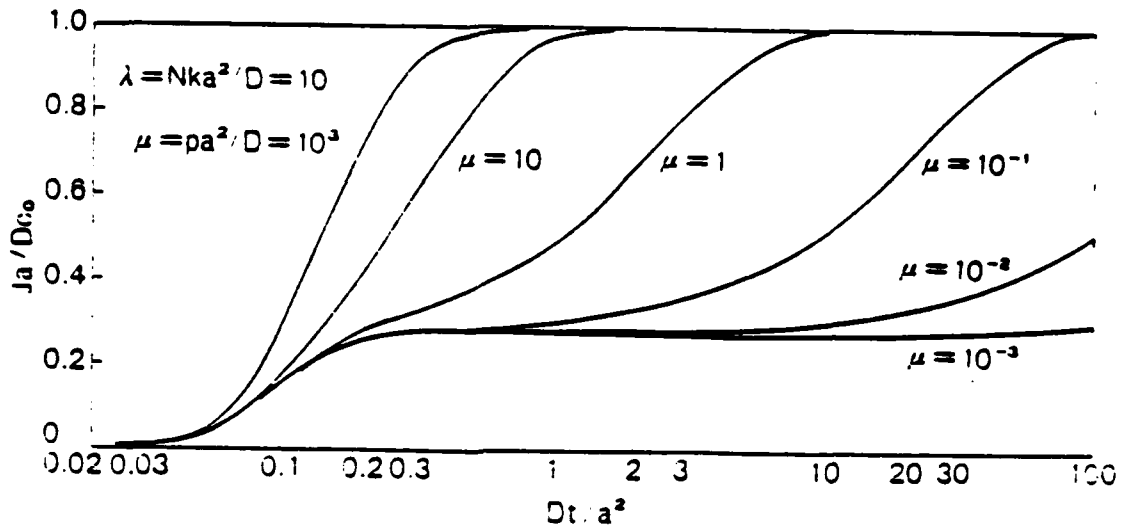
Figure 5-25: Predicted form of flux-time curves for increasing λ/μ of single reversible trap density. Iino[36]

An estimate of the irreversible trapping energy is possible from this data. Using the diffusivity values from Tables 5-3 and 5-4 for the $600°C$ aged microstructure one may assume again that:

$$\frac{D_o}{D} = 1 + \frac{k}{p} N_T \tag{5.11}$$

If the second polarization D value is used for D_o, the first polarization value for D and the estimated TiC precipitate density ($\sim 3.8 \times 10^{-16}$ cc^{-1}) for N_T, one obtains:

$$\frac{k}{p} N_T \sim 5 \times 10^{-16} \tag{5.12}$$

using

$$k/p = \exp (E_g/RT) \tag{5.13}$$

an estimate of $E_g \sim 87$ kJ/mole is found. This does not differ significantly from the values found by Pressouyre[29] and Lacombe[133], considering the error in N_T and the assumption of single atom trapping by each particle.

The flux transients for the $700°C$ aged specimen as shown in Figure 5-27 indicate
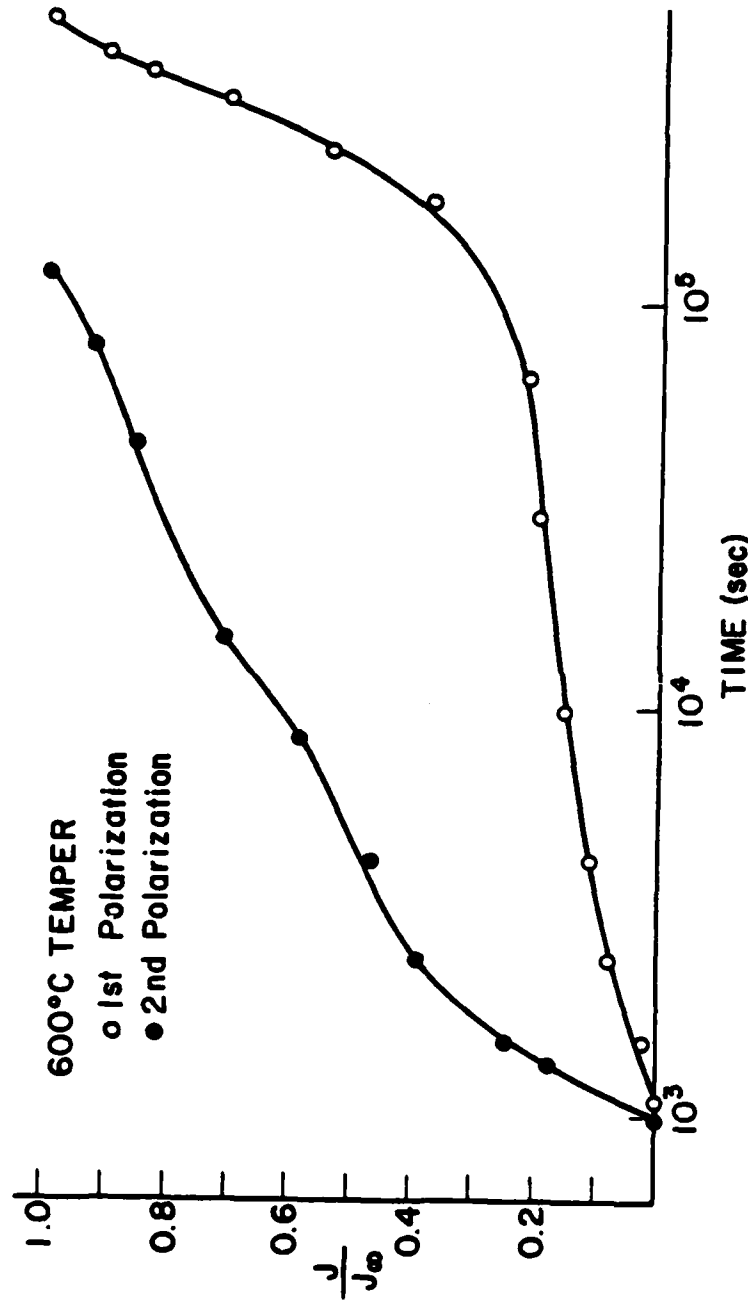
Figure 5-26: Normalized hydrogen permeation flux transients through microstructure aged 1hr at 600°C

that irreversible trapping still occurs but now the second polarization curve again develops somewhat of an intermediate plateau. At $900°C$ (Fig. 5-28), the intermediate plateau is again present but, as in the $400°C$ and $500°$ aged microstructures, both transients overlap. The indication here is that the nature of at least some of the TiC traps has changed to having a weaker interaction with hydrogen, possibly more similar to that between cementite and hydrogen. Additionally, it is possible that the loss of surface-to-volume ratio associated with coarsening in this temperature regime may also diminish the trapping capablity of the TiC phase. In the case of the $900°C$ aged microstructure, a significant quantity of TiC precipitates has coarsened sufficiently so that coherency strain interactions may be no longer appreciable. The work of Youle et al.[16] predicted incoherency at TiC interfaces for particles 200Å in size and larger. Since many precipitates in the $900°C$ aged microstructure ranged as high as 2000Å, this later suggestion is reasonable. It should be noted that this trend of decreased D with aging temperatures $> 600°C$ was also observed in the study of Takahashi et al.[51]. These authors concluded that fine *coherent* TiC particles were the most effective traps in their alloy. These combined findings suggest that trap strength may be decreased by the loss of coherency about TiC precipitates.

Additionally, as summarized in Figure 5-29, diffusivity values for each thermal treatment were also calculated using the breakthrough method, which is obtained from the measurement of the time for the first detectable flux for hydrogen;

$$t_{breakthrough} = \frac{L^2}{15.3D}$$ (5.14)

It has been noted by previous researchers that this method should be relatively free of internal hydrogen concentration effects but may reflect and can often be dominated by the effects of slow surface reactions. By comparison of Figure 5-22 with Figure 5-29, it is immediately obvious that, with the exception of the as-quenched microstructure data, the breakthrough D values which always more rapid than the time-lag D values, and somewhat dispells any argument for a slow surface reaction, while raising the possibilty that fast "short circuit" paths for hydrogen diffusion exist in these microstructures.
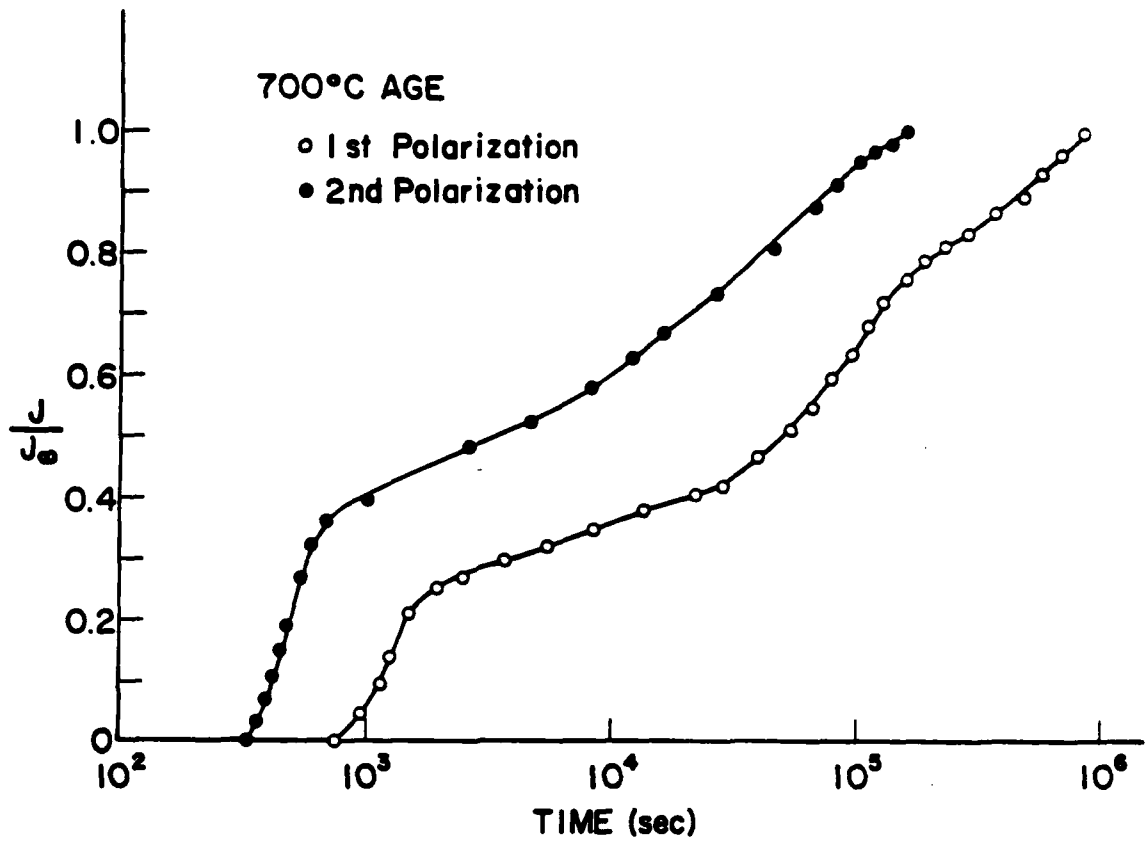
Figure 5-27: Normalized hydrogen permeation flux transients through microstructures aged 1hr at 700°C
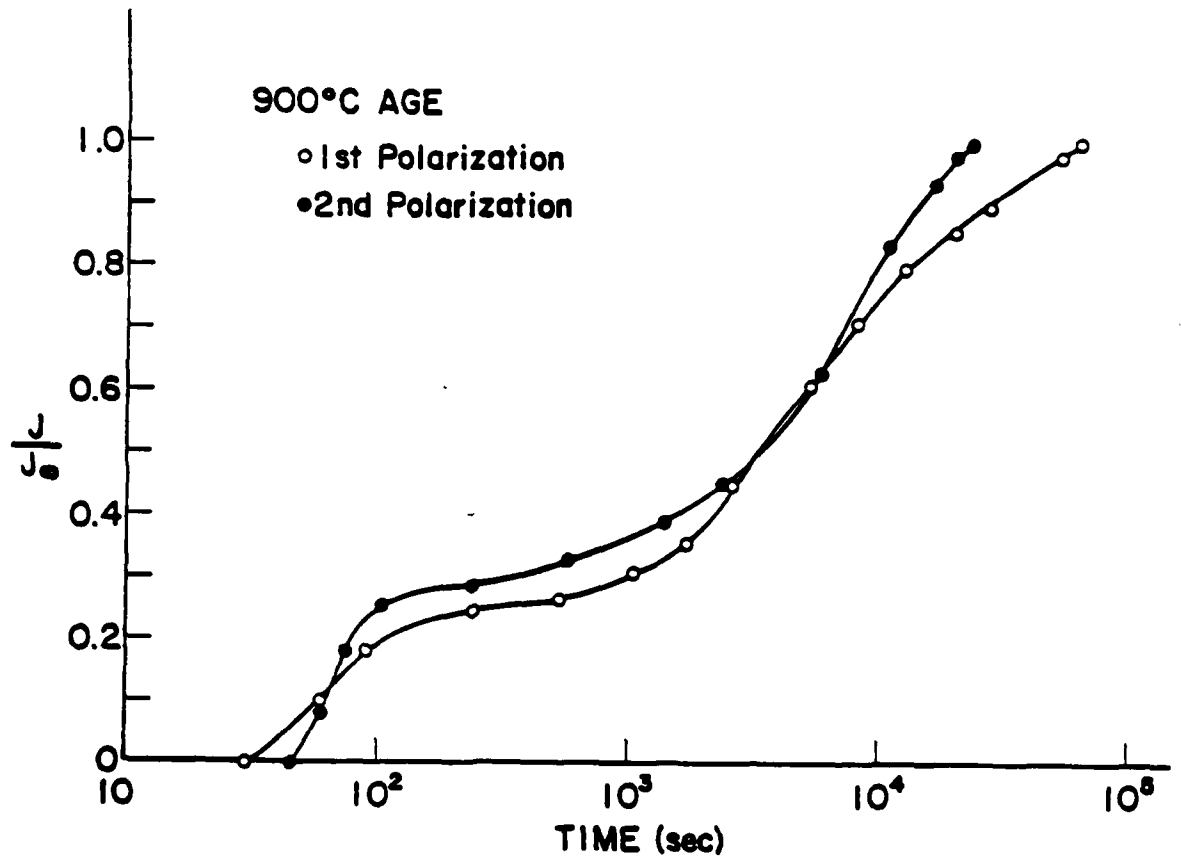
Figure 5-28: Normalized hydrogen permeation flux transients through microstructure aged 1hr at 900°C
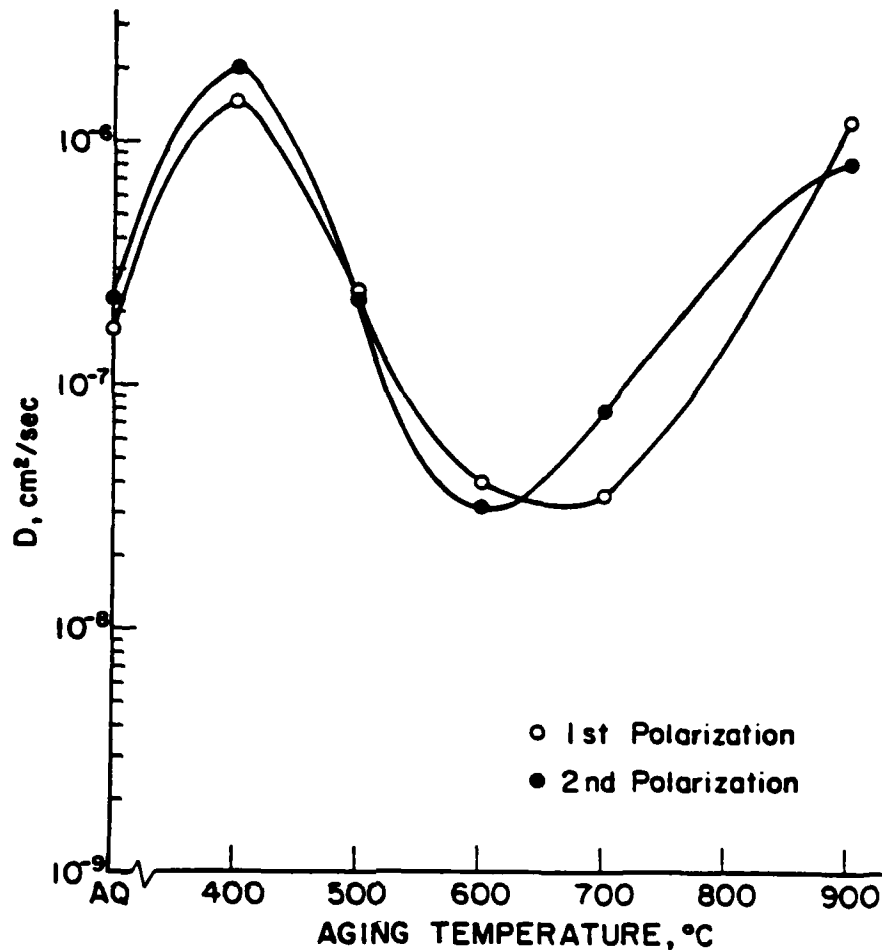
Figure 5-29: Summary of apparent D values calculated from permeation transients using breakthrough time method.

In this case, the initial emerging hydrogen flux may traverse the microstructure via a grain boundary or dislocation pipe diffusion path, avoiding strong trapping effects. This is evident by the close correspondence of the first and second polarization values over all aging treatments, in contrast to the time lag values. This indicates that the breakthrough method may not be effective in detecting the presence of strong trapping. The somewhat surprisingly high D value at 400°C aging apparently points to the most efficient fast flux paths, which may have consequences on the mechanical integrity in the presence of hydrogen. The lower D values at 600°C and 700°C aged conditions suggest that the high density of TiC precipitates may alter this "fast flux" mechanism in some way. Since the possible fast diffusion paths and preferred nucleation sites for TiC are probably the

same (i.e. dislocations and grain boundaries), this is not unreasonable. At higher temperatures, the diffusivity once again rises, indicating again that significant changes in trapping by TiC occur on coarsening (notwithstanding the decreased trapping in the recrystallized structure).

In summary, these hydrogen permeability studies lead to the following observations:

1. The hydrogen flux data for the microstructures studied here suggest that the analyses of both Iino[36] and Pressouyre[29,30] are appropriate for evaluating the strength and character of trapping.

2. Intermediate plateau occurrence was apparently associated with cementite (400°C and 500°C aging) and coarse ($>200\text{Å}$) TiC precipitation, indicating delayed release rates from these trap sites.

3. Irreversible trapping, as comparatively judged from sequential hydrogen flux transients, was caused by fine ($<200\text{Å}$) TiC precipitates, suggesting that the interfacial structure of these particles may be important in the trapping mechanism.

4. Comparison of breakthrough and lag-time diffusivity values indicated that the former were always faster, suggesting that the hydrogen may be able to diffuse by "short-circuit" paths. Additionally, sequential breakthrough values were identical, regardless of microstructure, indicating that these values are relatively unaffected by trapping.

5.3. Hydrogen Effects on Tensile Properties

The tests on cathodically charged and Cd plated smooth, cylindrical tensile specimens have revealed a surprisingly complex variety of responses to internal hydrogen. A summary of the results is as follows:

1. At aging temperatures less than 500°C and for one hour duration, failure proceeds by a ductile mechanism. Increased %RA at failure has been associated with diminished cementite precipitation and nucleation of fine(~10Å) TiC clusters.

2. Two distinct fractographic features were identified on ductile fracture surfaces; randomly dispersed, circular tearing topography surface (TTS)[136] "facets" and finer microvoids.

3. At aging temperatures above 500°C, an abrupt plateau in ductility occurs with a transition to brittle intergranular fracture. Microstructurally, this failure mode was associated with direct precipitation of TiC phase and metalloid segregation to grain boundaries.

The %RA versus aging treatment data summarized in Fig. 5-30 compares the charged and

Thermal Treatment	Thickness cm	$t_{Breakthrough}$ sec	t_{Lag} sec	$D_{Breakthrough}$	$D_{Lag} \frac{cm^2}{sec}$	J_∞, $\mu A/cm^2$	C_o, $\frac{H \ atoms}{cm^3}$
As-quenched	0.0165	105	656	1.69×10^{-7}	6.92×10^{-8}	6.3	8.92×10^{15}
400/1 hr	0.04318	84	21,340	1.45×10^{-6}	1.46×10^{-8}	4.8	1.78×10^{16}
500/1 hr	0.0394	420	27,300	2.41×10^{-7}	9.5×10^{-9}	5.0	1.69×10^{16}
600/1 hr	0.0221	800	2.53×10^5	3.99×10^{-8}	3.2×10^{-10}	42.5	8.06×10^{16}
700/1 hr	0.0203	750	76,140	3.59×10^{-8}	7.32×10^{-10}	23.5	4.09×10^{16}
900/1 hr	0.0239	30	5,700	1.24×10^{-6}	1.67×10^{-8}	9.8	2×10^{16}

Table 5-3: Summary of Experimental parameters measured for Analysis of Initial Hydrogen Transients through Heat V113

Thermal Treatment	Thickness cm	$t_{Breakthrough}$ sec	t_{Lag} sec	$D_{Breakthrough}$ $\frac{cm^2}{sec}$	D_{lag} $\frac{cm^2}{sec}$	J_∞ $\frac{\mu A}{cm^2}$	C_o $\frac{H\ atoms}{cm^3}$[a]
As-quenched	0.0165	75	445	2.37×10^{-7}	1.05×10^{-7}	4.9	2.37×10^{-7}
400/1 hr	0.04318	60	14,940	2.0×10^{-6}	2.08×10^{-8}	6.0	2.0×10^{-6}
500/1 hr	0.0394	432	39,924	2.3×10^{-7}	6.47×10^{-9}	5.0	2.3×10^{-7}
600/1hr	0.0221	990	10,440	3.22×10^{-8}	8.8×10^{-9}	34.5	3.22×10^{-8}
700/1 hr	0.0203	330	12,360	8.16×10^{-8}	5.56×10^{-9}	28.5	8.16×10^{-8}
900/1 hr	0.0239	45	5,700	8.29×10^{-7}	1.67×10^{-8}	9.8	8.29×10^{-7}

[a] $C_o = \frac{J_\infty L}{D_o F}$; J_∞ = steady state flux, A/cm^2; L = Thickness, cm;

$D_o = 7.3 \times 10^{-5}$ cm^2/sec, F = 96, 500 coul/eq.

Table 5-4: Summary of experimental parameters measured for Analysis of 2nd Hydrogen Transient through Heat V113

uncharged ductilities for longitudinal (rolling direction) specimens at approximately equivalent strength levels. It is important to note that the uniformly high uncharged ductility, about 70% in this case, indicates that the precipitation sequences and inclusion densities do not affect the uncharged ductilities to any great extent.
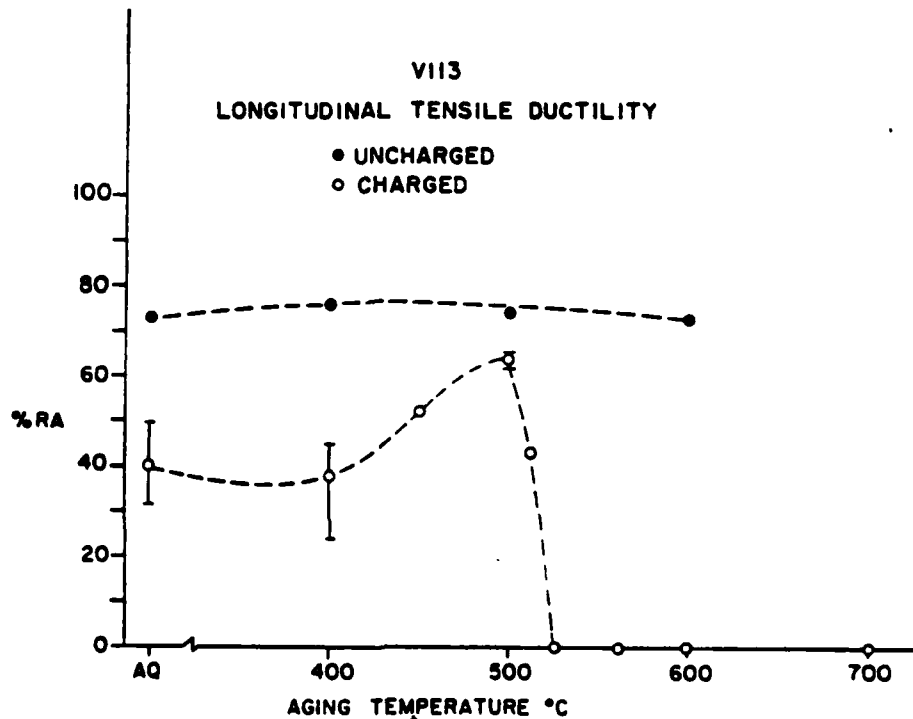
Figure 5-30: Comparison of charged and uncharged ductility response for longitudinal tensile testing of Heat V113.

It is useful to first consider the unaged through $500\,^\circ C$ aged data since apparently microstructure does play a role in hydrogen induced ductile fracture over this range. The %RA ranged from an average low of 39% for the unaged and $400\,^\circ C$ conditions to a high of 64% in the $500\,^\circ C$ aged specimens. The fracture modes and ductilities of the quenched and $400\,^\circ C$ aged microstructures were virtually identical, as demonstrated by the data of Table 5-5 and Figures 5-31 and 5-32. As stated above, two distinct fracture

modes were observed in these conditions; TTS and MVC. The TTS facets, ranged from 100-700 μm in diameter enabling them to be viewed by the naked eye in most cases, as seen from Figure 5-33. Interrupted tests were run in order to ascertain the point in the stress-strain history of the specimen at which these facets formed. Charged specimens which were charged and pulled past the necking strain were unloaded and baked at 150°C for over 2 hours. When later pulled to failure, these specimens displayed no facets although inclusions were still found at the center of dimples. Thus on specimens where one or more very large facets formed, the separation clearly occurred very late in the necking process. In general then, it is believed that overload fracture then directly ensued following the separation of the faceted areas.

Table 5-5: Summary of charged and uncharged longitudinal tensile properties of Heat V113 for various heat treatments.

Thermal Treatment	$\bar{\sigma}_y$, MPa	$\bar{\sigma}_{UTS}$, MPa	%RA Uncharged	%RA Charged	ΔRA, %
As-Quenched	765	895	73	39	34
400°C/1hr	761	838	75	38	37
500°C/25min	784	826	-	50	-
500°C/1hr	753	819	75	64	11
500°C/3hr	735	784	-	47	-
500°C/10hr	805	-	-	0	-
510°C/1hr	812	868	-	44	-
525°C/1hr	826	-	-	0	-
550°C/1hr	896	-	-	0	-
600°C/hr	716	903	73	0	73
700°C/1hr	680	-	-	0	-

The plastic tearing ridges formed by this mode formed a "river marking" pattern, not unlike that of a conventional cleavage mode. These river patterns in many cases
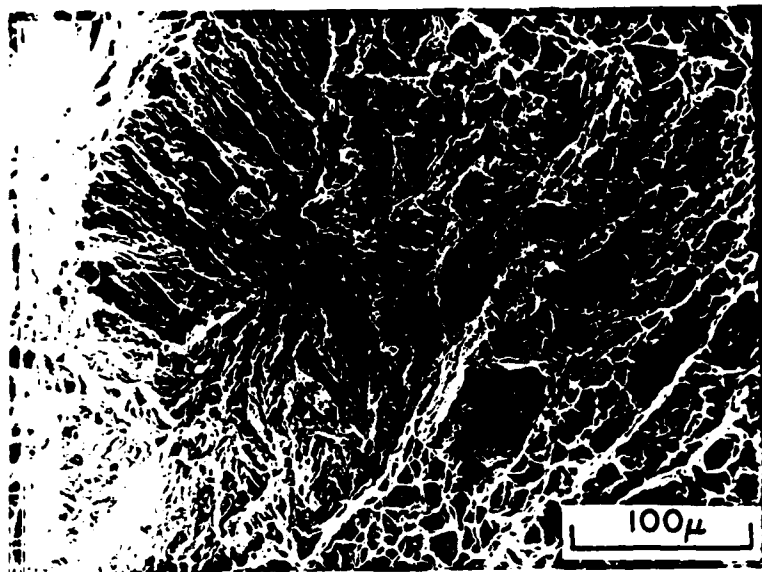
Figure 5-31: SEM micrograph of tensile fracture surface of specimen as-quenched from 1200°C. Hydrogen charged 5hr.
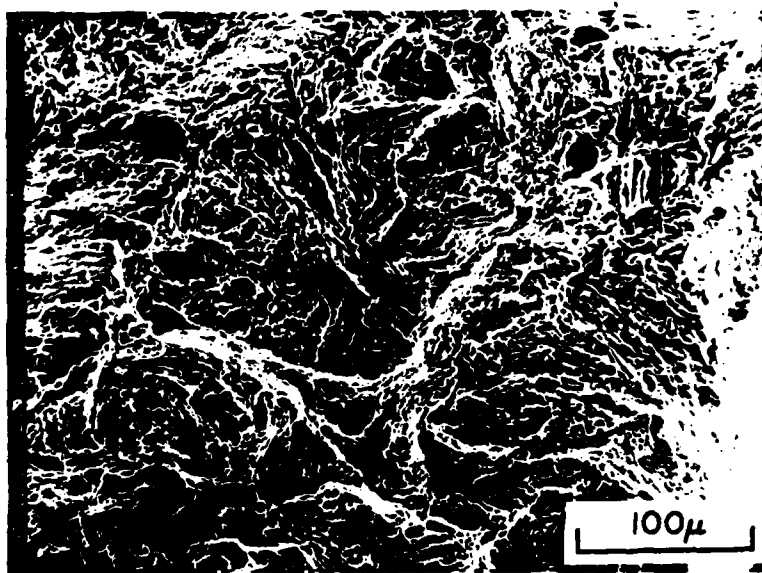
Figure 5-32: SEM micrograph of tensile fracture surface of specimen aged 1hr at 400°C. Hydrogen charged 5hrs.
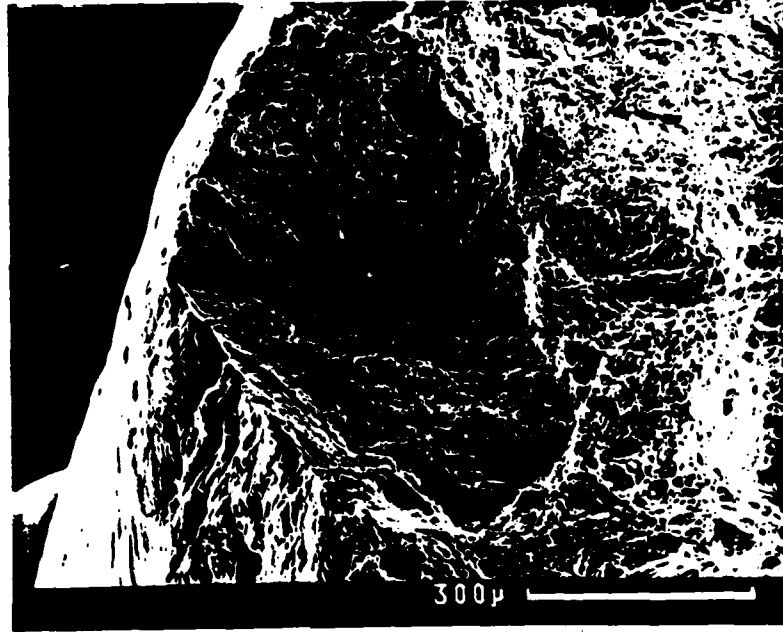
Figure 5-33: Tearing Topography Surface facet shown near edge of charged tensile specimen fracture surface

originated at the center of the usually circular facets and inclusions or inclusion clusters were often associated with these areas, as shown in Figure 5-34. Using X-ray energy dispersive spectroscopy and X-ray mapping capabilities, the constituent population for atomic number $Z > 13$ of these particles were determined and in most cases, were found to be Al and Ti. Examples of this analysis are shown in Figure 5-35a and 5-35b where X-ray mapping shows an inclusion cluster that is Al rich at the center and apparently Ti rich at the periphery. The abundance of Al-rich inclusions is not surprising since this steel, as well as commercial grade Ti steels, must be thoroughly killed prior to the addition of Ti to the melt to avoid TiO_2 formation. The clustering of Ti around Al in these inclusions indicates that the Al oxide (and nitride) particles which form first are favorable nucleation sites for Ti bearing inclusions which generally form at lower temperatures. Some, but not all Ti inclusions were found to contain S, as discussed earlier, which suggests that these may be τ-Ti_2S, $Ti_4C_2S_2$ or $Fe_{0.5}TiS_2$. The study of Craig and Krauss[60] also revealed similar flat facets emanating from complex chemistry inclusions in a study of pre-charged 4130 steel. For reasons which were not established, additional spurious chemical components of the inclusions of this study included Ca and Cr.
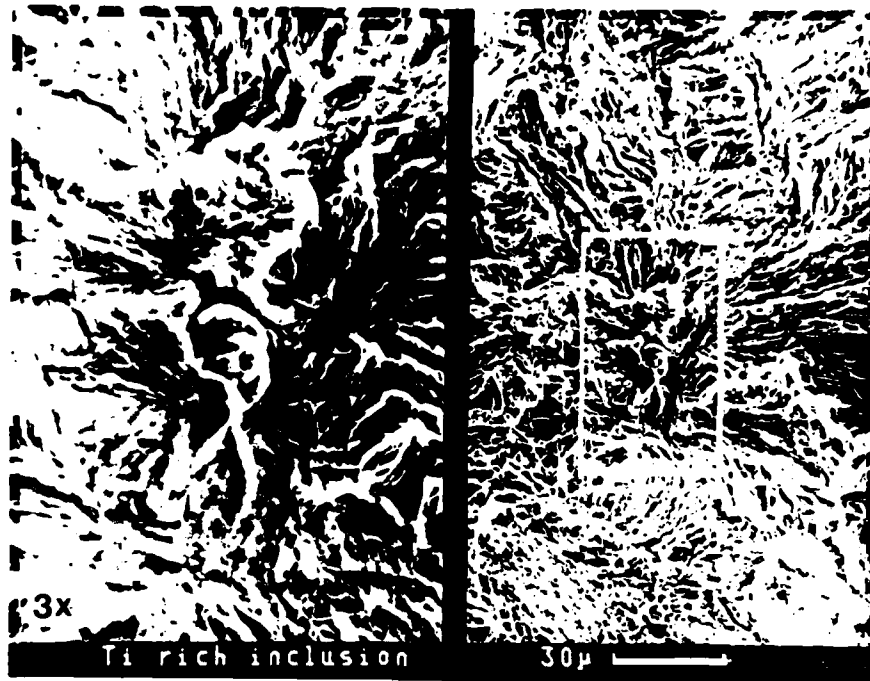
Figure 5-34: SEM Micrograph showing typical TTS fracture radiating from inclusion particle

The change in fracture processes within these facets is important since their formation was not observed in uncharged specimens and therefore it must be concluded that this fracture mode transition is directly related to hydrogen enrichment in and around the stressed regions associated with an inclusion. A similar type of fracture mode has been observed in notched low alloy HY-130 steels tested in a hydrogen gas atmosphere. These authors[61] found this failure mode along surfaces of maximum shear stress and noted the similarity to the glide-plane decohesion found by Bernstein[47] and Nakasato and Bernstein[146]. They further noted that this fracture involved both interfacial decohesion (of the martensite laths) and transcrystalline cracking. Earlier studies of Lee, Goldenberg and Hirth[148] on precharged and dynamically charged U-notch specimens of 1095 steel revealed that voids formed at lower macroscopic strains than in the uncharged condition, leading to the conclusion that hydrogen promoted plastic instability along characteristic slip lines. Recently Kim and Morris[149] examined hydrogen cracking in a 5.5 Ni cryogenic steel and found a similar fracture mode. Their TEM study of the initiation of cracking revealed that cracks did indeed form along {110} and {112} planes as expected for glide plane
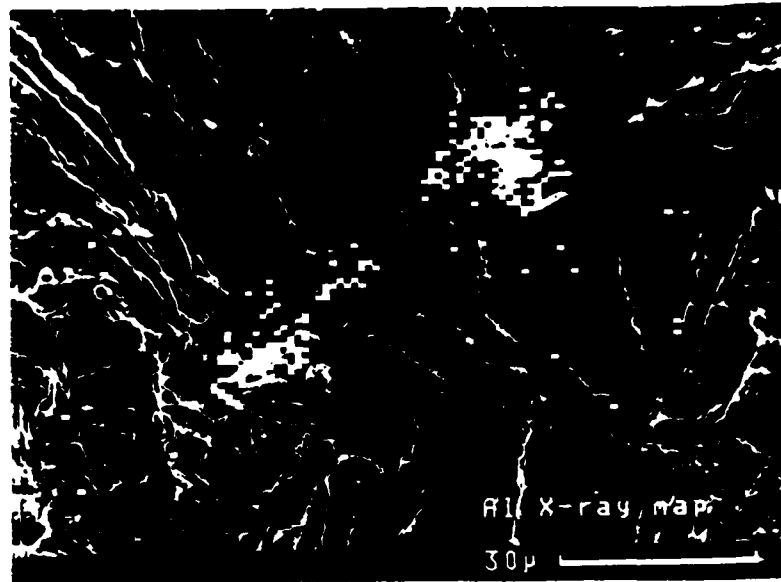
a
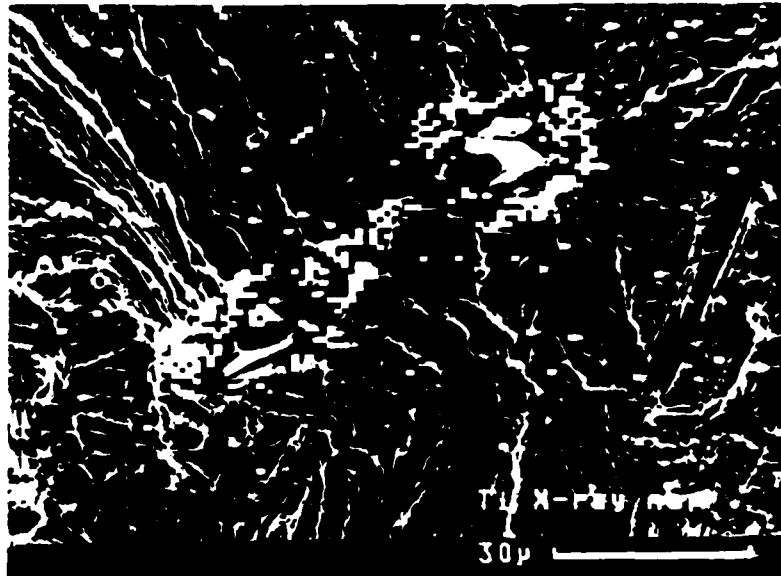
b

Figure 5-35: SEM micrograph of inclusion found at center of Fig. 5-33 with overlapping digital X-ray maps for a.) Al and b.) Ti

decohesion, but they noted that these were also common low angle boundary planes in lath martensite. They finally concluded that embrittlement occurred by interlath cracking due to hydrogen. In light of these other studies, the subtle change in fracture mode within the TTS facets here suggests that hydrogen may cause plastic instability or may alter the slip mode.

In a definitive review of tearing topography surface (TTS) fracture, Thompson and Chesnutt[136] proposed likely mechanisms of formation; one possibility was that it is a type of microvoid coalescence in which there are many closely spaced active nuclei. If subsequent void growth or premature strain localization intervenes, then well developed voids would not be observed. Premature strain localization may be exactly what Lee et al.[155] observed in their study, and localized plasticity would explain the intense transgranular cracks found by Bernstein along {110} planes in iron. There is supporting evidence for strain localization or localized plasticity. Earlier work has shown that sufficient H in the α-Fe matrix may increase the mobility of screw dislocations and promote planar (intense) slip. Additionally, apparently direct evidence for H induced dislocation mobility has been produced by Birnbaum[152] and workers using in-situ TEM studies. They found that the trace of "saw-tooth" fracture surfaces on thin foils of α-Fe strained in a hydrogen atmoshere contained the {110} plane. Hence, there exists in the literature a possibly consistent connection between H-induced slip planarity, strain localization and formation of void free ductile fracture.

The common thread of these findings, among others, is a microstructural alteration of slip ease, planarity and distribution due to a sufficient, albeit unknown, concentration of hydrogen. Another implication of such a mechanism, as suggested by McMahon[147], is that such a dislocation structure would enhance dislocation ingress along slip bands and a dynamic transport role of dislocations, if one exists. Such accelerated transport through intense "slip bands" may also explain the large extent of these facets compared to the size of the central inclusions.

What is also important in the findings of the present study is a lessened propensity for such facet formation at aging temperatures near $500\,^{\circ}C$. Fractography of these specimens Fig. (5-36 a and b) does not reveal any large facets although a number of secondary cracks, not present in the uncharged condition, are now evident. High magnification examination of these cracks reveals internal features which may be slip markings, as shown in Figure 5-36b. It should be recalled that this microstructure differs from those at lower aging temperatures in that the $500\,^{\circ}C$ aged microstructure was shown to contain a relatively high density of fine TiC particles and a somewhat less coarse Fe_3C particle distribution.

This tendency for increased resistance with the onset of TiC formation was somewhat obscured by the results of transverse orientation tensile tests as graphically summarized in Figure 5-37. In this case, the as-quenched and $500\,^{\circ}C$ treated specimens showed lower hydrogen-induced ductility than the $400\,^{\circ}C$ aged specimen. This discrepancy may be related to the uncharged anisotropy which was discussed earlier. It is possible in this case that the slightly higher strain rate (~ 3 times higher) could account for a shift in the material properties, but supporting evidence concerning this is lacking. An interlath orientation relation or an anisotropic inclusion distribution could be possible reasons for such an effect.

In summary, the embrittlement susceptibility of tensile specimens aged at temperatures up to $500\,^{\circ}C$ indicated that:

1. Inclusions play a central role in these microstructures as sites of hydrogen enrichment and premature fracture.

2. Ductile fracture initiated about inclusions does not produce a microvoid coalescence separation but instead a TTS fracture mode, suggesting that enriched hydrogen in these areas may promote a glide-plane decohesion mechanism.

3. Microstructures containing fine TiC clusters were found to have greater inherent resistance to TTS facets formation in longitudinal, 25 mm. (6.4 mm. diam.) length specimens.

In contrast to both of these results, which apparently point to a mechanism of

a

100μ
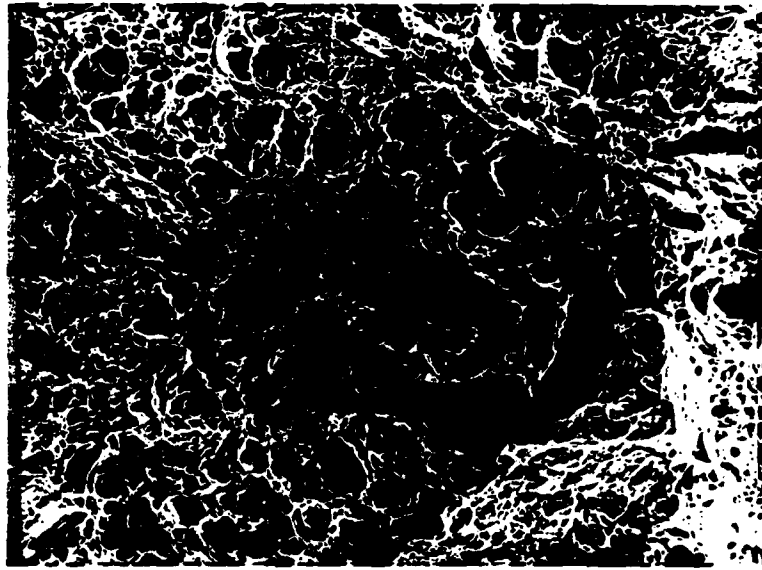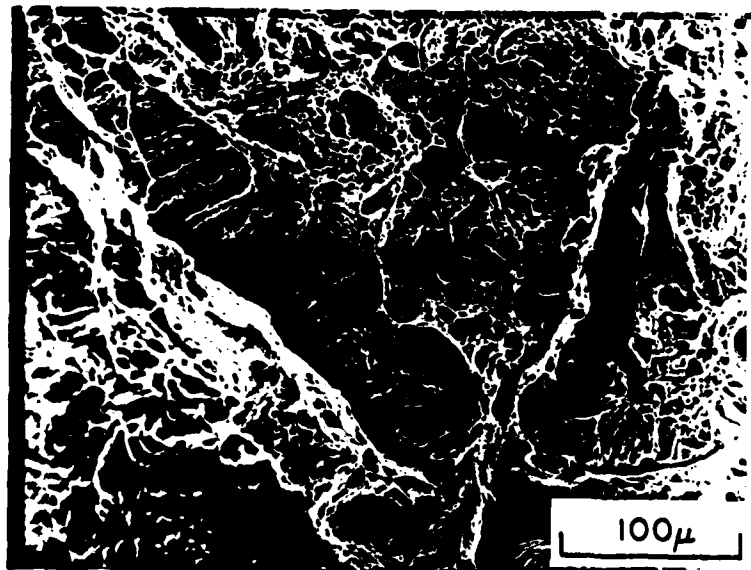
b

Figure 5-36: SEM micrographs of tensile fracture surfaces from specimen aged 1 hr. at 500°C a.) Dimpled surface and secondary cracks: b.) Close-up of secondary cracking revealing slip marking features.
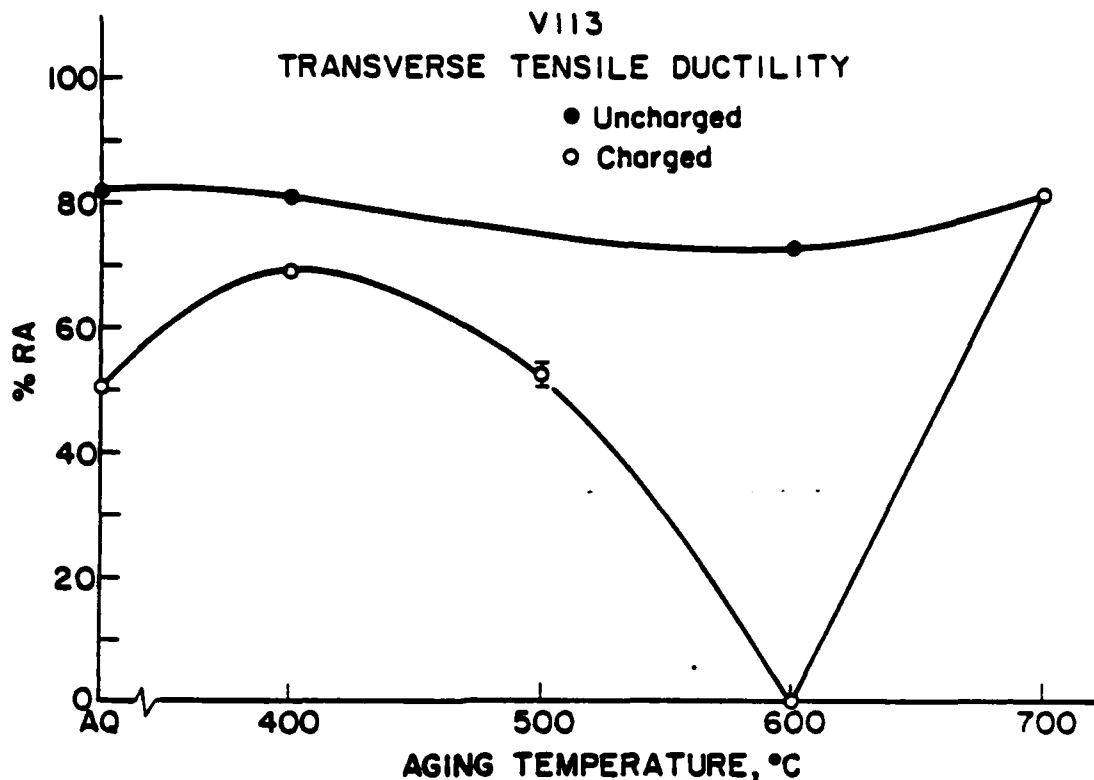
Figure 5-37: Comparison of charged and uncharged ductility response for transverse tensile testing of Heat V113

hydrogen embrittlement rooted in plasticity effects, the fracture mode of specimens aged at 525°C through 700°C was effectively totally intergranular with respect to the prior γ grain structure and dramatically no %RA was measured at any of these temperatures.

As with the trend in ductile response, it is important to keep in mind the microstructural aging reactions operative in this temperature regime; at temperatures between 500°C and 600° direct precipitation of TiC occurs with little or no Fe_3C precipitation evident.

SEM examination of fracture surfaces from the 600° aged specimen (Fig. 5-38) reveal that they are smooth and devoid of large particles, which have been associated with brittle fracture in previous studies[32,174]. Additionally, secondary intergranular cracks were often observed. The "clean" features of these grain boundary facets and their similarity to

Table 5-6: Summary of charged and uncharged transverse tensile properties of Heat V113 for various heat treatments

Thermal Treatment	$\bar{\sigma}_y$ MPa	$\bar{\sigma}_{uts}$ MPa	%RA, Uncharged	%RA, Charged	ΔRA
As-quenched	663	801	82.4	50.4	32
400/1 hr	700	772	81.6	69.6	12
500/1 hr	694	767	-	52.5	27.5*
600/1 hr	792.8	847	73.6	0	73.6
700/1 hr	601	653	81.6	83.2	0

temper embrittled steel fracture surfaces suggested that a similar mechanism may have been at least partially responsible for this fracture path. Accordingly, Auger electron spectroscopy techniques were employed in order to ascertain whether metalloid species (i.e. P or S) were present at these boundaries in order to understand why these fracture paths were preferred in this aging temperature regime.
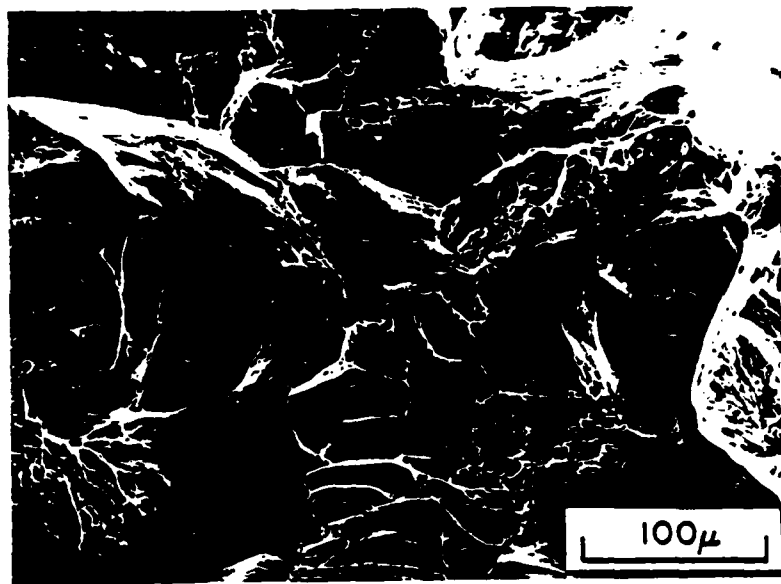
Figure 5-38: SEM micrograph of tensile fracture surface of specimen aged 1hr at 600°C. Hydrogen charged 5hr.

Auger spectra generated from specimens fractured in situ (10^{-9} torr) to produce "clean" γ facets revealed that significant P and sometimes S signals were generated from these surfaces (Figure 5-39). What is not known is how much if any of these species exist at these boundaries at lower temperatures. However, a possible implication of such findings is that these species segregate to the boundaries in a temperature regime concurrent with the direct precipitation of the TiC phase. Previous studies, as covered in the Literature Review, suggest that these two occurrences are often related. The aforementioned study of Ustinovshchikov[83] apparently has established this same sequence (i.e. association of alloy carbide formation with intergranular fracture) in a series of P-doped steels having Mo, V, and Cr as the alloy carbide formers. The development of the transition from transgranular to intergranular fracture in his study of a Mo steel is shown in Figure 5-40, where the chart summarizes the ductility, (given by transition temperature), precipitation sequence (inferred from hardness measurements) and fracture mode (given by either T or I) as a function of aging of time at 550°C. Note that the transition from transgranular to intergranular (and hence to a high transition temperature)

is almost directly related with the peak in secondary hardening and an implied conversion to a solely alloy carbide distribution. This same trend was observed for V and also for Cr, although to a lesser extent. It was suggested by the author that prior to carbide precipitation, the metal solute atoms exist in solution as clusters with other interstials as well as relatively stable P-bearing complexes. Given sufficient time for alloy atom diffusion, the more thermodynamically favored carbide eventually forms, freeing the metalloids to diffuse to grain boundaries. This sequence was supported by the study of Erhart et al.[42] on P segregation in the Fe-Ti-P and Fe-Ti-P-C systems, who showed that phosphorus does interact quite strongly with Ti in solution although the form of the phosphide phase cluster was undetermined. More importantly, they also established that the scavenging action of Ti with P was reduced in all experimental alloys containing carbon. This can be seen from Figure 5-41 taken from this study. The data at carbon levels less than 0.05% C indicate that the carbon-free alloy contained less P at γ grain boundaries (as determined from Auger electron analyses) than the carburized alloys. From these data, the authors also concluded that TiC phase can lower the grain boundary concentration of P by trapping the P at the TiC/matrix interface. It is clear, however, that the formation of stable complexes of Ti and P is more effective in alleviating embrittlement than trapping of P at TiC interfaces.

The specific details of this apparently similar phenomenon in the Ti steel of this study more or less point to the same sequence. Through a detailed examination of the development of intergranular fracture in longitudinal tensile specimens in this temperature regime, Figure 5-42, it appears that a plateau level develops starting at 550°, consistent with this temperature being the lowest at which direct TiC precipitation with no concurrent Fe_3C precipitation occurs. However, the Auger data at 550°C and 600°C as shown in Table 5-7 suggest that although the amount of intergranular fracture does not significantly increase above 550°C, continued enrichment of the metalloid elements at the prior γ boundaries continues to occur at 600°C. Attempts to analyze prior γ boundaries in 700°C specimens were unsuccessful since only a shear dimpled fracture surface was formed at this temperature. This likely results from the lower strength levels of this aged condition.
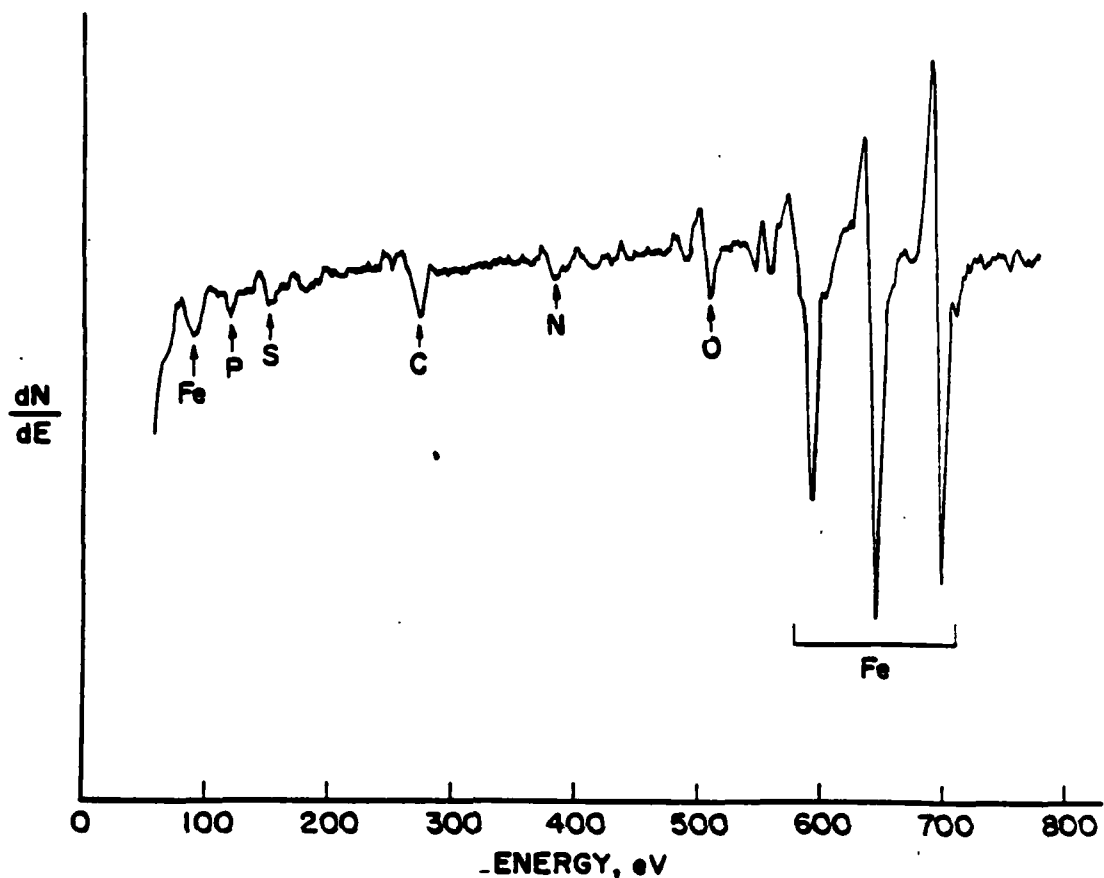
Figure 5-39: General scanning auger spectrum obtained from $600°C/1hr$ aged specimen fracture surfaces. In situ vacuum fracture.

Previous studies of hydrogen embrittlement of high strength steels have established that intergranular fracture is a common mode of failure, suggesting the efficiency of these sites as low configurational energy sites for hydrogen. They would presumably also be preferred for TiC precipitation, as judged by the more intense TiC precipitate density observed along lower angle lath boundaries in this steel. Since the hydrogen trapping results have established that these TiC particles are apparently strong traps for hydrogen it may well be that the hydrogen in solution has been concentrated in these areas, and along with the effect of P, the fracture strength of these boundaries is exceeded well before general yielding. Although this possibility is not unreasonable, the Auger spectrum data do not provide conclusive evidence for or against such a process. One problem in
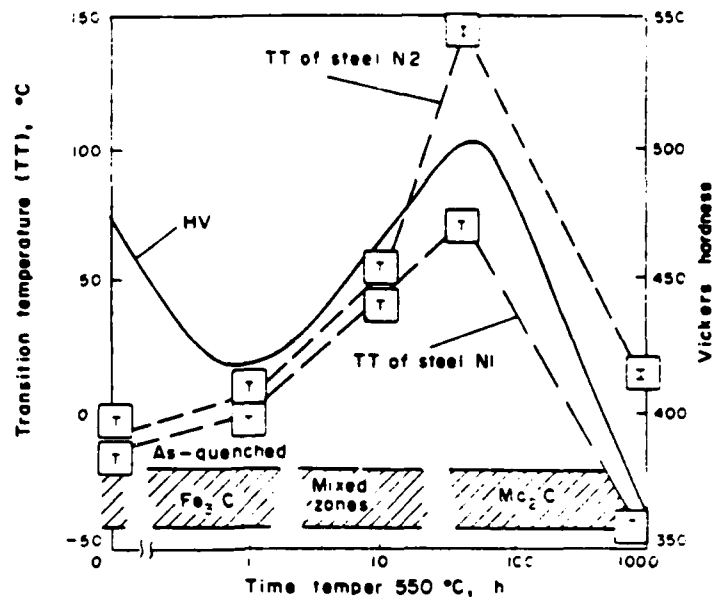
Figure 5-40: Development of temper embrittlement in P doped. Mo steel showing association of transition temperature, aging response and carbide planes. Ustinovshichikov[83]

interpretation is that the Ti transition at 386 eV may easily be obscurred by a nitrogen transition at 381 eV although the presence of an additional peak at 417 eV is strong suggestive evidence for Ti, as shown in the spectra of Figure 5-43. However, these characteristic Ti peaks were not found on all facets examined so a more conclusive answer is not possible.

The longitudinal data are once again contradicted by the transverse hydrogen charged ductility values in this brittle regime. Whereas the 700°C aged longitudinal tests continued to display intergranular fracture, the transverse test at this condition now somewhat surprisingly showed no effect whatsoever (through %RA) of hydrogen, as seen by comparison of Fig. 5-29 and 5-36. Since the longitudinal specimen does display intergranular fracture, it is felt that the high degree of plasticity developed in the transverse test at this condition is caused primarily by a drop in strength level.

The propensity for intergranular failure at these higher temperature aging conditions, as opposed to quasicleavage or MVC, as summarized in Fig. 5-42, indicates that by
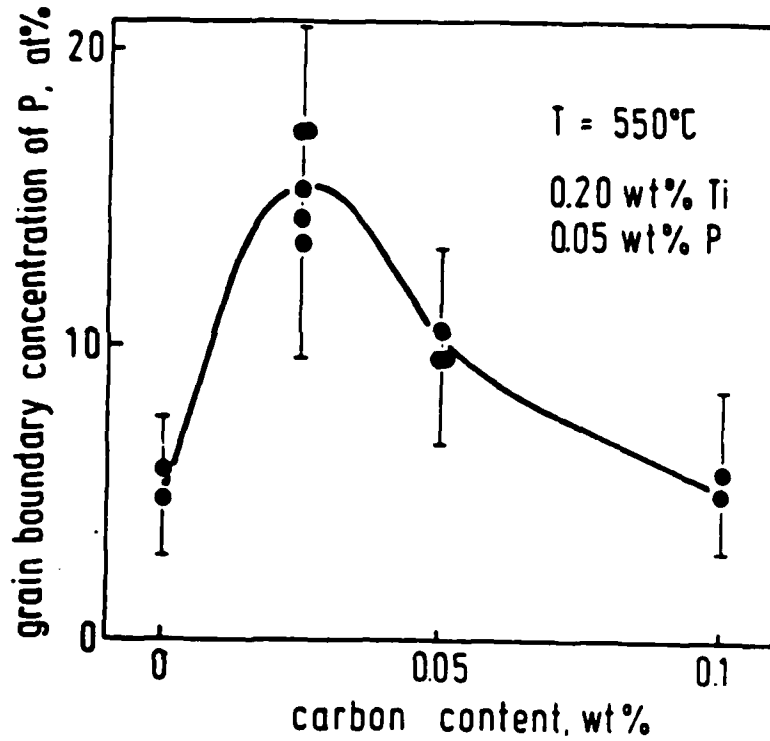
Figure 5-41: Dependence of P-coverage at grain boundaries on C content of Ti-Fe alloy. Note initial rise with small C additions. Erhart et.al.[42]
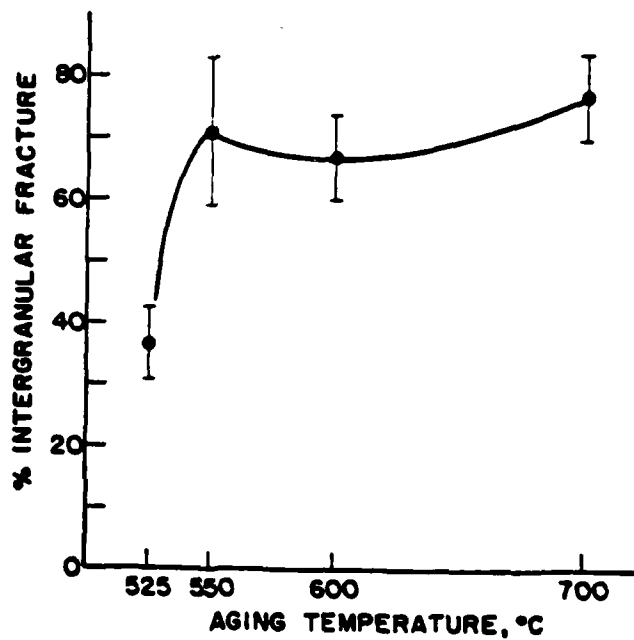
Figure 5-42: Development of intergranular fracture in charged tensiles as a function of aging temperature

550°C, the frequency of occurrence for this fracture mode is established and is relatively

Table 5-7: Summary of calculated P and S concentrations measured at prior austenite boundaries

Heat Treatment	$A_p/A_{Fe_{703}}$	$A_s/A_{Fe_{703}}$	%P at%	%S at%
550/1HR	0.0379	0.0303	1.4	0.8
	0.044	0.0503	1.6	1.2
			$\bar{C} = \overline{1.5\%P}$	$\overline{1.0\%S}$
600/HR	0.0462	0.0925	1.7	2.3
	0.0723	0.0395	2.6	0.9
	0.074	0.0855	2.7	2.1
			$\bar{C} = \overline{2.3\%P}$	$\overline{1.8\%S}$
	0.04	-	1.3	-
	0.03	-	1.1	-
	0.04	-	1.3	-
	0.02	-	0.7	-
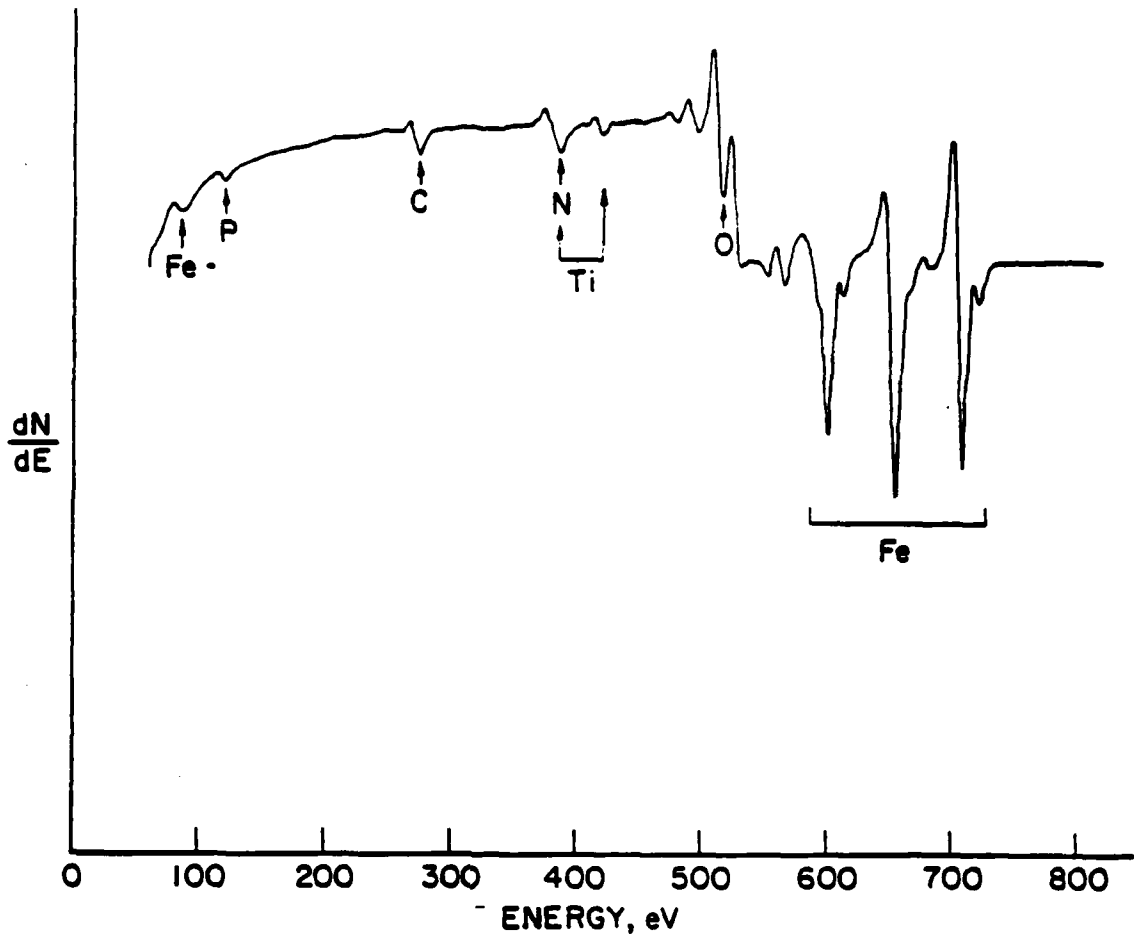
Figure 5-43: Auger electron spectrum taken from fracture facets on 600°C/1hr aged specimen showing overlap of N and Ti transitions.

constant up to 700°C. This is surprising since metalloid related embrittlement in steels has been shown to be diminished at temperatures higher than 600°C[64, 166], presumably due to increased matrix solubility. This persistence for intergranular fracture may stem from two different causes. First, if TiC is an effective trap for P, as suggested by Erhart et. al.[42], the TiC precipitates at these boundaries, still present as a fine distribution, may inhibit movement of P back into solution in the matrix. Additionally, these precipitates will still effectively trap hydrogen at these locations; both of these possible actions could retain H and P at the boundary.

In summary, the tests for the effect of H on tensile ductility in this alloy system have led to several conclusions.

1. Hydrogen can alter the form of ductile fracture from normal microvoid coalescence to a mode best described by the Thompson and Chesnutt[136] definition of tearing topography surface and consistent with hydrogen related fracture surfaces observed by previous researchers and similar to a glide plane decohesion mechanism of separation.

2. The centering of this fracture mode about inclusions indicates that hydrogen is attracted to these sites, most probably due to the localized stress enhancement about these sites and possibly through plastic flow (dislocation transport).

3. Small segregations of metalloid elements (i.e. P or S) to high energy (prior γ) boundaries can apparently induce brittle fracture along these boundaries when accompanied by and associated with internal hydrogen.

4. The strong coincidence of brittle fracture with the onset of secondary hardening (i.e. alloy carbide precipitation) implies that a strong interaction of Ti with P occurs in this steel or alternatively that the strong trapping of hydrogen at TiC precipitates on prior γ boundaries exceeds the critical concentration for cracking at these sites.

5.4. Hydrogen Induced Cracking (HIC)

In general, the results of internal hydrogen induced cracking in this alloy reflect the relatively high ductility of this alloy class in comparison with other alloys previously studied using this technique. For these tests, the only specimens studied were the as-quenched and 400, 500, 600°C/1 hr. aged treatments, as it will be recalled that the longitudinal σ_{ys} levels of these microstructures were equivalent. An additional specimen aged at 700°C/1 hr. was also tested, but sustained load/displacement cracking could not be induced.

In brief, the key results of these tests were:

1. The lowest threshold observed, for these particular hydrogen charged conditions, was for the 400°C/1 hr. aged specimen at 38 MPa(m)$^{1/2}$. The as-quenched, 500°C/1 hr. and 600°C/1 hr. conditions produced K_{Ith} levels of approximately 60 MPa(m)$^{1/2}$.

2. Critical fracture for the as-quenched, 400°C/1 hr. and 500°C/1 hr. aging conditions occurred at stress intensity levels between 100 and 110 MPa(m)$^{1/2}$; the 600°C/1 hr. treatment failed by fast fracture at a stress intensity level of 85 MPa(m)$^{1/2}$.

3. Although a distinct threshold level was found for all tests, little K-independent Stage II cracking was established in any of these studies. Instead, a regime consisting of highly erratic crack growth was observed, similar in its graphical features to that observed by Gerberich and co-workers[102].

Starting first with the results for the 600°C/1 hr. aged specimen, as shown in Fig. 5-44, it was observed that this microstructure possessed less intrinsic toughness than the other treatments studied. This is not unreasonable in light of the Auger electron spectroscopy which indicated an enhanced metalloid segregation to prior γ boundaries in this aging condition. Lower fracture toughness is a common characteristic indicator of the onset of temper embrittlement in steels. In the near-threshold region, the crack growth rate rose very sharply with stress intensity and a crack velocity exceeding 10^{-5} m/sec was attained. This should be compared to the lower velocities measured in this regime for the other microstructures. Crack growth abruptly dropped off at this point and only briefly sustained crack growth rates of near 10^{-6} m/sec before overload failure.

The most unexpected result from testing of this microstructure was the relatively high threshold K value of just over 60 $MPa(m)^{1/2}$ exhibited. It has been observed in previous work that temper embrittled microstructures usually exhibit lower thresholds for environmental cracking than non-embrittled ones. This is understandable from the standpoint of the conventional "mechanism" for hydrogen induced cracking; i.e. cracking will occur upon attainment of a critical stress/hydrogen concentration combination. The greater degree of irreversible trapping in this microstructure may have precluded the attainment of hyrogen concentrations sufficient to cause even low energy intergranular fracture. This possibility will be considered further in the discussion chapter.

Examination of the fracture surfaces from this specimen revealed that cracking was predominantly intergranular, as was observed in the charged tensile tests. This can easily be seen in Fig. 5-45, which shows the intergranular facets adjacent to the fatigue pre-crack from the threshold cracking region. Many secondary cracks were also observed on the fracture surface. Examination of sectioned surfaces normal to the main crack plane revealed isolated cracks below it. When etched, these cracks can be seen to be propagating along lath packet or high angle boundaries (Fig. 5-46).

In contrast with the above stated results, the results from the 500°C/1 hr. aged

Figure 5-44: Internal Hydrogen Induced Cracking in 600°C/1hr aged microstructure.
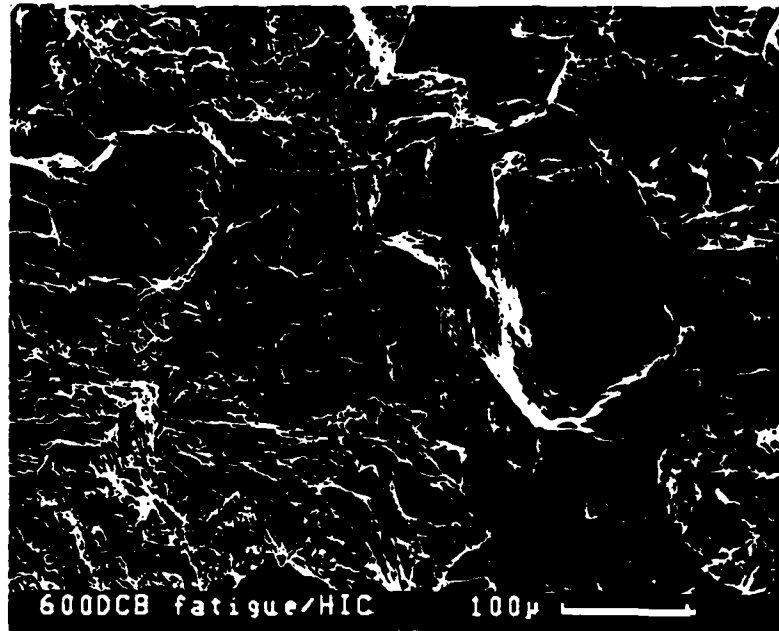
Figure 5-45: SEM micrograph of 600°C/1hr aged DCB specimen showing threshold cracking region.
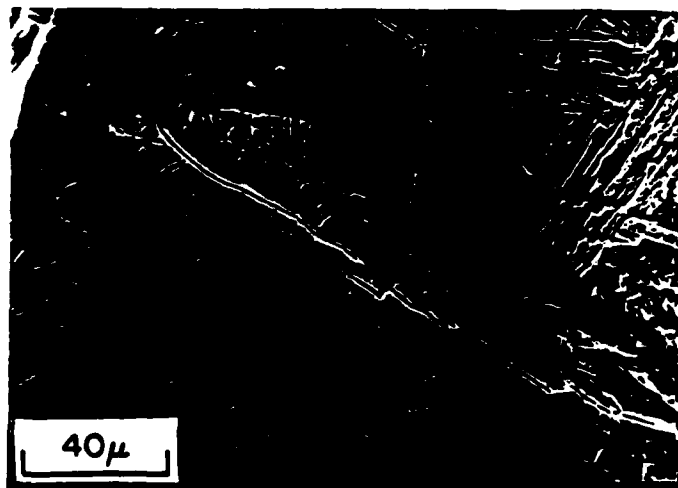
Figure 5-46: SEM plateau etched micrograph showing sub-surface boundary path cracking from 600°C/1hr aged DCB specimen.

specimen are indicative of a high toughness ($K_Q \sim 100$ MPa(m)$^{1/2}$) although the threshold stress intensity was virtually the same as the 600°C aged specimen at ~ 60 MPa(m)$^{1/2}$.

as shown in Fig. 5-47. Irregular crack growth commenced at stress intensities near 70 MPa(m)$^{1/2}$ and crack growth rates just above 10^{-6} m/sec. At increasing stress intensities up to failure, mean crack growth rates vacillated quite rapidly between high and low propagation rates.

This increased resistance to cracking was evident from the fractographic examination of this specimen, which displayed generally transgranular cracking and tearing on a fine scale. Figure 5-48 shows the cracking developed just beyond the fatigue pre-crack in the threshold region: fracture is certainly quite ductile here, in comparison to that seen in Fig. 5-45 from the 600°C aged condition. In addition, a number of "secondary" cracking features can be identified from this figure. These features resemble "yawned" transgranular cracks found by Bernstein[47] in cathodically charged iron. The nucleation sites for these cracks and the reason for their blunted appearance could not be ascertained from these studies, although more will be said about them later in this section.

Curiously, the as-quenched microstructure specimen displayed cracking behavior (Figure 5-49) quite similar to that found for the 500°C aging. The threshold in this case was 59 MPa(m)$^{1/2}$ and fast fracture (K_Q) occurred at a stress intensity of 110 MPa(m)$^{1/2}$. Once again, hydrogen induced cracking above the threshold stress intensity consisted of periods of growth followed by inactivity (incubation) which were again followed by growth. It appears that the erratic nature of this cracking may have been less than that observed for the 500°C aged specimen as growth periods in this case were less frequently interrupted and for shorter time periods.

The fracture surface of the as-quenched specimen was similar to that of the 500°C aged specimen in that cracking was predominantly transgranular, consisting of quasi-cleavage and ductile tearing, as seen in Fig. 5-50. Deeper secondary cracks, similar to those seen in the 500°C aged specimen were also present for this case, although the frequency of observation was somewhat less for this case at the higher crack velocities (near failure). The fracture mode observed resembled classical quasi-cleavage more so
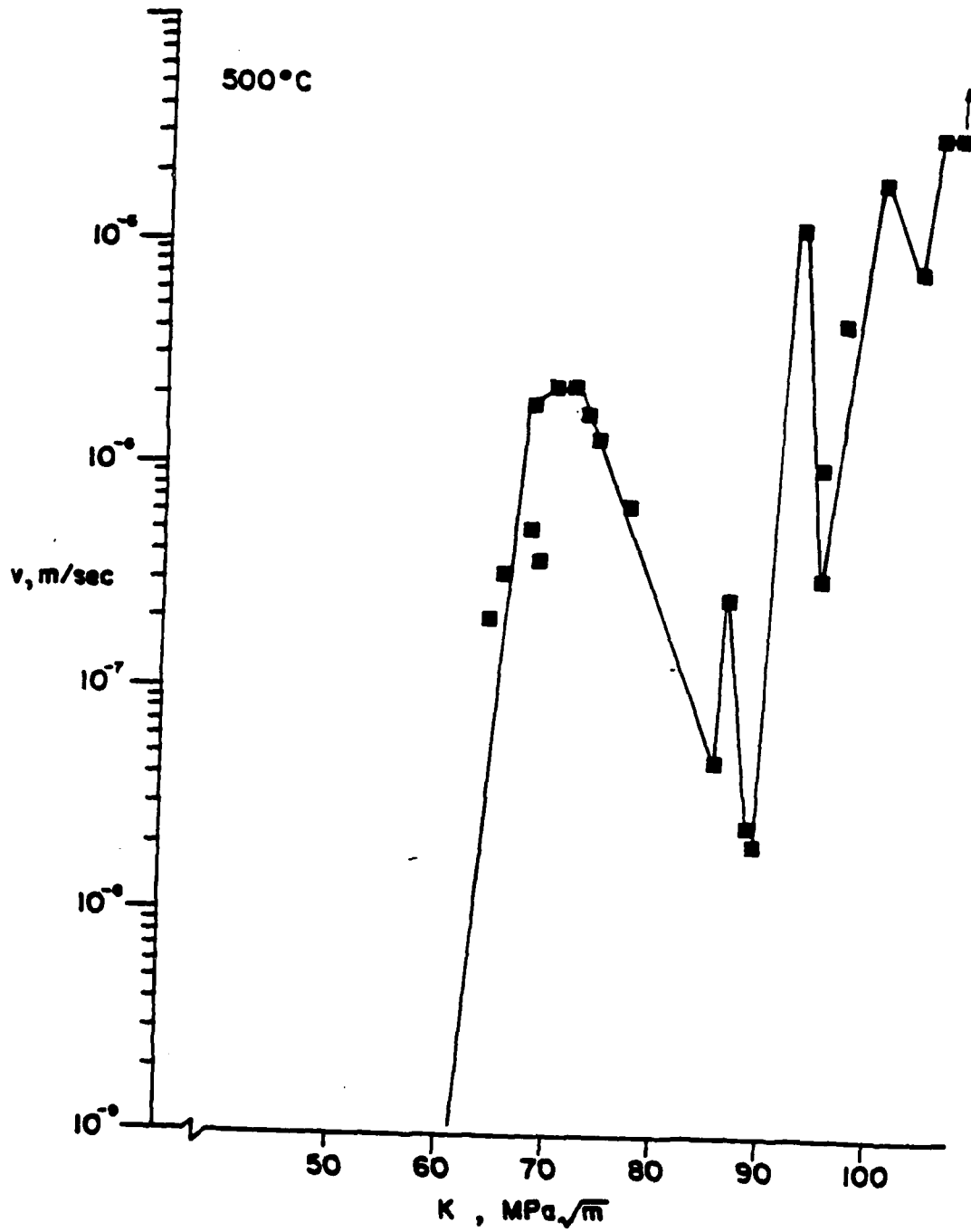
Figure 5-47: Internal Hydrogen Induced Cracking in 500°C/1hr aged microstructure.
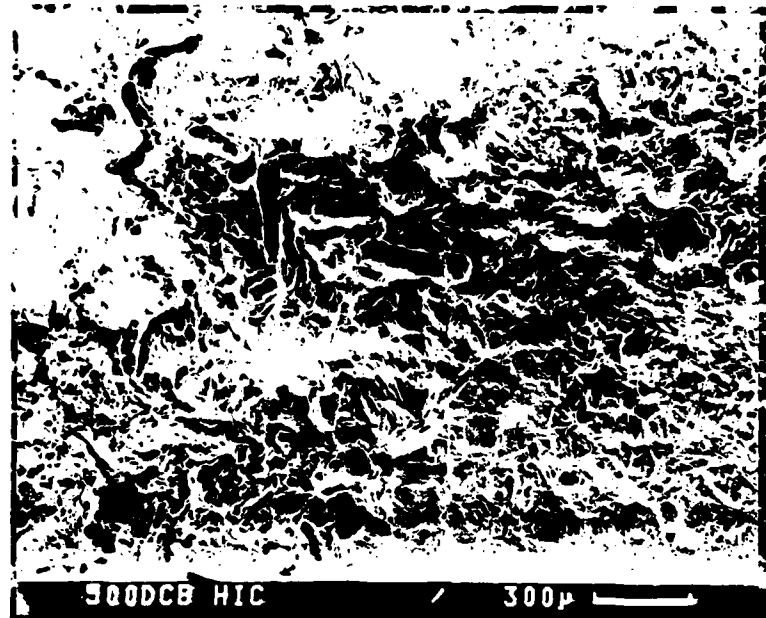
Figure 5-48: SEM micrograph showing near threshold crack surface in 500°C/1hr aged DCB specimen

than observed in any of the other specimens. This may indicate that the failure mode was more purely mechanically determined as opposed to one based predominantly on hydrogen/microstructure interactions.

The 400°C aging treatment yielded hydrogen induced cracking properties as shown in Figure 5-51. The most notable difference found here was that cracking continued down to a threshold stress intensity of 36 MPa(m)$^{1/2}$. Between 40 and 60 MPa(m)$^{1/2}$, a reasonably K- independent Stage II type cracking did occur at a crack growth rate of 3 x 10^{-7} m/sec. Analysis of the load cell/clip gage signal records indicated that the increments of crack growth, Δa, in this regime were also remarkably constant at ~1000 μm. The fracture mode in this regime, as shown in Figure 5-52, was essentially quasi-cleavage. Inclusions were occasionally identified at the source of these facets.

At 60 MPa(m)$^{1/2}$, crack growth once again, became highly irregular and a notable decrease in crack growth rate was found as observed in the 500°C aged and as-quenched
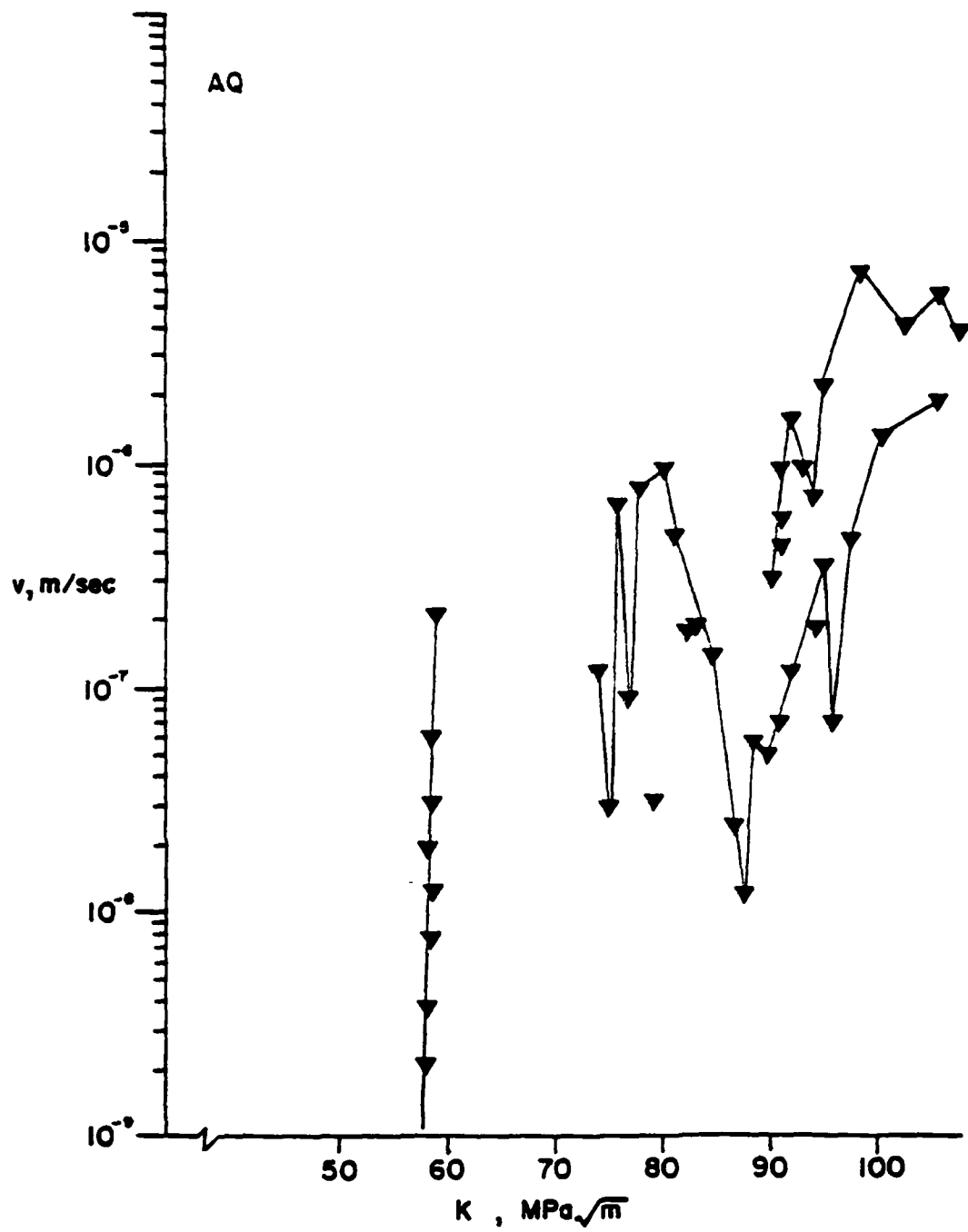
Figure 5-49: Internal Hydrogen Induced Cracking in as-quenched from 1200°C microstructure
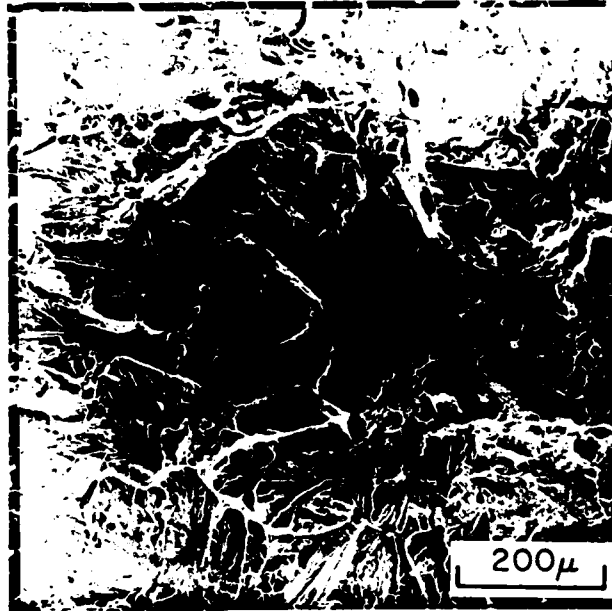
Figure 5-50: SEM micrograph of typical cracking mode from as-quenched DCB specimen

specimens. The cracking mode here was now quite similar to the ductile tearing mentioned previously, but now the occurrence of blunt secondary cracks was quite prevalent, as seen in Figure 5-53. Normal sections through the fracture surface revealed features within these "cracks" which had the appearance of slip markings, as shown in Figure 5-54. Note the presence of minor cracks adjacent to the larger one which apparently are not linked to the main crack. These cracks were found to follow the underlying lath structure. This cracking process was terminated by fast fracture at a stress intensity level of 100 MPa(m)$^{1/2}$.

The appearance of these secondary yawned cracks may be related to the cementite structure developed during the various aging treatments employed. These cracks were most prominent in the 400°C aged microstructure, followed by the 500°C aging and finally by the as-quenched microstructure. It may be recalled that the 400°C aging produced the largest density of cementite clusters at ferrite lath boundaries. The 500°C aging did cause some fine cementite precipitation, but this reaction was apparently hindered by TiC clustering and the occurrence of cementite was thus diminished. The as-quenched
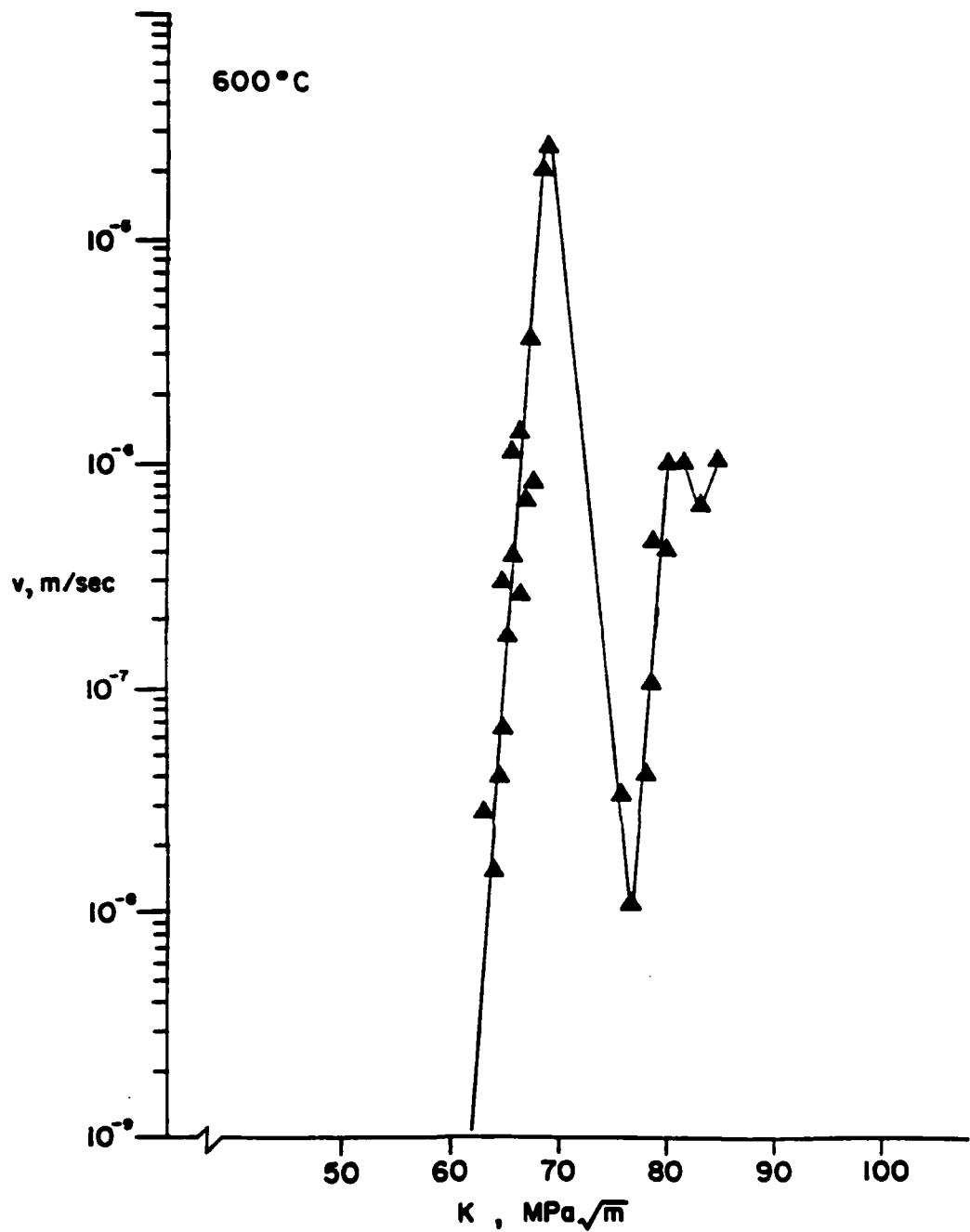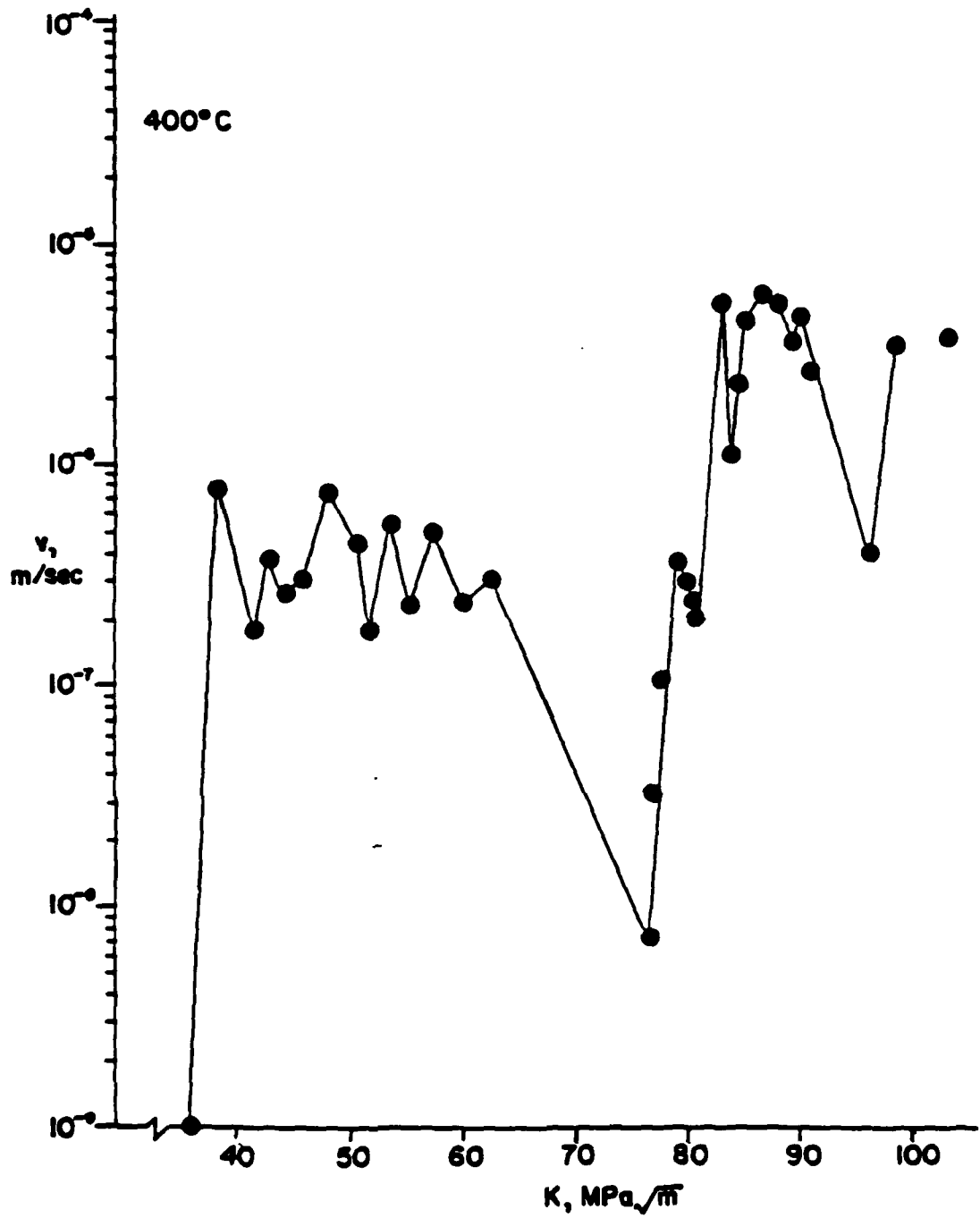
Figure 5-51: Internal Hydrogen Induced Cracking in 400°C/1hr aged microstructure
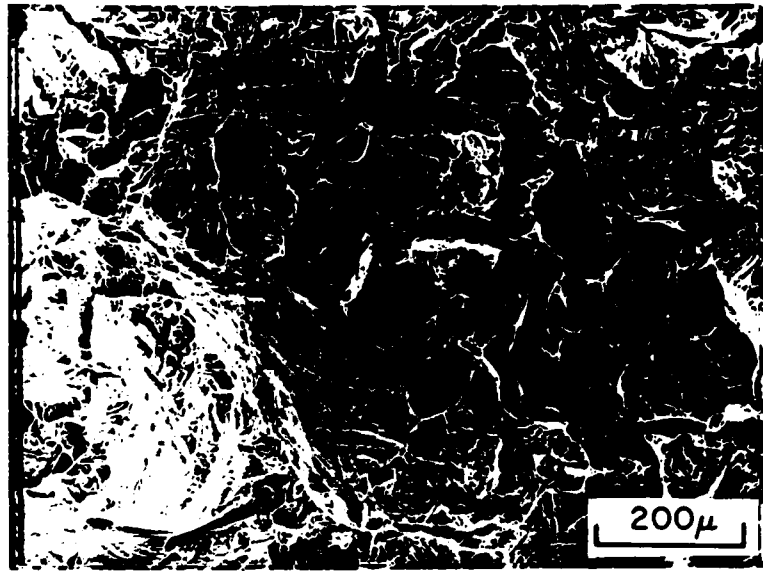
Figure 5-52: SEM micrograph of fracture surface of 400°C/1hr aged DCB. K~ 46 MPa(m)$^{1/2}$
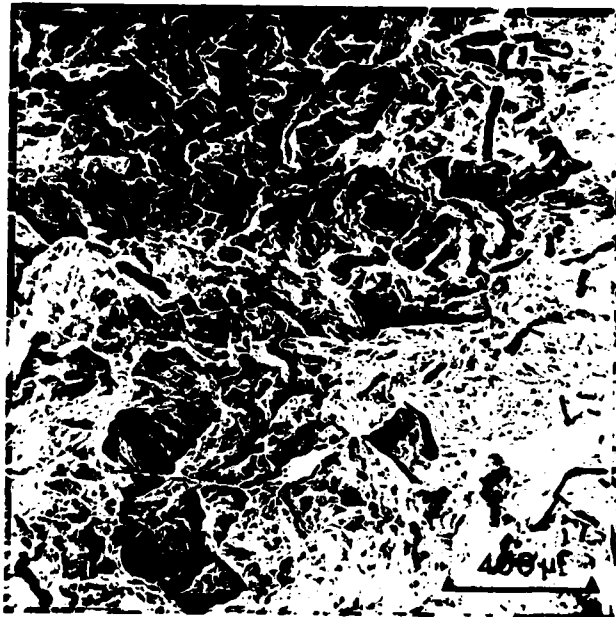
Figure 5-53: SEM micrograph of fracture surface of 400°C/1hr aged DCB specimen. K~ 65 MPa(m)$^{1/2}$

microstructure essentially by-passed precipitation of all carbide phases; isolated cementite laths were irregularly found in this microstructure. The coincidence of this fracture morphology with the cementite phase suggests that cracking in advance of the main crack
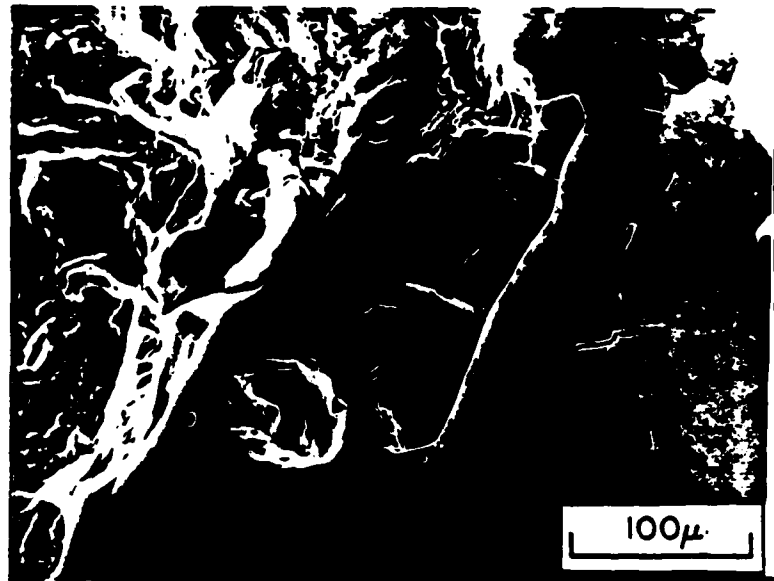
a
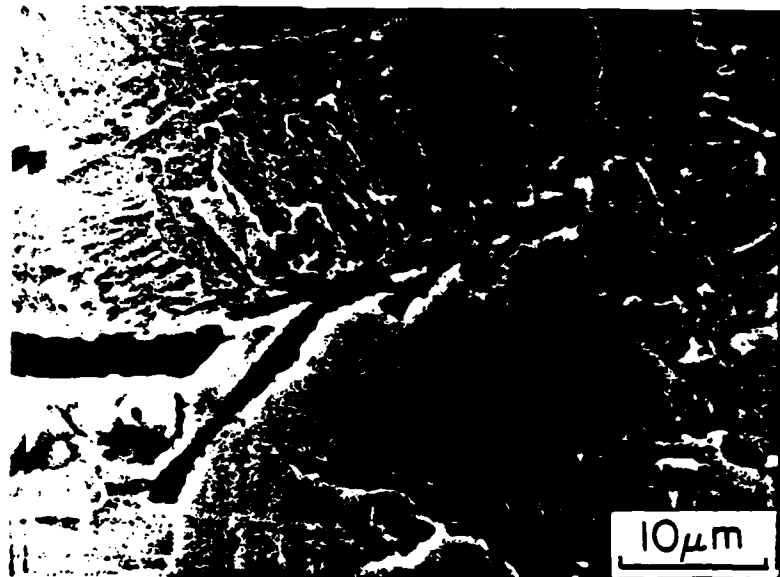
b

Figure 5-54: SEM Plateau etched micrograph showing sub-surface crack structure from 400°C/1hr aged DCB specimen a.) slip markings within blunt secondary crack b.) high magnification showing minor crack orientation relative to underlying microstructure

may be nucleated at these particles. The common stress intensity (60-70 MPa(m)$^{1/2}$) for appearance of this process may similarly indicate the common stress/hydrogen concentration required for cracking initiated at these sites.

To summarize, hydrogen induced cracking in this alloy was found to be dependent on microstructure at equivalent strength levels. When aged at 600°C, so that fine TiC precipitation took place, the alloy was found to have the lowest apparent toughness and HIC occurred predominantly along prior austenite boundaries. This microstructure also exhibited the highest subcritical cracking rate ($>10^{-5}$ m/sec). At lower aging temperatures, as found for the charged tensile experiments, cracking proceeded by a more ductile transgranular fracture mode. As stress intensities between 60-70 MPa(m)$^{1/2}$, blunted secondary cracks appeared on the fracture surface; the incidence of this type of cracking increased in the order 400°C, 500°C and as-quenched. This is also the order of increasing frequency of cementite appearence in this alloy. Only in the 400°C aged microstructure was cracking observed below K levels of 60 MPa(m)$^{1/2}$. In this case, the fracture mode appeared to be that of quasi-cleavage, and larger inclusions appeared to play a significant role in the initiation of quasi-cleavage facets.

Some general observations concerning the tests should be noted. The load cell/clip gage signal test records for there studies indicated that cracking occurred by discrete jumps of the main crack front suggesting, as has been done previously, that cracking is a discontinuous process. An additional feature which was common to virtually all of there tests was crack branching and breakage of the specimen "arm" during testing. It is the author's opinion that this phenomenon was largely attributable to specimen geometry, specifically arm height and side groove depth. As the crack continued to grow, more bending of the arms occurred until the grossly altered specimen deflection produced more severe stresses (normal and shear) across the arm height than at the crack tip region. This problem was probably exacerbated by the unusually high stress intensities necessary to produce hydrogen induced cracking in the first place.

Chapter 6
Discussion of Results

6.1. Hydrogen Trapping

The results of the electrochemical permeation experiments strongly indicate that deep trapping, as indicated by depressed initial transient diffusivity values, is associated with aging reactions which occur at temperatures $>500°C$. From the results of the microstructural characterization section, it is apparent that the predominant reaction in this temperature range is the direct heterogeneous precipitation of TiC phase. That deep trapping is associated with the presence of significant amounts of this phase is in direct agreement with earlier work[34,36,51] primarily that of Pressouyre[28].

Comparable results have been reported recently by Takahashi[51] and co-workers where hydrogen diffusivity values were measured using the same technique employed in this thesis. Using quench and temper treatments on 0.05%C-0.02% Ti steels, these authors ♦ reported virtually identical diffusivity values for hydrogen in the as-quenched condition and for 1 hr aging times at 300, 400 and 500°C (Fig. 6-1). The D value in all these conditions was approximately 5×10^{-6} cm^2/sec. In the 1 hr at 600°C condition, the diffusivity value dropped to 1×10^{-7} cm^2/sec; a one and a half order of magnitude drop. It was also found that the diffusivity values increased steadily on aging at progressively higher temperatures. At temperatures of 900-1000°C, the diffusivity values once again attained a mean value of $5 \times 10^{-6} cm^2/sec$.

These authors attributed the low diffusivity at 600°-700°C to Ti precipitation by direct observation of Ashby-Brown type contrast about fine "coherent" TiC precipitates in these microstructures. At 700°C, the mean particle diameter was 100Å. Additionally,
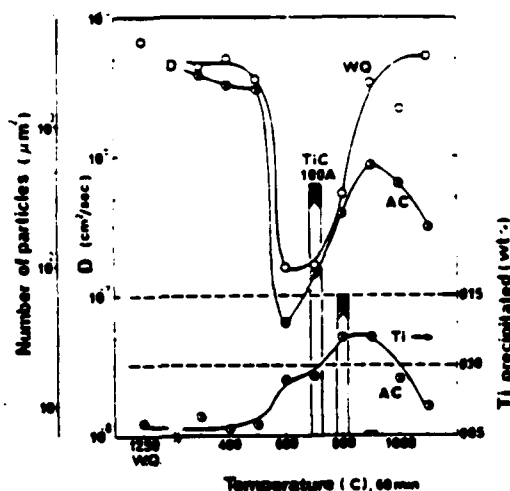
Figure 6-1: Time-lag diffusivity and precipitate data of Takahashi et.al.[51] showing steep diffusivity drop after 600°C aging

electrical resistivity measurements showed a marked drop at 600°C which was associated with Ti precipitation. The diminished trapping at higher aging temperatures (>700°C) was associated with the loss of coherency rather than coarsening of the TiC phase. Additionally, it was concluded that coherent TiC particles were more effective traps than either Ti substitutional atoms or incoherent TiC particles and that static hydrogen induced cracking in this steel was diminished in microstructures possessing lower D values. The evidence for the trapping conclusion was minimal however, and no cracking data or details were given.

These findings are consistent with those of Pressouyre[28], who concluded that Ti precipitates were strong traps by comparison of first and successive diffusion transients through microstructures containing these particles, as described previously. He analyzed the TiC precipitate distribution in his Fe-Ti-C alloys, and the smallest reported size was 400Å[29]. In light of the microstructural and trapping characterization of this and Takahashi's study, it must be questioned whether TiC particles exceeding 400Å were predominantly responsible for deep trapping. Similarly, the exact cause of deep trapping at TiC interfaces must also be re-examined.

Additional evidence for the strong trapping capability of TiC on diffusing H in

a-Fe has been provided by Iino[36] on Ti bearing steels, using electrochemical permeation and thermal desorption techniques. He observed intermediate plateaus on flux-time curves which could be predicted using the McNabb-Foster formalism, by allowing for greatly diminished release rates and low coverage ($C_o/N_i \ll 1$) of the trapping population. Iino found that the persistence of these plateaus increased with increasing Ti content; this was explainable in terms of an overall reduced concentration of diffusing H in the matrix and a greater quantity of deep trapping sites. Additional thermal degassing experiments indicated that a peak hydrogen evolution occurred between 500-$550\,^\circ C$ and that the height of this peak increased with increasing Ti concentration. It was concluded that the high temperature peak was associated with "deep" traps and the correspondence with Ti content allowed for the conclusion that TiC precipitates were the responsible microstructural trapping site. The appearance of transient plateaus in the present study supports Iino's explanation and model, from which additional information may also be derived. Although Iino did not report microstructural characterization results or heat treatments for his material, one must assume that they were aged in such a way that all the Ti was precipitated as carbides; hence, the strong observed trapping.

In the previously mentioned study of Brass[17a], hydrogen permeation and trapping were studied in both 35 CD4 (AISI 4137) and 42 CD4 (AISI 4140) low alloy steels. Here too, intermediate plateaus were observed but only during the first polarization and only for microstructures aged above $300\,^\circ C$. This may indicate a similar trapping behavior trend as observed in the present study, since it may be recalled that intermediate plateaus were found during initial polarizaion for all but the as-quenched microstructure. Brass, however, did not observe this behavior for second polarizations; such results were only found in the present study for the $600\,^\circ C$ aged microstructure.

In the present study, the trend in plateau occurrence directly paralleled the progression of carbide precipitation in the lath ferrite matrix. In the as-quenched microstructure, the flux curves (Fig. 5-21) displayed a form predicted for weak, reversible trapping only. Plateaus were observed in microstructures (Figs. 5-23 and 5-24)

possessing somewhat stronger trapping than observed in the as-quenched structure, i.e. dislocations, grain boundaries and Ti substitutional atoms. It is postulated that these intermediate (but still reversible) strength traps were Fe_3C carbides, as concluded from the lower aging temperatures (400°C and 500°C) and TiC precipitates sized above some critical dimension, as shown by the development of second polarization plateaus in the 700°C (Fig. 5-27) and 900°C (Fig. 5-28) microstructures, and the absence of this plateau in the 600°C second polarization.(Fig. 5-26)

In the 400°C age treatment, where cementite precipitation was well advanced, the intermediate plateau was observed. This may be accounted for by the stronger trapping exhibited by the cementite phase, as predicted by Asaoka[34]. Since no TiC phase was detected in this microstructure, it must be assumed that Fe_3C is responsible. It should be noted that, although the transient plateau indicated delayed release of trapped hydrogen, the traps responsible in this case are *not* irreversible. This can be determined by noting the close correspondence of the second polarization flux with the first. This indicates that the same density of traps has participated in the second polarization as did in the first polarization; therefore, little hydrogen -was irreversibly trapped.

This same reasoning applies to the flux data for the 500°C age microstructure, although the order of magnitude drop in diffusivity compared to the as-quenched microstructure clearly indicates that the nature of the traps has changed during this treatment.

Here again, the microstructures were found to contain cementite and TiC clusters were also detected. Since the first and second transients for this microstructure were virtually identical it may again, and in the case of the 400°C aged microstructure, be concluded that bulk trapping is reversible and any additional role of the TiC phase cannot be definitely determined. The dramatic drop in diffusivity at 600°C, as observed by Takahashi[51], undoubtedly is associated with TiC precipitation. From examination of the flux time curve, one may see a persistent intermediate plateau which indicates stronger

trapping than in either the 400 or 500°C conditions. As might be expected, the second polarization flux does not develop a transient plateau. It is noteworthy here that the observed TiC precipitation was generally sized *below* the supposed semicoherent - incoherent transition diameter of ~200Å, as postulated by Youle.[16] If coherency strains are important to the irreversible trapping of this phase, then this precipitate population would be expected to exhibit only irreversible trapping. The lack of an observable plateau on the second polarization transient may be taken as evidence that little intermediate strength reversible trapping capability is associated with this precipitate size range.

Considering the observed flux transient results for the 700°C aged microstructure test (Fig. 5-27), the second polarization transient now exhibits an intermediate plateau. Except for the partial recrystallization of this microstructure (which would diminish reversible trapping), the primary distinction with the 600°C aged structure is the coarsening of a fraction of the TiC particles above the 200Å range. As stated before, the implication is that these precipitates now behave as intermediate strength, reversible traps. Since many particles are sufficiently small, irreversible trapping still occurs.

Finally, after 900°C aging, a sufficient portion of the precipitates has coarsened to an incoherent size range such that little irreversible trapping occurs. The existence of plateaus on both transients confirms, however, that these precipitates give rise to delayed release of trapped hydrogen from their interfaces.

It is difficult to substantiate the role of precipitate coherency effects on trapping without direct observation and analysis. Due to the small size range in which TiC loses its registry with the matrix, TEM examination in this study failed to provide useful information. Takahashi[51] reported that coherency strain fields were detected about small TiC precipitates in the 700°C aged condition in the form of Ashby-Brown type contrast. Evidence of this form was not possible in the present study, possibly due to interfering strain effects from the high dislocation density or quenched in stresses.

The breakthrough diffusivities (Fig. 5-29) determined from the electrochemical

permeation experiments are suggestive of a fast-path diffusion mechanism through these microstructures, as determined from their larger magnitude in comparison to the time-lag D values (Fig. 5-22). As stated in the last chapter, the coincidence of the first and second polarization values indicates that this method does not provide a sensitive measure of trap strength, but the variation of diffusivity with aging treatment does suggest that the microstructure can affect these supposed short-circuit paths. The features to note from the breakthrough D values are the apparently high D values in the $400\,^{\circ}C$ and $900\,^{\circ}C$ aged conditions as compared to the $600\,^{\circ}C$ and $700\,^{\circ}C$ aged specimens. Microstructurally, the former two structures correspond to coarse cementite cluster formation and coarsened TiC precipitation, respectively. In contrast, the latter microstructures consist of the finest TiC precipitation and strongest trapping. The presence of fine, homogeneous strong traps may perhaps delay H permeation whereas a low density, heterogeneous trap density is less efficient in this way. The recrystallized structure at $900\,^{\circ}C$ may obscure this analogy somewhat, but this certainly appears to be the case for the $400\,^{\circ}C$ aging.

To summarize the preceding discussion, it appears that trapping in relatively simple alloy systems may be more complex than previously imagined. It has once again been demonstrated that precipitates associated with Ti can be strong traps for hydrogen as indicated by the form of the transient hydrogen fluxes through these microstructures, as well as by comparison of time-lag diffusivity values. Apparently, when these particles coarsen above a critical size and/or coherency range, the nature of trapping about them is altered and they become more reversible traps with relatively high λ/μ values, in analogy with the model of Iino[36]. This apparently also applies to Fe_3C which precipitates at relatively low ($< 500^{\circ}$) temperatures. The nature of trapping (reversible or irreversible) in these microstructures can be ascertained from time-lag analysis and this is supported by the similarity in the diffusivity trends between this and Takahashi's[51] work. Conversely, breakthrough diffusivities may only indirectly indicate the nature of trapping as successive transients produce identical diffusivity values. The values of these diffusivities may nonetheless be important for a predictive capability in evaluating a particular microstructure's susceptibility to internal hydrogen. In contrast to the time-lag methods,

which determines the diffusivity through an integration of the flux, the breakthrough time can more easily be understood as a more direct measure of the ease of hydrogen transport through the microstructure. In a microstructure where only slight supersaturation levels are required at failure initiation sites or mean diffusion distances are relatively small, it is possible that the degree of embrittlement may scale better with the breakthrough, rather than time-lag diffusivity. In the following sections, where the degree of embrittlement of this alloy is considered, these different methods of interpreting hydrogen permeability should be kept in mind. For the tensile test, time is particularly important since diffusion will be greatly confined. Plasticity effects (dislocation transport) on hydrogen transport must also be considered. For the long-term hydrogen induced cracking studies, larger scale diffusion of hydrogen should certainly play a more important role, especially since deformation and failure are not externally induced in this case, i.e. hydrogen must contribute more to the fracture mechanism. The supply of hydrogen from the remote matrix regions to the crack tip may also be important in this case.

6.2. Tensile Properties

The results of the uniaxial tension tests indicate the complexity of the interaction of internal hydrogen with a ferritic steel microstructure. It is felt, however, that the results are consistent with the trap theory of hydrogen embrittlement (TTHE) developed by Pressouyre and Bernstein[32] and also with more recent theories of temper embrittlement involving alloy element-metalloid interactions[42,79,83,165].

In brief, the trap theory of hydrogen embrittlement models various situations through which the trap population in a microstructure may modify the extent and nature of hydrogen embrittlement. Important parameters include:

1. Hydrogen transport mechanisms (dislocation atmospheres, interstitial diffusion or high diffusivity paths)

2. Location of hydrogen prior to test (internal or external)

3. Character of traps present in microstructure.

The premise of this theory is that specific sites within a ferritic microstructure which will act as premature fracture nuclei are themselves irreversible traps and embrittlement will ensue when a sufficient concentration of hydrogen and stress state level exist at the most detrimental of the possible trap sites.

Pressouyre developed his model specifically for the Fe-Ti-C system. Three specific traps were considered as important in controlling the hydrogen distribution but in the broadest general sense, all sites are accounted for. TiC particles were considered the dominant irreversible traps, while Ti substitutional atoms and dislocations were considered as reversible traps. An important assumption was that dislocations were mobile carriers of hydrogen which would effectively redistribute reversibly trapped hydrogen at stationary sites to stronger irreversible sites such as TiC particles, inclusions and high angle grain boundaries.

For the case of internal hydrogen, which is experimentally represented by a pre-charged and plated material, the total hydrogen content is fixed. The redistribution of hydrogen to irreversible sites during plastic deformation is related to the strain rate by:

$$\dot{C}_H^i(t) = k(\dot{\epsilon}/b)(D_i/l_i^2)(C_H^i(t) + t\dot{C}_H^i(t)) \qquad (6.1)$$

where $C_H^i(t)$ = time dependent concentration of hydrogen at irreversible traps (single population assumed)

k = a constant

$\dot{\epsilon}$ = strain rate

b = Burgers vector

D_i = influence range of irreversible types

l_i = mean distance between traps

$C_{\bar{H}}(t)$ = concentration of hydrogen at dislocations.

Through the use of the model of Tien et al.[58] for hydrogen transport by dislocations and substitution, Pressouyre finally arrives at the following two equations:

$$n = n_o + \frac{D\left(\sum K_r + 1\right)C}{\left(\sum D N^{a}\right)N}$$

and (6.2)

$$r = \frac{C - C}{\left[D N C - \dfrac{\left(\sum D\right)}{\left(\sum K_r + 1\right)}(C - C)\right]N(\epsilon \, b)}$$

where: (6.3)

n_f' = final quantity of hydrogen collected at each irreversible traps.

K_r = exchange "rate" constant of hydrogen from fixed weak traps to dislocations.

N_i = density of irreversible traps

t_c' = initial hydrogen concentration at deep traps.

C_o^i = initial hydrogen at deep traps.

From a practical standpoint, the final quantity of hydrogen associated with the deep traps must not exceed a critical value:

$$n_f' < n_c' \qquad (6.4)$$

or the time for this accumulation to occur must be sufficiently long in comparison to the test time.

$$t_c' \gg t_f \qquad (6.5)$$

There are important conditions on these relationships. First, TiC particles will assume different roles depending on their size and distribution. Below a certain size, which will depend on matrix flow stress, initial hydrogen content, temperature, etc., the carbides will essentially be considered only beneficial and never capable of becoming crack nuclei. Above this size, the particles are treated essentially as inclusions, with their

own D_i and 1_i Pressouyre's general formula for N_f^i simply states that the amount of hydrogen associated with *any* irreversible trap may not exceed some critical value. More realistically, this criterion should limit hydrogen only at potentially deleterious irreversible sites (large particles and inclusions) and should also account for the continuous beneficial effects of hydrogen irreversibly trapped at very fine, homogeneously dispersed particles.

The initial trend of the pre-charged tensile tests suggests that such a model may be applicable to the present system. The dominant deleterious traps are, in this case, the larger Ti-based inclusions, which apparently cannot be altered by heat treatment. The beneficial contribution of even embryonic TiC particles is obvious from the increased ductility associated with microstructures where these particles are present (500°C). The lower ductility in specimens aged at 400°C or in the unaged condition is in effect caused by isolated deep trapping at inclusions. Using the nomenclature of the trap theory of hydrogen embrittlement, the increased sensitivity may be rationalized in the following ways. First of all, the value of N_o^i is higher due to a lower overall irreversible trap density; the same probably pertains to C_o. Additionally, the value of N_i will be lowest for these microstructures, enhancing susceptibility. Finally, since a greater concentration of Ti will be contained in solid solution, the term $\sum_r K_r$ will also be greater, producing more sources of hydrogen to mobile dislocations. In this case, the attainment of a critical quantity of hydrogen at strong trap sites is clearly manifested by the radiating TTS fracture mode which surrounds these particles. Although hydrogen has embrittled this microstructure through a change in fracture mode, it is still clear that the trapping capability of these sites, which may have been aided by the localized stress gradient surrounding them, was responsible for the effect.

In certain instances it was quite apparent from the form of the load-time record for the tensile test when the separation of a large facet occurred. In such a case, the load level would turn down sharply with time as if failure were about to occur. Before dropping to zero, the load would then level off and necking strains of a few more per cent would occur before complete separation. This was usually only observed for cases

where one dominating facet appeared on the fracture surface rather than many small ones. Although data for these particular cases were limited, it was noticed that the load/stress (using estimated cross sectional areas) level for separation ranged from 1160 to 1230 MPa before a Bridgman type correction. It is presumptuous to expect more precise information from such an estimate since important factors such as the inclusion shape and size and resulting affects on local deformation and hydrogen enrichment cannot be controlled. It is suggested, however, that the fracture stress for the TTS mode may be determinable under better controlled experimental conditions (i.e. inclusion size, shape and density) or for situations where these parameters can be measured and accounted for.

The upward trend in hydrogen charged ductility, which peaked at the $500\,^{\circ}C$ condition, was most likely caused by enhanced trapping capability due to TiC clustering. TiC trapping is supported both by: 1.) decreased diffusivity and delayed release rate from trap sites and 2.) direct evidence of TiC "clusters" using FIM techniques. The new and surprising implication is that the effective trapping capability of TiC may extend to very fine ($\sim 10\,\text{Å}$) precipitates of this phase, and that an incoherent interface is not essentially necessary. This may be deduced by the lower diffusivities (from breakthrough and time-lag) at $500\,^{\circ}C$ as compared to the unaged and $400\,^{\circ}C$ aged microstructures. The remaining question is whether this capability stems from coherency strain fields or is based on a more chemical interaction.

From the TTHE standpoint, the precipitation of this phase may be beneficial from several standpoints. First, the value of n_o^i corresponding to the larger inclusions may be lower, as well as C_o^i. Most importantly, the value of N_i is effectively increased, causing the amount of hydrogen associated with any particular irreversible trap to be greatly diminished. A less obvious benefit also stems from the K_r terms. Since titanium from solution is consumed in TiC precipitates, the value of C_H^r (t) and hence K_r will be diminished, thereby eliminating sources of H to mobile dislocations.

Since the permeation experiments indicated that deep trapping i.e. complete carbide

precipitation did not occur isochronally until somewhere between 500-600°C, the TTHE would predict that resistance to embrittlement would continue until this phase was excessively coarsened. This would not only diminish the trapping capacity but would also render these carbides as potentially deleterious. The presence of the "hump" in the ductility response is evidence of a change in character of one of the major traps, i.e. grain boundaries. In the simplest sense, the occurrence of grain boundary fracture resulting from the high temperature aging may be interpreted as a change in n_c^i to lower values or, less likely, lowering of the value of t_c^i for these sites. The difficulty arises from the ambiguity described in the results section, namely, it cannot be determined whether the fine precipitation of TiC particles along prior γ boundaries in itself is sufficient to trap a critical concentration of H at these sites and in so doing bring about the intergranular fracture or if the precipitation of TiC phase is accompanied by dissolution of Ti-P clusters or a phosphide phase, thus freeing P to segregate or to assume a different bonding role (Fe-P rather an Ti-P) at the grain boundary region.

The latter rationale is preferred for the following reasons. The previously cited paper by the author[54] reported initial results for tensile tests on this same alloy heat. The findings in that study showed a large improvement in hydrogen charged tensile properties which were not observed in later tests. Additionally, the heat chemistry analyses reported in chapter 4 indicated that a wide variation in S content did occur. In lieu of a more detailed examination of this discrepancy, it must be concluded that variations in heat chemistry originating from the pouring of the ingots are responsible for this change in properties. Hence, the results of the Stevens et al. paper suggest that in a heat of sufficient cleanliness, the presence of a fine distribution of deep trapping sites can ameliorate the effects of internal hydrogen.

The compositional analyses of prior γ boundaries did lead to the conclusion that phosphorus and sulfur were invariably present at these grain facets. The preferential precipitation of TiC at these microstructural sites should be accompanied by a strong Ti signal, as shown in Fig. 5-43. Unfortunately, N and Ti have Auger electron transitions

at nearly equivalent energy levels (381 eV for the N and 386 for Ti) and this tends to obscure interpretation of Ti presence. .—other transition occurs for Ti at 417 eV which more conclusively indicates the presence of this element, but this peak was only irregularly present even for repeated analyses from the same specimen, leaving the question of TiC precipitation effects still unanswered. The quantitative analysis comparison from 550°C/1hr and 600°C/1Hr treatments suggests that a modest enrichment may occur at the higher temperature. The development of intergranular fracture, as shown in Figure 5-42 suggests, however, that the conditions for this fracture mode are essentially constant at temperatures $\geq$ 550°C, implying that further enrichment is not necessary.

An attempt to thermodynamically describe metalloid segregation in ternary systems (Fe–M–I) has been made by Guttman[81] using a regular solution model and it is worth noting the predictions of his model. The extent of segregation was assumed to be predictable from the solubility of the metalloid, I in a-Fe as affected by the interaction coefficient between it and the alloy element. Guttman claims that if this parameter is relatively low (10,000-30,000 cal/mol), then segregation and embrittlement should be enhanced. If this parameter exceeds 50,000cal/mol, then the interaction should be sufficient for precipitation of a second phase (Ti_3P) and embrittlement will be reduced. Finally, after long times at high temperature, the phosphide may be replaced with a carbide phase, freeing P for segregation. Since the interaction between Ti and P is quite strong, this model appears to be consistent with the present study. However, it cannot be tested unambiguously since the almost certain partitioning of P to grain boundaries during austenitization, as has been shown by Schultz and McMahon[166], cannot be accounted for. Segregation in the austenite field is also hinted at by the presence of S in the Auger spectra, an occurrence which is sometimes associated with burning or overheating of steels at high (~ 1200°C) temperatures[24].

An additional difficulty is that this segregation appears to be quite local in nature. If phosphide dissolution followed by phosphorus diffusion to high angle boundaries occurs, it is useful to consider the extent of diffusion possible for P in a-Fe at 600°C. This can be estimated by:

$$x \sim Dt^{1/2}$$

with $D = 7 \times 10^{-13}$ cm^2/sec (6.6)

$\quad$ t = 3600 sec

yielding

$\quad x \sim 0.5 \mu$m

Since the mean austenite grain size was estimated at above 100μm, this precludes large scale diffusion of P unless fast diffusion paths are present.

The likely scenario then is that at low aging temperatures, where TiC precipitation is either impossible at short times or incomplete, the action of P at or near prior γ boundaries is modified by the presence of Ti, either through phosphide phase or metastable Ti-P cluster formation.

When TiC formation occurs, the Ti-P clusters dissolve and P now forms a stronger interaction with adjoing Fe atoms at the boundary. Coupled with H which may be preferentially trapped at high angle boundaries, either an additive or synergistic embrittling effect results.

6.3. Hydrogen Induced Cracking

In this section, the results of the hydrogen induced cracking studies will be compared to predictions of existing models of internal hydrogen embrittlement. In addition, through consideration of available fracture mechanics models of cracks in ductile materials, possible explanations for the observed results will be considered.

The generally accepted picture of internal hydrogen induced cracking is that hydrogen will accumulate in front of the notch root, presumably near the region of maximum hydrostatic stress. When a critical concentration is attained, a microcrack will form and crack growth will occur when this microcrack propagates back to the notch or

crack root. As discussed in the literature review chapter, this approach has been used by Gerberich[102] and van Leeuwen[106]. Using the simple model of van Leeuwen, and appropriate mechanical parameters for example, Fig. 6-2 shows predicted crack growth curves for the material of this study. Although this derives from a highly simplified calculation, and the crack tip radius will most certainly change appreciably during crack growth (except for K = constant tests), the important point is that this model already predicts the drop in crack velocity above threshold K levels. It is tempting to suggest that this apparent similarity with the present data is due to the sequence of cracking which van Leeuwen has proposed. However, several other possible explanations exist.

Gerberich's analysis required the use of an empirically determined crack tip radius in order to predict a decreasing crack velocity with increasing stress intensity, and even this produced a linear relationship between ρ and K whereas an analysis of Rice[93] predicts ρ to vary as K^2. Gerberich determined the crack tip radii at the specimen surfaces in his study so free surface (plane stress) effects may be the cause of this discrepancy.

It is believed that these models are not applicable to the present study for several reasons. McMahon et al.[158] have attempted to explain erratic v-K data in the following way: K-independent crack growth is unlikely since cracking occurs by the formation of small cracks in advance of the main crack and their subsequent joining. Since the cracks often form along side of, rather than directly ahead of the main crack, crack advance occurs in an uneven way along the main crack front. This irregular crack morphology in turn produces variations in the state of stress and the diffusion distance for hydrogen to the point of maximum triaxiality. From the fractographic analysis of the crack growth specimens, it is believed that events within the plastic enclave, but not restricted to the site of maximum triaxiality on the θ = 0 plane, are important to the crack growth process. The possible reasons for the distinction of the present results from the previous predictions are several fold. First of all, the yield strength of the steel used in this study was significantly less than that used by Gerberich, whose strength levels ranged from 1100 to 1500 MPa. This resulted in a more sizable plastic zone than was possible in
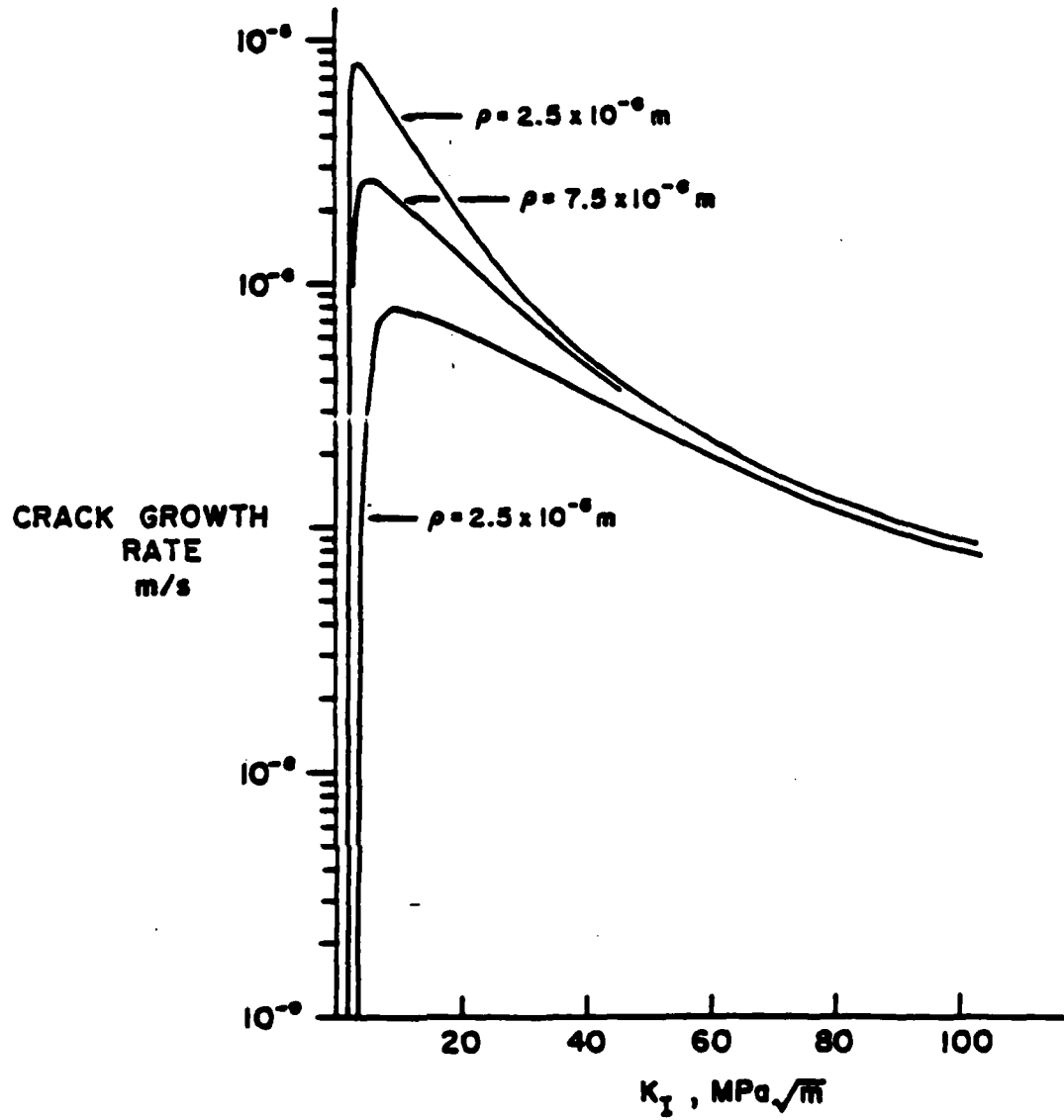
Figure 6-2: Predicted crack growth-stress intensity behavior using simplified van Leeuwen model[106]

Gerberich's study. For example, using Rice's[93] elastic-plastic crack tip model, the maximum radius of the plastic zone is:

$$\sim 0.17 \left[\frac{K}{\sigma_{ys}}\right]^2 \tag{6.7}$$

along a 70° angle from the crack growth direction. Assuming $K=70$ MPa$(m)^{1/2}$ and $\sigma_y = 700$ MPa, this predicts a $1700\mu m$ extent of the plastic zone, which for this material means a sampling of 10-20 prior γ grains. By comparison, a typical range of plasticity during irregular crack growth for Gerberich's[102] study would be from 100 to $150\mu m$, much closer to an expected prior γ grain size. This may be an important reason why these authors observed partial intergranular fracture in this regime while this mode was largely absent (except for the $600^\circ C$ aged sample) in the present study.

The state of stress may have had a strong influence on cracking in all of these tests from a macroscopic standpoint. In general, the state of stress ahead of the main crack will depend on intrinsic parameters such as yield strength and work hardening rate as well as extrinsic factors such as applied load (K_1) and specimen geometry, especially thickness. Plane strain conditions will prevail for situations where the size of the plastic zone (r_p) is small in comparison to the thickness $(B)^{[159]}$. As r_p/B approaches unity, plane stress will become more prevalent. Experimentation has shown cracking typical of plane strain if $r_p/B \ll 0.025^{[159]}$. Although this criterion appears simple enough, an accurate description of r_p (both spatially and numerically) is difficult to attain.

Considering first the simple Von Mises Criterion for yielding, the plastic zone depth along the cracking plane is given by:

$$r_p(\theta=0) = \frac{K^2}{2\pi \sigma_{ys}^2} [1-2\nu^2] = 0.028 \left[\frac{K}{\sigma_{ys}}\right]^2 \tag{6.8}$$

If Irwin's[160] plastic zone model incorporating plastic constraint is used, the form of r_p becomes.

$$r_p(\theta=0) \sim \frac{1}{6\pi} \frac{K_I^2}{\sigma_{ys}^2} \sim 0.053\left[\frac{K}{\sigma_{ys}}\right]^2 \qquad (6.9)$$

Assuming that $\sigma_{ys} = 770$ MPa for the material of this study, then the Von Mises model predicts the plane strain-plane stress transition to occur at 90 MPa$(m)^{1/2}$ while the Irwin analysis predicts this to take place at 65 MPa$(m)^{1/2}$. Although this difference represents a meaningful discrepancy, a re-examination of the cracking results shows that irregular cracking behavior was initiated in all tests at stress intensities of 60-70 MPa$(m)^{1/2}$. Since the yield strength levels were essentially constant for all conditions studied here, the possibility of a macroscopic stress state transition effect on crack growth must be considered. The implications of such a stress state transition are several fold. The reduced hydrostatic stress state accompanying plane stress would diminish the concentration and flux enhancements as predicted by Li, Oriani, and Darken[104]. Even in terms of a simplified critical stress/concentration assumption for the hydrogen induced cracking sequence, this in of itself would predict longer times between cracking events and an overall drop in macroscopic cracking velocity. Additionally, the larger plastic zone size (or longer extent along the crack front) may allow for more relaxation at the crack tip, resulting in larger values of $\bar{\rho}$ which, would diminish the driving force for hydrogen diffusion to the crack tip region. The higher shear stresses in and of themselves would favor ductile fracture mechanisms (as were observed) which should require higher K values to propagate. Finally, the larger plastic zone "wings" would produce large dislocation trapping "sinks", as mentioned previously, which would tend to redistribute hydrogen away from the crack tip.

The observation of the many "blunted" secondary cracks also implies that many advance crack nuclei form ahead of the main notch. It is suspected that these blunt cracks are nucleated at larger cementite clusters and inclusions. The exact cause of the blunted appearance may not be determinable but they certainly suggest relaxation of the local stresses, possibly aided by hydrogen. This in turn produces a situation where the high triaxiality at the crack front would be greatly relieved, lessening the likelihood that sub-notch nuclei cracks would form exclusively at the predicted point of maximum

triaxiality, $\sim 2\delta_i$ according to Rice[93], and as was predicted in the van Leeuwen[106] and Gerberich[102] models.

Alternatively, a more likely cracking sequence would occur as follows. As a starting point, the elastic-plastic crack tip normal stress and plastic zone shape model of Rice and Johnson[179] and Rice and Tracey[180] will be considered as representative of this material. The normal stress distribution from this model is shown in Figure 6-3 for an ideally plastic and n=0.1 work hardening material. Internal hydrogen will be drawn to the stressed region but owing to the large extent of plasticity in comparison to the existing ferrite lath structure, it is probable that the plastic zone will become a "sink" for hydrogen, owing at least in part to the increased dislocation density within this enclave.

The examination of sectioned DCB specimens suggests that the enriched hydrogen levels within the plastic enclave eventually nucleate cracks along lath boundaries and lath packet boundaries. As mentioned previously, this may involve hydrogen assisted plasticity since these boundaries often coincide with {110} and {112} type slip planes in ferrite but this cannot be proven. However, the rounded features of these surface cracks on fracture surfaces indicates that significant plasticity occurs near many of these cracks prior to main crack passage. This again raises the question of hydrogen assisted plasticity; however, other possibilities exist. The intense tensile stresses existing prior to crack passage may in themselves have induced relaxation but the fact that this fracture process is sub-critical (and hence occurs only due to the hydrogen presence) in nature seems to exclude a purely fracture mechanics explanation. Bernstein[47] has previously suggested that sub-surface cracks in iron may present excellent sites for H recombination and pressurization. Examination of the fracture surfaces linking these "yawned" cracks suggests that normal quasi-cleavage is not involved in crack growth across these areas. Hence, hydrogen altered plasticity cannot be ruled out.

Whatever the exact cause of this cracking, it is probable that the main crack continues to grow by repeated link-up of these sub-notch cracks. The increased density of
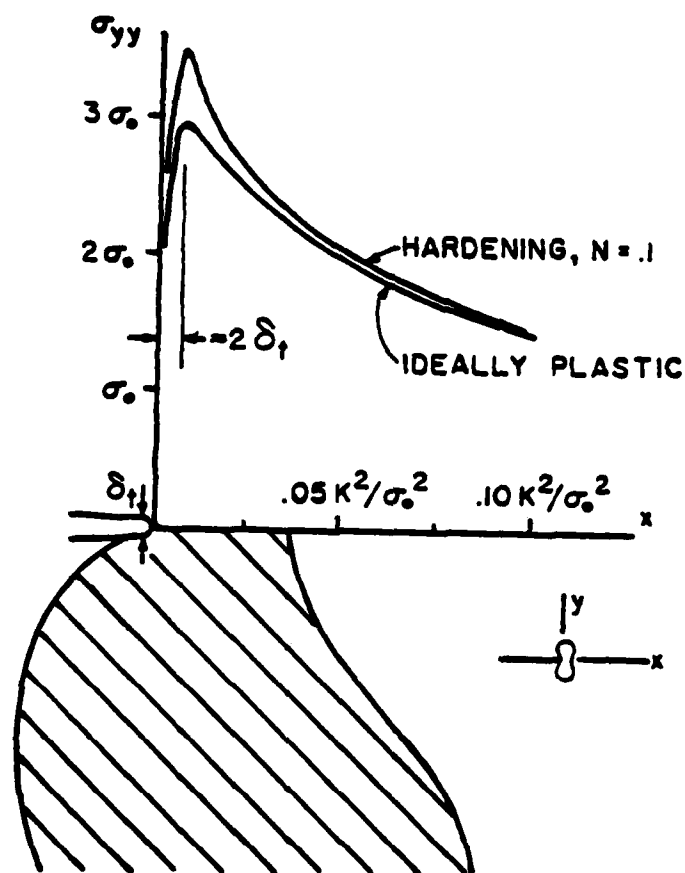
Figure 6-3: Predicted distribution of normal stresses and sub-notch depth of maximum stress for ideally plastic and n = 0.1 power law work hardening materials. from Rice[93]

secondary cracks in the microstructural sequence AQ → 500°C → 400°C can easily be explained by considering that the 400°C aged microstructure contains the coarsest interlath carbides which may act as crack nuclei. Finer, interlath cementite occurs in the 500°C microstructure and little detectable cementite occurs in the as-quenched material. Additionally, the possible detrimental role of large Ti inclusions must also be considered. As in the uniaxial tensile case, it is possible that these inclusions act as localized fracture initiation sites. For the present case of hydrogen induced cracking, these may also iniate blunted secondary cracks similarly to large cementite clusters. A rationalization of the results may also follow from the general outline of Pressouyre and Bernstein's[32] trap theory of hydrogen embrittlement. In this case, the more prevalent occurrences of blunted

secondary cracking in the 400° aged microstructure may be brought about by the lack of deep trapping and the correspondingly high apparent hydrogen diffusivity. This is especially evident from the diffusivities calculated from breakthrough times, as shown in Figure 5-29, where the 400°C aged microstructure diffusivity was an order of magnitude higher than either the as-quenched or 500°C aged microstructure. The combined higher diffusivity and lack of innocuous deep trapping may also help to explain why the 400°C aged microstructure possessed a lower threshold for cracking. When compared to a microstructure possessing deep traps such as the 600°C aging treatment, the 400°C aged condition would contain a higher diffusible hydrogen concentration which could more rapidly relocate under the action of stress. It may be recalled that the embrittled 600°C aged condition possessed a higher threshold, possibly due to a lower diffusible hydrogen content brought about by strong TiC trapping.

An additional note concerning the 400°C aging: It was noted that a somewhat constant crack velocity was found between stress intensities of 40 and 60 $MPa(m)^{1/2}$, where it is presumed that macroscopic stress state changes may have altered the cracking characteristics. It was found that the increments of crack advance in this regime was approximately 1000 μm and that constant growth rate was 3×10^{-7} m/sec. These parameters show that the time increment between cracking events was on the average 3000 sec. Using the thin film solution of Fick's law and 1000μm as a characteristic diffusion distance, a diffusivity of 3×10^{-6}cm^2/sec is found. This value corresponds quite closely with the breakthrough diffusivity of about 2×10^{-6}cm^2/sec found for the microstructure. If such a correspondence could be shown for the other microstructures, it may be possible to suggest a correlation between diffusivities calculated using breakthrough measurements and Stage II cracking. The most obvious solution to such a problem is to use test specimens designed to assure predominantly plane strain conditions at all stress intensity levels up to the intrinsic fracture toughness.

6.3.1. Summary

In summary, the hydrogen embrittlement susceptibility of this material appears to be explainable in terms of the competing effects of inocuous irreversible trapping (fine, dispersed TiC phase) and deleterious crack nuclei, (either inclusions or cementite clusters) which are themselves traps. It is also considered that stress state and time are important parameters to be characterized for the particular test configuration.

In the uniaxial tensile test, deformation is imposed and time (strain rate) is critically important. Contributions from possible dislocation transport are of obvious importance and localized stress state triaxiality about inclusions and defects would be expected to greatly influence hydrogen flux. From the experiments conducted herein, it is concluded that irreversible trapping is beneficial in such a trap configuration since it will permanently immobilize a greater quantity of hydrogen, even to mobile dislocations, as predicted by Pressouyre and Bernstein[32]. In the present case, the formation of irreversible traps (TiC) may even inadvertently have had a beneficial effects on diminishing the size and influence of possible crack nuclei (Fe_3C). The beneficial effects of such irreversible trapping were shown to be removed when the formation of such traps introduced a more detrimental temper embrittlement effect. This phenomenon is considered a separate event and if it can be inhibited independently, further improvements in hydrogen bearing properties would be expected.

In contrast, a fracture mechanics type test configuration, as used in this study, did not impose deformation on the material and time was presumably a less critical factor. For the conditions used in this study, long range diffusion of hydrogen through the matrix would be considered the critical process and the driving force would be the highly macroscopic stress state existing at the crack tip. In this test configuration, the different aspects of hydrogen permeability available from breakthrough and time-lag diffusivity can be expected to influence cracking behavior. First, the time-lag diffusivity may indicate the relative quantity of hydrogen which may redistribute under the influence of stress through a knowledge of irreversible trapping density. Second, the breakthrough diffusivity

will reflect to relative ease and expedience of the redistribution. The faster this is, the less likely that supersaturated concentrations of hydrogen will dissipate before the fracture mechanism intervenes.

Chapter 7
Conclusions

The primary goal of this thesis was to develop a greater understanding of the general observation that Ti and Ti precipitates are beneficial to the mechanical properties of iron and steel under conditions where absorbed hydrogen is present. It has been contended that this increased resistance to hydrogen embrittlement is brought about by a drop in apparent hydrogen diffusivity through low energy trapping at solute Ti atoms and higher energy trapping at titanium carbide/iron matrix interfaces. Through thermal treatment, various microstructures have been produced in the HSLA steel chosen for this study. The principal variables were the amount of free titanium and the related size, density, morphology and coherency of TiC precipitates. Hydrogen permeability in these microstructures has been studied using electrochemical permeation and the results compared to existing models which predict trapping effects on permeability based on trapping parameters. Hydrogen embrittlement susceptibility has been evaluated using two mechanically distinct testing modes. The first consisted of uniaxial tension (low triaxiality) testing of pre-charged cylindrical specimens over short time periods ($\sim$ 10 min). The second used a fracture mechanics specimen (high triaxiality) which was also pre-charged with hydrogen and tested over long time periods ($\sim$50-100 hrs.).

Microstructural characterization of quench and aged samples has established an aging sequence quite similar to that generally suggested by Honeycombe[22]. Quenching from elevated temperatures (1200°C) produces a highly substructured, nonequiaxed ferrite microstructure. Aging at temperatures $\leq$500°C results presumably in relief of quenched-in stresses and grain boundary precipitation of cementite. At temperatures above 500°C,

cementite formation is pre-empted by direct alloy carbide (TiC) formation and associated secondary hardening is observed. Aging at temperatures $\geq 700°$ results in appreciable recrystallization and softening. Aging at $500°C$ apparently produced both cementite and TiC phases. Softening associated with cementite formation was delayed (as compared with softening at $400°C$) and this was attributed to competition for carbon by TiC phase.

Analyses of trapping effects on hydrogen diffusivity and permeability revealed that the various microstructures may possess subtle but significantly different trapping properties. As expected, the as-quenched microstructure displayed hydrogen permeation transients typical of ferrite consisting of reversible, low interaction energy traps such as dislocations, grain boundaries, vacancies, etc., and the strength of these interactions was found to agree well with the values found by Pressouyre[28]. Microstructures containing cementite ($400°C$ and $500°C$ agings) also revealed essentially reversible trapping, but the flux curves displayed transient "plateaus". The presence of these plateaus has been predicted by Iino[36] for microstructures containing reversible traps with high capture-to-release rate ratios. It is postulated that the cementite interface in these microstructures may possess a greater interaction than anticipated[134]. In accord with the findings of Pressouyre and others[34], TiC precipitates have been found to be strong, irreversible traps through analysis of sequential hydrogen flux transients. Microstructural examination of these microstructures showed a size range of precipitates from 30 - 120Å, which falls below the predicted 200Å size range for fully incoherent interfacial structure[16]. Hence, it is suggested that coherency and/or chemical interactions or possibly interactions with dislocations associated with semi-coherent TiC particles and hydrogen cannot be ruled out as a cause of deep trapping. Coarsening of the TiC phase at temperatures above $600°C$ results in both a reduction in irreversible trapping and a reappearance of transient plateaus in hydrogen flux transients. It is suspected that the transition to full incoherency of a greater fraction of TiC particles is responsible, resulting in trapping properties similar to those of cementite at lower aging temperatures. It was also found that the analyses of breakthrough times from hydrogen permeation transients do not provide a sensitive measure of the trapping character (reversible or irreversible), but may rather represent a more

realistic measure of the effective ease of hydrogen redistribution during dynamic mechanical testing and hence relative embrittlement susceptibility. As in the studies of Pressouyre, time-lag diffusivities were found to indicate most directly the relative densities of reversible and irreversible trapping. Due to the fact that these diffusivity values are obtained from integrated quantities of hydrogen flux, they may not provide a useful measure of short time susceptibility to hydrogen embrittlement.

Short term tensile testing of pre-charged specimens with the various microstructures summarized above essentially established two separate regimes of response. Microstructures formed from aging at temperatures $\leq 500^\circ C$ failed by formation of torn topography surface[136] "facets" about nonmetallic inclusions. The presence of very fine TiC clusters was found to inhibit the formation of these facets, resulting in greater reductions of area upon failure. Microstructures formed on aging at temperatures above $500^\circ C$, where direct precipitation of TiC occurs, failed by brittle intergranular fracture along prior γ grain boundaries. The presence of P and S at these boundaries led to the conclusion that these impurities existed as benign clusters with Ti in solution before TiC phase formation. Upon precipitation, the elements are rejected to high angle boundaries.

Long term hydrogen induced cracking studies showed that the effects of hydrogen trapping and diffusivity may be quite complex. In microstructures possessing negligible deep trapping and exhibiting high breakthrough diffusivity (i.e. $400^\circ C$ aging), hydrogen embrittlement was most acutely manifested, mostly through a lower threshold. This may be rationalized as the consequence of maximum redistribution ease of a larger quantity of diffusible hydrogen. In the case of $600^\circ C$ microstructure, which cracked along low energy intergranular paths, a *higher* threshold was displayed nonetheless, due to the presence of deep trapping (lower quantity of diffusible hydrogen) and slower redistribution (lower breakthrough time). It was additionally concluded that conservative assurance of plane strain conditions in such tests was important for minimizing the complicating effects of extensive plastic zone formation.

Chapter 8
Recommendations

The findings of this study suggest future studies which may clear up some of the questions raised herein. These include:

1. The development of banded alloy carbide distributions during isothermal transformation was discussed but thermal treatments of this kind were not used. Besides their obvious applicability to controlled-rolling steels, the different alloy carbide distribution may alleviate the temper embrittlement mechanism by precluding nucleation at prior γ boundaries.

2. The effect of inclusions on ductile failure and the associated fracture mode transitions could be studied through preparation of a steel with a controlled density and size of inclusions, such as rare earth inclusions. Under such circumstances, the effect of the inclusion may be modelled through a better a priori knowledge of the altered stress distribution about the prarticle, influence diameter, etc.

3. Future heats prepared for studies of the type attempted here should be specified with certain guidelines in mind. Most importantly, Ti:C ratios should be held to 4:1 in order to ensure maximum hardenability. Also, the total Ti and C content should not exceed the solubility at the solutionization temperature which will be used. Sulfur levels should be kept below 0.01 w/o in order to avoid uncontrollable inclusions and loss of Ti. Alternatively, formation of a limited quantity of this phase may be beneficial for the following reason. Ti_2S and $Ti_4C_2S_2$ are hexagonal as is Ti_3P. If P substitutes in the former phases, this may provide a more efficient way of "gettering" phosphorus. Trapping at TiC interfaces appears to be of limited usefulness, especially in the presence of hydrogen. The final alternative may be to use a second reactive element addition, such as vanadium, to take the place of Ti in precluding segregation.

4. The anisotropy of both charged and uncharged tensile properties of the heat used for this study must be explained in order to know the generality of the conclusions. Nonuniform inclusion distributions and directional dependency of interlath or interpacket ferrite orientations should be checked through detailed microscopy. Detailed quantitative information concerning the effect of crystallographic texture on strength, ductility and toughness may also help answer this question.

5. Inhibiting extensive plasticity during fracture mechanics testing is also important for any future experiments of this type. This means that a valid

K_{Ic} should be established for all tempers investigated and design of HIC specimens based on these. Side grooving, although not essential, does appear to confine the crack to a planar path. This should be exercised carefully since the resulting affects on the stress intensity calibration for the specimen may not be easily determined. An addition factor of importance is the specimen arm height. This factor should be chosen to be $\geq$ 2B where B is the thickness. It is believed that this will stiffen the specimen arm and prevent bending of same. The thickness of the specimen should of course be chosen from linear elastic fracture mechanics considerations.

Appendix A
Characterization and Hydrogen Embrittlement
Susceptibility of heat 704K017

An additional heat similar to heat V113 was also characterized in a manner similar to that prescribed in Chapter 4. The goals of this additional work were to provide comparative microstructures against which the results found for heat V113 could be evaluated and also to provide a "cleaner" base material in an attempt to eliminate dominating inclusion effects on ductile fracture, as well as temper embrittlement type effects accompanying alloy carbide precipitation and associated metalloid segregation.

As seen from the chemical compositions of the two heats on Table 4-1, heat 704K017 contained a higher C level with a stoichiometric Ti content. The Mn level was lower by a factor of 1/2 and this heat was prepared essentially free of silicon. The heat treatment preparation of this heat similarly consisted of high temperature solutionization at 1200°C. Figures A-1 and A-2 exhibit the as-quenched microstructure revealing the fine lath structure and high dislocation density which was found in heat V113. Many sharp edged inclusions were also found in this heat (see Fig. A-1), leading to the conclusion that these were TiN particles[7]. These particles were found on a fine scale, as shown in Figure A-3 and faceting of these particles is also evident. The presence of this phase is undesirable since, once formed, these particles cause a continuous loss of Ti from the matrix. Due to the low solubility of TiN in austenite[9], this phase does not produce secondary hardening or inhibit grain growth of austenite since its distribution and precipitation cannot be controlled[5]. Figure A-3 was taken from a 600°C aged condition and once again, precipitation of finer TiC particles is observed. This aging reaction, in spite of the loss of Ti to inclusions, did give rise to notable secondary hardening.

The effect of lower Mn and Si levels as well as the consumption of Ti as inclusions on the strength level of this heat is evident from examination of Table A-1. A comparison with heat V113 shows that the strengths at equivalent heat treatments were generally 20% lower in heat 704K017. The lower Mn level may play a dual role in this loss of strength: not only will solid solution strengthening be diminished, but higher temperature transformation to ferrite may also occur during quenching, resulting in a lower hardenability. This is further supported by the more obvious rise in strength level accompanying secondary hardening at 600°C. This is consistent with a lower strength contribution from ferrite grain shape effects[3]. Additionally, it should be pointed out that this strengthening trend in longitudinal tensile properties is quite similar to that found for the transverse tensile properties of heat V113. This suggests an anisotropic grain shape or orientation role on the tensile properties of this material.

Tensile specimens identical to those used for longitudinal testing of heat V113 were polished, cathodically pre-charged with hydrogen, cadmium plated and pulled to failure as described in Chapter 4. A charge current density of $20\mu A/cm^2$, as was used with heat V113, produced very little embrittlement in any of the heat treatments, as shown in Figure A-4. The charging current density was increased to 0.1 and then 0.5 mA/cm². Some separation of microstructural response was observed at 0.1 mA/cm² and more so at 0.5 mA/cm². At 0.5 mA/cm² the lowest ductility was once again associated with the 600°C aging, but this must be viewed cautiously, since the strength level was almost 10% higher in this case. Each of the remaining three microstructures studied displayed virtually identical behavior and any differences in response to internal hydrogen cannot be determined from these tests.

The fractography of the failure surfaces reveals that inclusions once again played a significant role in failure as circular TTS facets associated with Ti and (N,S) rich inclusions were again found in the as-quenched, 400, and 500°C aged specimens for a 0.5 mA/cm² charging. As described before, this failure apparently initiated near the inclusion and radiated outward. Final failure of the intervening regions occurred by

Figure A-1: Optical Micrograph of microstructure resulting from 1200°C solutionization and water quenching of Heat 704K017. Nital etch. Nomarski interference
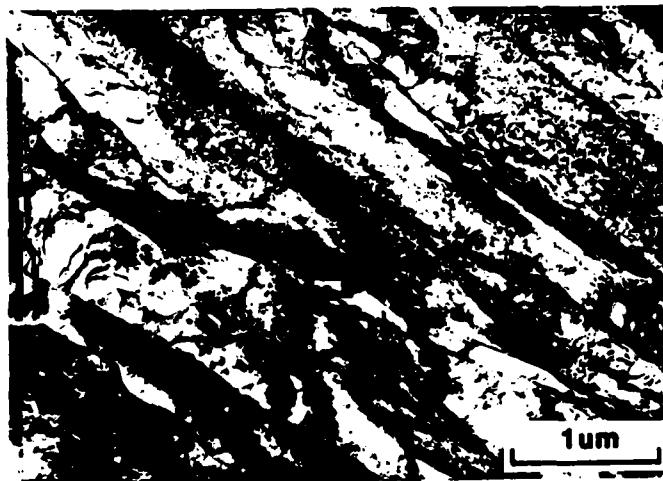
Figure A-2: Transmission electron micrograph BF image of microstructure of Heat 704K017 resulting from water-quenching from 1200°C
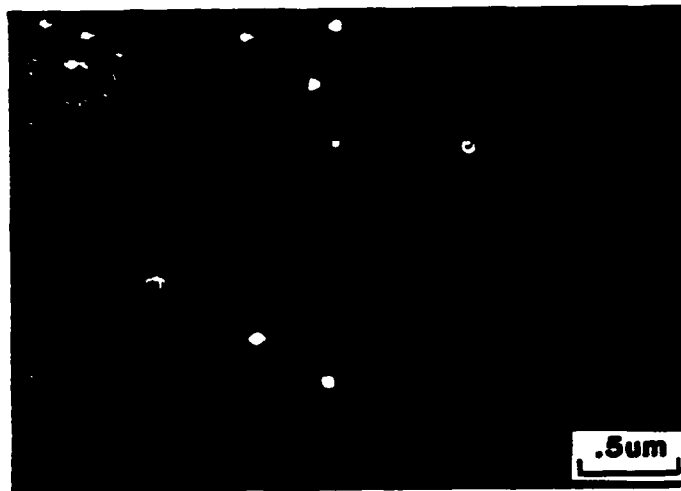
Figure A-3: Transmission electron micrograph DF image of faceted Ti(C,N) precipitates in 600°C/1hr aged microstructure

overload dimpled fracture. Although the 600°C aged specimen test did display plasticity before failure, fractographic analysis revealed that the fracture mode may be similar to that observed in the other heat, although less well developed. Figure A-5 shows the fracture from the 600°C aged specimen after the 0.5 mA/cm^2 charging, revealing some faceted regions which may be intergranular. Also, some quasi-cleavage regions are present within the dimpled fracture. In this case, it may be imagined that failure initiated at the intergranular regions. The sharp, local rise in stress and strain rate may have caused some of the quasi-cleavage fracture at this point. This fracture mode is reasonable owing to the higher flow stress in the matrix for this condition. Finally overall specimen fracture occurred by microvoid coalescence.

It appears, then, that some of the same trends observed in heat Vll3 were also exhibited by this heat, particularly a tendency for intergranular cracking accompanying secondary hardening and ductile failure initiated at inclusions. It must certainly be concluded, however, that this material is substantially less susceptible to internal hydrogen than heat Vll3. The key difference appears to be strength level and it is curious that the strength levels of these two materials lie just on either side of the so called 700 MPa

Table A-1: Summary of tensile properties and ductility levels of Heat 704K017

Thermal Treatment	$\bar{\sigma}_y$, MPa	$\bar{\sigma}_{UTS}$, MPa	%RA Uncharged	i=0.02 mA/cm^2	i=0.1 mA/cm^2	i=0.5 mA/cm^2
As-Quenched from 1200°C	633	767	79%	74%	66%	45%
400°C/1HR	662	735	80%	78%	63%	44%
500°C/1HR	653	728	78%	81%	77%	44%
600°C/1HR	719	778	72%	75%	64%	31%
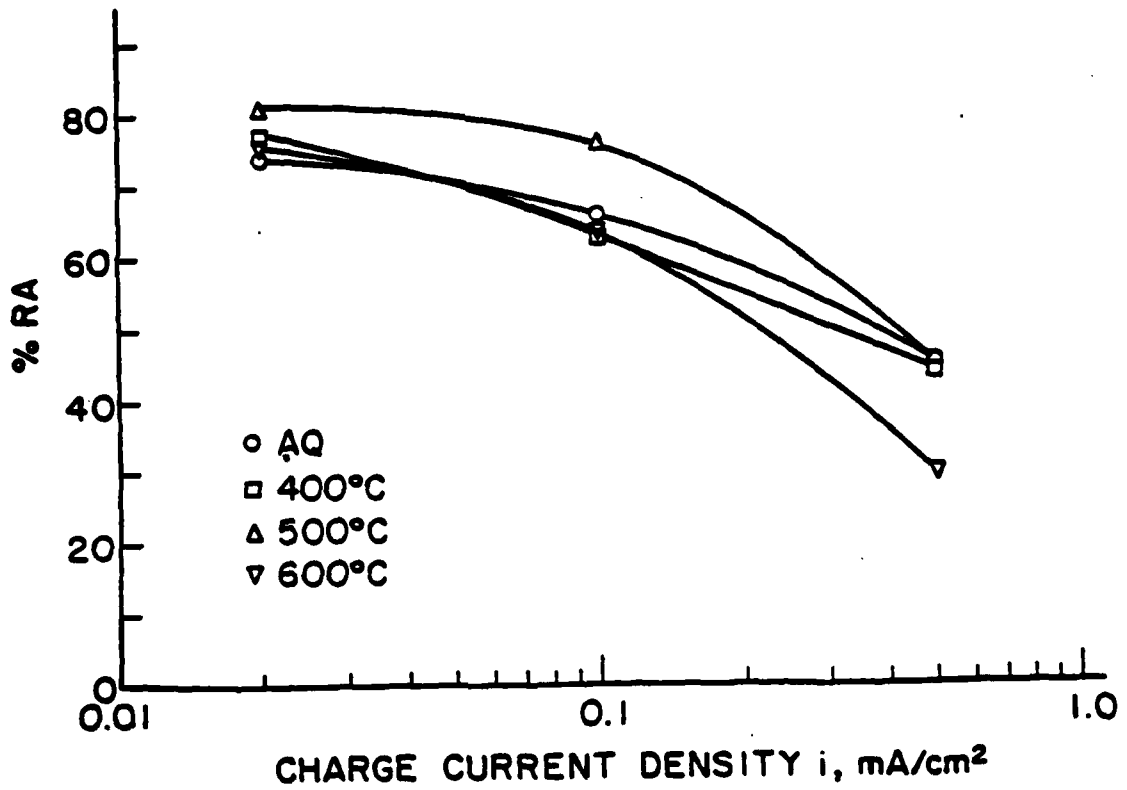
Figure A-4: Pre-charged hydrogen embrittlement susceptibility of Heat 704K017 with varing cathodic current density (hydrogen content). Values at 0.02 mA/cm^2 correspond to current densities used for Heat V113
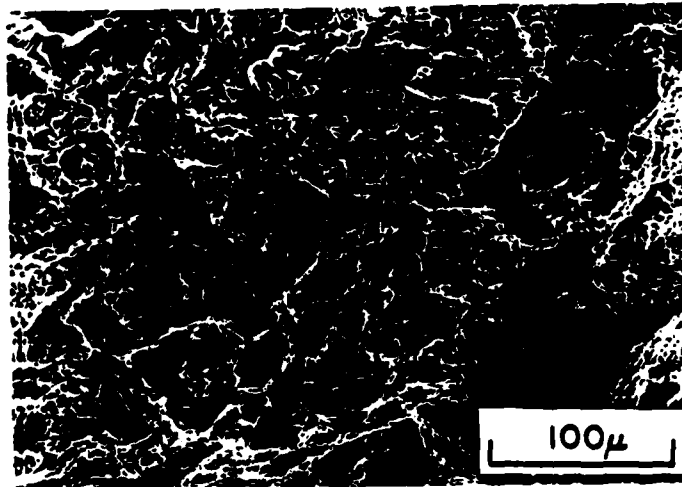
Figure A-5: SEM micrograph of tensile fracture surface resulting from 0.5 mA/cm^2 charging of 600°C/1hr aged microstructures

dividing line[173] between low and high strength steels. Thompson[173] has pointed out that

steels possessing strengths above this level exhibit increasing brittleness in the presence of hydrogen, although the significance of this strength level and the relative immunity of lower strength steels is not known. Another possibly key difference stems from the aging response of these two materials. It is clear that heat 704K017 derives less strength from grain refinement/dislocation density contributions (Fig. A-6), as judged from the more obvious secondary hardening (compared to heat V113). This may point to important dislocation sub-structure/hydrogen interactions insofar as they may affect bulk plasticity. More definitive knowledge concerning fundamental interactions between hydrogen and dislocations must be obtained before this possibility is exploited.
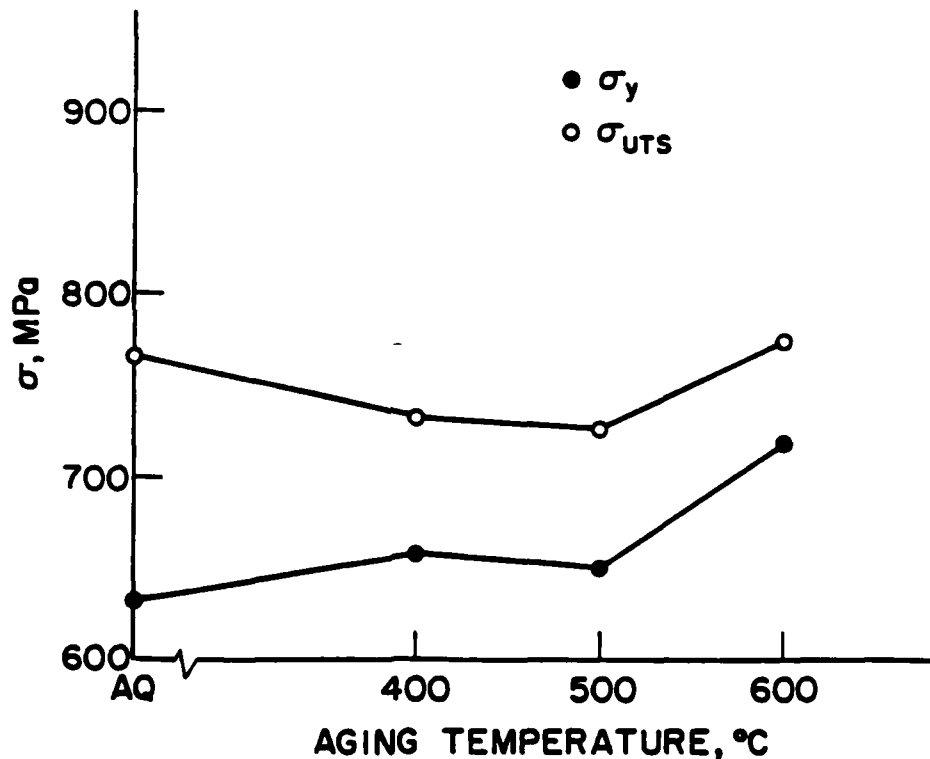
Figure A-6: Mechanical strength levels of Heat 704K017 as affected by aging

Hydrogen induced cracking studies using double cantilever beam type specimens were also attempted on this material, in a manner similar to that used on heat V113. Specimen preparation charging and plating was conducted exactly as described previously but once again, the higher charging current densities were used.

In this case, HIC as observed in heat V113 was not observed. Specimens were loaded in the charged condition to stress intensities ranging from 50 $MPa(m)^{1/2}$ to over 100 $MPa(m)^{1/2}$ and left for over 50 hours without any detectable crack growth occurring. As with the tensile test results, it appears that the lower strength level and associated plasticity considerations are responsible. Since the specimen dimensions were identical to those used for V113, one would even expect the plane strain/stress transition to occur at lower stress intensities. This observation is added evidence that more conservative specimen design may be necessary in order to obtain meaningful data from tests of this type.

These results, coupled with those found for heat V113, clearly indicate the importance of heat cleanliness and composition in determining embrittlement susceptibility, even when the failure mode is essentially ductile. The use of Ti may be beneficial to steels by the trapping of internal hydrogen, but the heat must contain low oxygen, nitrogen and sulfur levels, as these elements react with titanium preferentially to produce uncontrollable inclusion distributions. Moreover, thorough killing of melts through the use of aluminum or silicon may reduce oxygen levels, but the resulting oxide particles become convenient nucleation sites for lower temperature reactions between Ti and N and S. Hence, these materials must be produced in such a way that both inclusion and interstitial solute (e.g. O, N, S, and P) levels are kept low. Ironically, the present of a high density of sulfur rich inclusions may in fact be beneficial in offsetting the "temper embrittlement" reaction in heat 704K017 since the τ-Ti_2S phase (hexagonal) is isomorphous with TiP, and interchange of P for S is likely. Once "captured" in these low solubility particles, P would be permanently removed from solution, decreasing the likelihood of intergranular embrittlement, as was observed.

Chapter 9
References

1. L. F. Porter and P. E. Repas, *Journal of Metals*, 1982, pp. 14-21.

2. Morris Cohen and Walter S. Owen, "Thermomechanical Processing of Microalloyed Steels", in *Microalloying 75*, Conf. Proceedings, 1976, Union Carbide, pp. 2-8.

3. William C. Leslie, *The Physical Metallurgy of Steels*, 1981, McGraw-Hill, pp. 189-200.

4. L. J. Cuddy in *Thermomechanical Processing of Microalloyed Austenite*, A. J. DeArdo, G. A. Ratz and P. J. Wray, eds., AIME-TMS, 1983.

5. L. Meyer, F. Heisterkamp and W. Mueschenborn, *Columbium, Titanium and Vanadium in Normalized, Thermo-Mechanically Treated and Cold-Rolled Steels*, in Microalloying 75 Proceedings, 1976, pp. 130-144.

6. F. B. Pickering, ibid, 3-24.

7. L. Meyer, F. Heisterkamp and D. Lauterborn *Processing and Properties of Low Carbon Steel*, Metall. Soc. of AIME, 1973, pp. 279-320.

8. H. Chino and K. Wada, Yawata Tech. Rep. 251, (1965), pp. 5817-5842.

9. K. J. Irvine, F. B. Pickering and T. Gladman, *J. Iron Steel Inst.*, 1967, pp. 161-182.

10. D. A. Porter and K. E. Easterling, *Phase Transformations in Metals and Alloys*, Van Nostrand Reinhold, 1981, p. 275.

11. R. W. K. Honeycombe, *Metall. Trans.*, 7A, 1976, pp. 915-936.

12. S. Freeman in *Effect of Second Phase Particles on Mechanical Properties of Steel*, ISI Report No. 145, p. 152, 1971; London (Iron and Steel Inst.)

13. S. Freeman and R. W. K. Honeycombe, *Met. Sci*, 1977, pp. 59-64.

14. K. Campbell, Ph.D. Dissertation, University of Cambridge, 1971.

15. K. R. Kinsman and H. I. Aaronson, *Metall. Trans.*, 1973, 4, p. 959.

16. A. Youle, B. Ralph, S. Freeman and R. W. K. Honeycombe, *Metallography*, 7, (1974), pp. 333-344.

17. T. Gladman, D. Dulieu and Ian P. McIvor, in *Microalloying 75 Proceedings*, Union Carbide Corporation, 1976, pp. 25-48.

18. L. J. Cuddy, H. E. Knechtel and W. C. Leslie, *Metall. Trans.*, 5, 1974, pp. 1979-2003.

19. W. H. Herrnstein, J. A. Straatmann and R. A. Bosch, "Strengthening in Low-Carbon Titanium Steels", AIME Meeting, Pittsburgh, May 14, 1969 .

20. A. D. Batte and R. W. K. Honeycombe, *Met. Sci.*, 7, pp. 160-168, 1973.

21. J. H. Smith and J. J. Vett, *Met. Progress*, 96, No. 2, Aug. 1969, pp. 76-77.

22. R. W. K. Honeycombe, "Structure and Strength of Alloy Steels", Climax-Molybdenum Co., Special Report.

23. T. Gladman, B. Holmes and I. D. McIvor in *Effect of Second Phase Particles on Mechanical Properties of Steel*, ISI Report No. 145, 1971, pp. 68-78, London (Iron Steel Inst.).

24. R. W. K. Honeycombe, *Steels-Microstructure and Properties*, Edward Arnold and ASM, 1981, pg. 152.

25. L. S. Darken and R. P. Smith, *Corrosion*, 5, (1949), 1.

26. R. Gibala in *Stress Corrosion Cracking and Hydrogen Embrittlement of Iron Base Alloys*, NACE-5, 1977, p. 244, Houston, TX.

27. J. P. Hirth, *Metall Trans.*, 11A, 1980, pp. 861-890.

28. G. M. Pressouyre, Ph.D. Thesis, Carnegie-Mellon University, 1977.

29. G. M. Pressouyre and I. M. Bernstein, *Metall. Trans.*, 9A, 1978, pp. 1571-1580.

30. G. M. Pressouyre and I. M. Bernstein, *Corrosion Science*, 18, 1978, pp. 819-833.

31. G. M. Pressouyre and I. M. Bernstein, *Acta. Met.*, 27, 1979, pp. 89-100.

32. G. M. Pressouyre and I. M. Bernstein, *Metall. Trans.*, 12A, 1981, pp. 835-844.

33. M. A. V. Devanathan, Z. Stachurski and W. Beck, *J. Electrchem. Soc.*, 1963, pp. 886-890.

34. T. Asaoka, G. Lapasset, M. Aucoutourier and P. Lacombe, *Corrosion*, 34, No. 2, 1978, pp. 39-47.

35. H. Kimura, H. Matsui, A. Kimura, T. Kimura and O. Oguri in *Hydrogen Effects in Metals*, I. M. Bernstein and Anthony W. Thompson, eds., AIME-TMS, Warrendale, PA, 1981, pp. 191-208.

36. M. Iino and I. Yazima, in *Hydrogen in Steel*, Conf. Proc., 14-16 University of Bath, April, 1982.

37. J. F. Elliott, M. Gleiser and V. Ramakrishna, *Thermochemistry for Steelmaking*, Addison-Wesley, Reading, Mass. 1963.

38. J. Friedel, Ber. Bunsen-Gesellschaft, Vol. 76, No. 8, 1972, p. 828.

39. G. Lapasset, Thesis, Paris-Sud University, Orsay, 1975.

40. S. M. Meyers, D. M. Follstaedt and H. J. Rack, *J. Appl. Phys.*, 33, (1978), pp. 396-398.

41. J. Pillar, M. K. Miller and S. S. Brenner, *Trans 29th Field Emision Symp.*, Gotheburg, Sweden, 1982, pp. 473-480.

42. H. Erhart, H. J. Grabke and R. Moller, *Arch. Eisenhuttenwesen* 54 No. 7, 1981, pp. 285-289.

43. I. M. Bernstein and A. W. Thompson, *Int. Met. Rev.* (Rev 212) 21, (1976), pp. 269-287.

44. A. W. Thompson and I. M. Bernstein, "The Role of Metallurgical Variables in Hydrogen Assisted Environmental Fracture" in *Advances in Corrosion Science and Technology*, 7, M. G. Fontana and R. W. Staehle, Eds., (Plenum Publishing Corporation, 1980), pp. 53-175.

45. H. K. Birnbaum, "Hydrogen Related Failure Mechanisms in Metals". in *Environment Sensitive Fracture of Engineering Materials*, Z. A. Foroulis, ed. AIME-TMS, Warrendale, PA, 1979, pp. 326-360.

46. H. K. Birnbaum, "Hydrogen Effects on the Fracture of BCC Metals" in *Mechanical Properties of BCC Metals*, M. Meshii, ed., AIME-TMS, Warrendale, PA, 1982, pp. 153-172.

47. I. M. Bernstein, *Metall. Trans.*, 1A, 1970, p. 3143.

48. B. B. Rath and I. M. Bernstein, *Metall. Trans.*, 1A, 1972, p.2845, .

49. I. M. Bernstein, *Scripta Met.*, 8, 1974, pp. 343-350.

50. I. M. Bernstein and B. B. Rath, *Metall. Trans.*, 4A, 1973, pp. 1545-1551.

51. I. Takahashi, Y. Matsumoto and T. Tanaka, Proc. JIMIS-2, *Hydrogen in Metals*, Minakami, Japan, 1979, pp. 265-268.

52. A. B. Kuslitski, I. I. Kurilo, S. A. Zlotnikov and V. G. Starchak, *Fiz. Khim, Mekh. Mater.*, 6, No. 5, 1970, p. 98.

53. Y. N. Archakov, N. D. Grebeshkova, Y. I. Zuezdin and V. M. Kutyaev, *Zashch. Met.*, 9, No. 3, 1973, p. 288.

54. M. F. Stevens, I. M. Bernstein and W. A. McInteer in *Hydrogen Effects in Metals*, I. M. Bernstein and A. W. Thompson, eds. AIME-TMS, Warrendale, 1981, pp. 341-348.

55. L. Christodoulou, M. F. Stevens, J. J. Lewandowski, I. M. Bernstein and A. W. Thompson, "Studies of Microstructural Effects in Hydrogen Embrittlement of Steels", in *Environmental Degradation of Engineering Materials in Hydrogen*, M. R. Louthan, Jr., R. P. McNitt, and R. D. Sisson, Jr., eds., VPI, 1981, pp. 161-174.

56. B. I. Edelson and W. M. Baldwin, *Trans. ASM*, 55, 1962, pp. 230-50.

57. P. Bastien and P. Azou, *C. R. Acad. Sci.* Paris, 232, 1951, pp. 1845-1848.

58. John K. Tien, Anthony W. Thompson, I. M. Bernstein and Rebecca J. Richards, *Metall. Trans.*, 7A, 1976, pp. 821-829.

59. M. R. Louthan, G. R. Caskey, J. A. Donovan, and D. E. Rawl, *Mater. Sci. Eng.*, 10, 1972, pp. 357-68.

60. B. Craig and G. Krauss, in "Hydrogen Effects in Metals", I. M. Bernstein and Anthony W. Thompson, eds., AIME-TMS, Warrendale, PA, 1981, pp. 795-802.

61. Y. Takeda and C. J. McMahon, Jr., *Metall. Trans.*, 12A, 1981, pp. 1255-1266.

62. M. Iino, N. Nomura, H. Takezawa and H. Gundoh in *Hydrogen in Metals*, Proc. JIMIS-2, Minakami, Japan, 1971, pp. 617-620.

63. W. Steven and K. Balajiva, *J. Iron Steel Inst.*, 178, 1959, p. 141.

64. C. J. McMahon, Proc. 4th Bolton Landing Conf., J. L. Walter, J. H. Westbrook and D. A. Woodford, eds., Claitor's Pub. Division, 1975. pp. 525-552.

65. C. L. Briant and S. K. Banerji, *Int. Met. Rev.*, No. 4, (Rev. 232), 1978, pp. 164-199.

66. M. P. Seah, *Surface Science*, 53, 1975, pp. 168-212.

67. J. R. Low, Jr, *Prog. Mater. Sci*, 12, 1963, 1.

68. W. P. Rees and B. E. Hopkins, *J. Iron Steel Inst.*, 172P, 1952, p. 403.

69. C. J. McMahon, Jr., *Acta Met*, 14, 1966, p. 839-845.

70. J. R. Low, Jr. and R. G. Feustel, *Acta Met*, 1, 1953, p. 185.

71. A. Kumar and V. Raman, *Acta Met*, 29, 1981, pp. 1131-1139.

72. J. R. Rellick and C. J. McMahon, Jr. *Metall. Trans.*, 1, pp. 1970, 929-937.

73. P. Jolly and C. Goux, *Mem. Sci. Rev. Met.*, 66, 1969, p. 605.

74. H. J. Rack, *Metall. Trans.*, 3, 1972, pp. 1667-1670.

75. H. Ohtani, H. C. Feng, and C. J. McMahon, Jr., *Metall. Trans.*, 7A, 1976, p. 87.

76. H. Ohtani, H. C. Feng and C. J. McMahon, Jr., *Metall. Trans.*, 5A, 1974, pp. 516-520.

77. J. R. Rellick and C. J. McMahon, Jr., *Metall. Trans*, 5A, 1974, pp. 2439-2450.

78. H. Ohtani, H. C. Feng and C. J. McMahon, Jr., *Metall. Trans.*, 7A, 1976, pp. 1123-1131.

79. W. R. Graham and A. C. Yen, *Metall. Trans.*, 9A, 1978, pp. 1461-1465, .

80. H. Kaneko, T. Nishizawa, K. Tamaki and A. Tanifuji, *J. Jpn, Inst. Met.*, 29, 1965, p. 166.

81. M. Guttman, *Met. Sci*, 10, 1976, pp. 337-341.

82. H. W. Pickering, T. Sakurai, K. Al-Saleh, D. R. Hess, B. Bennett and H. Kim, "Proc. 30th Int. Field Emission Symp.", University Penn, Phila, PA, 1983.

83. J. I. Ustinovshchikov, *Acta Met*, 31, No. 3, 1983, pp. 355-364.

84. U. W. Cabral, A. Hache and A. Constant, *C. R. Acad. Sci.*, 260T, 1965, p. 6887.

85. K. Yoshino and C. J. McMahon, Jr., *Metall. Trans.*, 5, 1974, p. 363 .

86. C. L. Briant, C. J. McMahon, Jr. and H. C. Feng, *Metall. Trans.*, 9A, 1978, p. 625.

87. B. J. Berkowitz, J. J. Burton, C. R. Helms, and R. S. Plizzotti, *Scr. Met.*, 10, 1976, p. 871.

88. R. D. McCright and R. W. Stehle, *J. Electrochem. Soc.*, 121, 1974, p. 609.

89. R. M. Latanision and H. Opperhauser, Jr., *Metall. Trans*, 5A, 1974, p. 483.

90. B. F. Brown, *Stress Corrosion Cracking in High Strength Steels and in Titanium and Aluminum Alloys*, Naval Research Laboratory, 1972.

91. S. M. Wiederhorn in *Materials Science Research* (W. W. Kriegel and H. Palmour III, eds.) 3, 1966, pp. 503-528, Plenum Press, New York.

92. H. G. Nelson and D. P. Williams, In *Stress Corrosion Cracking and*

Hydrogen Embrittlement of Iron Base Alloys, R. W. Staehle, J. Hochmann, R. D. McCright, and J. E. Slater, eds., NACE-5, 1977, p. 390, Houston, TX.

93. J.R. Rice, ibid., p. 11.

94. D. P. Williams and H. G. Nelson, *Metall. Trans.*, 1, 1970, pp. 63-68 .

95. D. P. Williams and H. G. Nelson, *Metall. Trans.*, 3A, 1972, pp. 2107-2113.

96. J. D. Landes and R. P. Wei, *Int. Journal Fracture*, 9, No. 3, 1973, pp. 277-293.

97. S. J. Hudak, Jr. and R. P. Wei, *Metall. Trans.*, 7A, 1976, pp. 235-241.

98. R. P. Gangloff and R. P. Wei, ibid., 8A, 1977, p. 1043.

99. V. R. Sawicki, Ph.D. Dissertation, Materials Science Center, Cornell University, 1971.

100. W. A. van der Sluys,"Mechanisms of Environment Induced Subcritical Flaw Growth in AISI 4340 Steel", T & AM Report No. 292, Dept. Theo. and Appl. Mechanics, University of Illinois, 1966.

101. W. W. Gerberich and Y. T. Chen, *Metall. Trans*, 6A, 1975, pp. 271-278, .

102. W. W. Gerberich, Y. T. Chen, and C. St. John, ibid., *6A*, 1975, pp. 1485-1498 .

103. A. R. Troiano, *Trans ASM*, 52, 1960, p. 54.

104. J. C. M. Li, R. A. Oriani and L. S. Darken, *Z. Physik. Chem.* 49, 1966, p. 271.

105. R. A. Oriani, Berichte. Der Bunsen Gesellschaft Fur Physiakalische Chemie, Proc. Conf. on Hydrogen in Metals, Julien, 1972.

106. H. P. van Leeuwen, "Quantitative Models of Hydrogen-Induced Cracking in High Strength Steels" in *Reviews on Coatings and Corrosion*, J. Yahalom, ed. Vol IV, No. 1, Scientific Pub. Div., Freund Publishing House Ltd. POB 35010, Tel-Aviv, Israel, 1979.

107. F. M. Burdekin and D.E.W. Stone, *J. Strain Anal.*, 1, No. 2, 1966, pp. 145-153.

108. R. A. Oriani, *Acta Met*, 22, 1974, p. 1065.

109. H. P. van Leeuwen, *Corrosion*, 31, No. 2, 1975, pp. 42-50.

110. H. P. van Leeuwen, *Eng. Frac. Mech.*, 6, 1974, pp. 141-161.

111. C. S. Carter, ibid., 3, 1971, pp. 1-13.

112. C. G. Interrante and S. R. Low, in *Current Solutions to Hydrogen Problems in Steel*, C. G. Interrante and G. M. Pressouyre, eds., Proc. 1st Int. Conf. on Current Solutions to Hydrogen Problems in Steels, ASM, Metals Park, Ohio, 1982, pp. 557-562.

113. C. R. Roper "Preparation of Thin-Foil Steel Specimens for Electron Microscopy", in Metals Handbook, 8, 8th Edition, ASM, Metals Park, OH, 1973, p. 69.

114. Y. J. Park, Ph.D. Thesis, Carnegie-Mellon University, 1977.

115. S. S. Brenner and M. K. Miller, *J. Metals*, 35, No. 3, 1983, pp. 54-63 .

116. H. W. Pickering, Y. Kuk and T. Sakurai, *Appl. Phys. Let.*, 36 No. 11, 1980, pp. 902-904.

117. H. W. Pickering and T. Sakurai in *Environmental Degredation of Engineering Materials in Hydrogen* M. R. Louthan, Jr., R. P. McNitt and R. D. Sisson, Jr., eds., VPI, Blacksburg, VA, 1980, pp. 413-423.

118. J. Crank, *The Mathematics of Diffusion*, Oxford, Clarendon Press, (1956).

119. M. A. V. Devanathan and Z. O. J. Stachursky, *Proc. Roy. Soc.*, A270, 1962, p. 90.

120. K. Kiuchi and R. B. McClellan, *Acta Met*, 31, No. 7, 1983, pp. 961-984 .

121. M. Zamanzadeh, A. Allam, C. Kato, B. Ateya, A. H. W. Pickering, *J. Electrochem. Soc.*, 129, No. 2, 1982, pp. 284-289.

122. D. A. Berman, Naval Air Systems Command Progress Report NADC-82238-60, 19 November, 1982.

123. Plane-Strain Fracture Toughness of Metallic Materials, ANSI/ASTM E 399-78, ASTM, Phila, PA, 1978.

124. R. G. Hoagland, *Trans ASME, JBasic Eng*, 89, 1967, pp. 525-532.

125. C. N. Freed and J. M. Krafft, *J. Mater.*, 1, No. 4, 1956, pp. 740-790.

126. G. R. Irwin and J. A. Kies, *Welding Research Supplement*, 1954, pp. 1935-1985.

127. M. Iino, *Metall. Trans.*, 10A, 1979, pp. 1691-1744.

128. A. J. West and M. R. Louthan, Jr., *Metall. Trans.*, 10A, 1979, pp. 1675-1682.

129. W. C. Leslie, *Metall. Trans.*, 3A, 1972, pp. 5-26.

130. G. R. Speich and W. C. Leslie, *Metall. Trans.*, 3A, 1972, pp. 1043-1054.

131. G. R. Caskey, Jr. and W. L. Pillinger, *Metall. Trans.*, 6A, 1975, pp. 467-476.

132. A. J. Kumnick and H. H. Johnson, *Acta Met.* 28, 1980, pp. 33-40.

133. P. Lacombe, M. Aucouturier, J. P. Laurent and G. Lapasset, in *Stress Corrosion Cracking and Hydrogen Embrittlement of Iron Base Alloys,* R. W. Staehle, J. Hochmann, R. D. McCright, and J. E. Slater, eds., NACE-5, p. 423-430, Houston, TX, 1977.

134. Wayne M. Robertson and Anthony W. Thompson, *Metall. Trans.,* 11A, 1980, pp. 553-557.

135. G. W. Hong and J. Y. Lee, *J. Mater. Sci.,* 18, 1983, pp. 271-277.

136. Anthony W. Thompson and J. C. Chesnutt, *Metall. Trans.* 10A, 1979, pp. 1193-1196.

137. E. E. Fletcher, "A Review of the Status, Selection and Physical metallurgy of High-Strength, Low-Alloy Steels", MCIC-79-39, Metals and Ceramics Information Center, Battelle Columbus Laboratories, March 1979.

138. S. H. Moll and R. E. Ogilvie, *Trans. Met. Soc. AIME,* 215, 1956, pp. 613-618.

139. S. Freeman, Ph.D. Disertation, University of Cambridge, 1971.

140. K. Kuo, *J. Iron and Steel Inst.,* 184, 1956, pp. 258-268.

141. M.A.V. Devanathan and Z. Stachurski, *Proc. Roy. Soc.,* 1, No. 270, 1962, p90.

142. A. McNabb and P. K. Foster, *Trans TMS-AIME,* 227, 1963, p. 618.

143. M. Iino, *Acta Met,* 30, No. 2, 1980, pp. 367-376.

144. M. Iino, ibid., 30, pp. 377-384.

145. A. Zielinski, E. Lunarska and M. Smialowska, *Acta Met,* 25, 1977, p. 233.

146. F. Nakasato and I. M. Bernstein, *Metall. Trans.,* 9A, 1978, pp. 1317-1326.

147. C. J. McMahon, Jr. in *Hydrogen Effects in Metals,* I. M. Bernstein and Anthony W. Thompson, eds. TMS-AIME, Warrendale, PA 1981, pp. 219-234.

148. T. Goldenberg, T. D. Lee and J. P. Hirth, *Metall. Trans.,* 9A, 1978, pp. 1663-1671.

149. Y. H. Kim and J. W. Morris, Jr., *Metall. Trans.,* 14A, 1983, pp. 1883-1888.

150. J. J. Gilman, *Trans TMS-AIME,* 212, 1958, p. 783.

151. H. Kimura, H. Matsui, S. Moriya, *Scripta. Met.,* 11, 1977, p. 413.

152. T. Tabata, I. M. Robertson and H. K. Birnbaum, Paper delivered in Philadelphia, PA; October 4, 1983, at Fall Mtg TMS-AIME.

153. J. F. Lessar and W. W. Gerberich, *Metall. Trans*, 7A, 1976, pp. 953-960.

154. C. D. Beachem, *Trans. ASME- J. Basic Eng*. June 1965, pp. 299-306.

155. T. D. Lee, T. Goldenberg and J. P. Hirth, *Metall. Trans*, 10A, 1974, pp. 439-448.

156. H. H. Johnson, J. G. Morlet and A. R. Troiano, *Trans TMS-AIME*, 212, 1958, pp. 528-536.

157. R. A. Oriani and P. H. Josephic in *Environment Sensitive Fracture of Engineering Materials*, Z. A. Foroulis, ed., TMS-AIME, Warrendale, PA 1979, pp. 440-450.

158. C. J. McMahon, Jr., C. L. Briant and S. K. Banerji in *Fracture 1977*, Vol 1, ICF4, Waterloo, Canada, June 19-24, 1977, pp. 363-385.

159. D. Broek, *Elementary Engineering Fracture Mechanics*, Sijthoff and Nordhoff, The Netherlands, 1978.

160. G. R. Irwin, Proc. 7th Sagamore Conf., 1960, p. IV-63.

161. G. R. Irwin, *J. Applied. Mech.*, 24, 1957, p. 361.

162. I.S. Tuba, *J. Strain Anal.*, 1, 1966, pp. 115-122.

163. A. B. J. Clark and G. R. Irwin, *Exp. Mech*, 23, 1966, p. 321. .

164. "Handbook of Auger Electron Spectroscopy", 2nd ed., L.E. Davis, N. C. MacDonald, P. W. Palmberg, G. E. Riach and R. E. Weber, eds. *Phys. Electronics Ind.*, 1976.

165. Z.Qu and C. J. McMahon, Jr.,*Metall. Trans.* 14A, 1983, pp. 1101-1108.

166. B. J. Schultz and C. J. McMahon, Jr., in *Temper Embrittlement of Alloy Steels* ASTM STP 499, ASTM 1972, p. 104.

167. L. D. Jaffee and D. C. Buffum, *Trans. ASM*, 42, p. 604, 1950

168. M. Ransick and P. Shewmon in *Hydrogen Effects in Metals*, I. M. Bernstein and A. W. Thompson, eds., TMS-AIME, Warrendale, PA, 1981, pp. 895-902.

169. C. Zapffee and C. Sims, *Trans. Met. Soc. AIME*, 145, 1941, p. 225.

170. A. R. Troiano, BISRA, The Iron and Steel Inst., Harrogate Conf., 1961, p. 1.

171. C. D. Beachem, *Metall. Trans.*, 3, 1972, p. 437.

172. H. Kimura, H. Matsui, S. Takaki, A. Kimura and K. Oguri in *Mechanical Properties of BCC Metals*, M. Meshii, ed. TMS-AIME, Warrendale, PA, 1982, pp. 125-133.

173. Anthony W. Thompson, *Effect of Metallurgical Variables on Environmental Fracture of Engineering Materials*, in *Environment-Sensitive Fracture Engineering Materials*, Z. A. Foroulis, ed. AIME-TMS, Warrendale, PA 1979, pp. 379-410.

174. D. Kalish and H. J. Rack, *Metall. Trans*, 2A, 1971, p. 2665.

175. Y. Kikuta in *Hydrogen Effects in Metals*, I. M. Bernstein and Anthony W. Thompson, eds., AIME-TMS, Warrendale, PA, 1981, pp. 755-765.

176. J. W. Edington, *Practical Electron Microscopy in Materials Science*, Van Nostrand Reinhold Co., New York, 1976, pp. 244-251.

177. W. A. Spitzig, Fund. Res. Lab., U. S. Steel Corp., Unpublished Reseach.

178. A. M. Brass. Thesis, Paris-Sud University, Orsay, 1983.

179. J. R. Rice and M. A. Johnson, "The Role of Large Crack Tip Geometry Changes in Plane Strain Fracture", in *Inelastic Behavior of Solids*, M. F. Kanninen et.al., eds., McGraw-Hill, New York, 1970, p. 641.

180. J. R. Rice and D. M. Tracey, "Computational Fracture Mechanics", in *Numerical and Computer Methods in Structural Mechanics*, S. J. Fenves et.al., eds., Academic Press, New York, 1973, p. 585.

REPORT DOCUMENTATION PAGE		READ INSTRUCTIONS BEFORE COMPLETING FORM
1. REPORT NUMBER N00014-75-C-0265 NR 036-099-19 C-MU	2. GOVT ACCESSION NO. AD-A148 610	3. RECIPIENT'S CATALOG NUMBER
4. TITLE (and Subtitle) Effect of Microstructure and Trapping on the Hydrogen Embrittlement Susceptibility of a Ti-Bearing HSLA Steel		5. TYPE OF REPORT & PERIOD COVERED Technical Report
		6. PERFORMING ORG. REPORT NUMBER NR 036-099-19
7. AUTHOR(s) M. Stevens & I.M. Bernstein		8. CONTRACT OR GRANT NUMBER(s) N00014-75-C-0265
9. PERFORMING ORGANIZATION NAME AND ADDRESS Dept. of Metallurgical Engineering and Materials Science; Carnegie-Mellon University; Pittsburgh, PA 15213		10. PROGRAM ELEMENT, PROJECT, TASK AREA & WORK UNIT NUMBERS
11. CONTROLLING OFFICE NAME AND ADDRESS ONR Code 471 Arlington, VA 22217		12. REPORT DATE November 1984
		13. NUMBER OF PAGES 175
14. MONITORING AGENCY NAME & ADDRESS(If different from Controlling Office)		15. SECURITY CLASS. (of this report)
		15a. DECLASSIFICATION/DOWNGRADING SCHEDULE

16. DISTRIBUTION STATEMENT (of this Report)

Qualified requesters may obtain copies from DDC.

Reproduction in part or in whole is permitted for any purpose of the U.S. Government.

17. DISTRIBUTION STATEMENT (of the abstract entered in Block 20, if different from Report)

unlimited

18. SUPPLEMENTARY NOTES

19. KEY WORDS (Continue on reverse side if necessary and identify by block number)

20. ABSTRACT (Continue on reverse side if necessary and identify by block number)

The general hydrogen embrittlement susceptibility of a Ti-bearing HSLA steel has been characterized and correlated with detailed transmission electron and field ion microscopic studies of various microstructures. The hydrogen permeability and trapping in the same microstructures has also been studied through the use of electrochemical polarization and potentiostatic detection. The trapping character of the various microstructures has been determined by the use of cathodically precharged cylindrical tensile specimens and hydrogen

DD FORM 1473 EDITION OF 1 NOV 65 IS OBSOLETE

induced cracking of double cantilever beam type fracture mechanics specimens.

The hydrogen permeability studies showed that austenitized and quenched micro-structures were composed of essentially low interaction energy reversible trap sites for hydrogen including but not restructed to grain boundaries, solute elements and dislocations. Aging at temperatures between 400°C and 500°C still resulted in a reversible trap population, although the character of trapping was inferred to have shifted to higher capture-to-release rates from examination of the form of the transient hydrogen exit flux. The introduction of cementite in these microstructures was assumed to be responsible. At aging temperatures of 600°C and higher, irreversible trapping of hydrogen was found to occur concurrently with the direct precipitation of the alloy carbide, TiC. As this precipitate coarsened beyond the estimated incoherent interface size range, irreversible trapping capability was lost and reversible trapping with high capture-to-release rate behavior was again found.

Pre-charged uniaxial tensile testing established that the formation of even 10-15 Å diameter "clusters" of TiC could bring about a 50% improvement in ductility compared to microstructures lacking this phase. More complete precipitation of Ti and C as carbide phase at 600° aging resulted in complete intergranular failure and loss of measurable ductility. This was found to be due to concurrent segregation of metalloids to high angle (prior γ) boundaries with the loss of titanium to the carbide phase.

Hydrogen induced cracking studies indicated that both bulk hydrogen diffusivity (as measured by permeation breakthrough times) and diffusable hydrogen content (as determined from permeation time-lag values) are important. In micro-structures possessing a relatively high "breakthrough" diffusivity and little or no irreversible trapping (i.e. 400°C aging), low threshold stress intensities and high stage II crack velocities were observed. In a microstructure having a relatively low breakthrough diffusivity and a high density of fine, irreversible traps (i.e. 600°C aging) a higher threshold was found notwithstanding the lower inherent fracture toughness resulting from temper embrittlement.

END

FILMED

1-85

DTIC